HOKKAIDO UNIVERSITY

Title	Fault Slip Behaviors in Plate Subduction Zones inferred from the Nano-scale Pore Structure of Fault Rocks
Author(s)	中元, 啓輔
Degree Grantor	北海道大学
Degree Name	博士(理学)
Dissertation Number	甲第15601号
Issue Date	2023-09-25
DOI	https://doi.org/10.14943/doctoral.k15601
Doc URL	https://hdl.handle.net/2115/90767
Type	doctoral thesis
File Information	Keisuke_Nakamoto.pdf

Hokkaido University Collection of Scholarly and Academic Papers : HUSCAP

Doctoral dissertation

博士学位論文

Fault Slip Behaviors in Plate Subduction Zones inferred from the Nano-scale Pore Structure of Fault Rocks

断層岩のナノスケール間隙構造からみる プレート沈み込み帯の断層すべり挙動

Keisuke Nakamoto

中元 啓輔

Department of Natural History Sciences, Graduate School of Science, Hokkaido University

北海道大学大学院理学院 自然史科学専攻

September 2023

Abstract

The pore structure of rocks is one of the factors influencing fluid and gas transport processes. In rocks composed of fine-grained minerals, such as shale, nanoscale pore structure is considered to play a particularly important role. Since crustal fault rocks, the subject of this study, are also rich in fine-grained comminuted rock fragments and clay minerals formed by water-rock interactions, nanoscale pore structure assessment will be important for understanding fluid and gas transport processes in fault zones. Furthermore, understanding these processes is essential for elucidating the mechanical behavior of faults and material cycles within the crust. The aim of this paper is to investigate the formation and development processes and mechanical properties of faults and to clarify the changes in deformation processes within subduction zones, mainly based on nanoscale pore structure assessment in fault rocks affected by coseismic deformations in a variety of environments from deep to shallow plate subduction zones.

Chapter 1 describes the importance of pore structure assessment in understanding fault behavior and the usefulness of gas adsorption/desorption methods when applying to fault rocks.

Chapter 2 introduces the principles and applications of gas adsorption/desorption measurements.

In Chapter 3, changes in the internal structure associated with fault deformation were examined for the fault gouge of the Shirako Fault, which develops in the Boso Accretionary Complex, central Japan. Previous studies suggest that this fault records coseismic high-velocity slip in the shallow part of the subduction zone. Gas adsorption/desorption measurements and mercury injection methods showed that pore size decreases in the fault gouge, while pore volume below 10 nm and BET specific surface area increase. As the increase in BET specific surface area is generally considered to be due to comminution of particles, particle size analysis by X-ray computed tomography was performed. The results showed that the particle size of quartz and feldspar did not change distinctly between the host rock and the fault gouge. This suggests the fracturing of finer-grained clay minerals and the associated formation

of micropores. Therefore, I focused on the XRD spectrum of the smectite-illite mixed-layer of the Shirako fault, which has been obtained in previous studies, and performed an XRD pattern simulation using Newmod. The results show that the XRD spectrum of the fault gouge can be explained by a decrease in the number of stacks of mixed-layers. In this fault, it is likely that little or no fracturing of feldspar and quartz grains occurred as a result of fault slip, and that delamination and deformation of clay mineral occurred preferentially. This suggests that the energy dissipation associated with particle comminution during the earthquake was suppressed, which may have facilitated coseismic slip on this fault.

In Chapter 4, the relationship between microscopic particle-particle interactions and fault-slip processes was investigated using fault gouge samples recovered from the plate boundary fault in the Japan Trench that triggered the 2011 Mw 9.0 Tohoku-oki earthquake. To evaluate the interparticle interaction energies, the zeta potential was measured by electrophoresis, and the surface free energy of the particles was determined by contact angle measurements. Based on these measurements and the extended DLVO (Derjaguin and Landau, Verwey, and Overbeek) theory, the interaction energies between the clay particles were evaluated, and it was found that the forces acting between the particles were very small under high-salinity conditions equivalent to the fault zone, which may have weakened the viscous resistance of the fault zone and resulted in large fault displacements during the earthquake. The interaction energy curves obtained also show the presence of a potential well, which indicates the existence of energetically stable particle configurations. The average interparticle distances estimated by the gas adsorption/desorption method deviate somewhat from this stable structure, and this may correspond to shear-induced structural break-up and subsequent post-seismic structural relaxation (strength recovery process). Furthermore, such structural break-up and subsequent structural relaxation within the fault zone may lead to the development of thixotropic properties of the fault and associated spontaneous stick-slip movements.

In Chapter 5, an assessment of the swelling behavior of faults was carried out for a shallow smectite-rich fault zone in a subduction zone. Mixed samples of montmorillonite and quartz powders were prepared and swelling pressures were measured when contacting with 0.6 *M* NaCl solution and pure water. Experimental results showed that under identical porosity conditions, the swelling pressure increased

with increasing smectite content. It was also found that the swelling pressure decreased as the ionic strength of the solution increased. Based on these results, the in situ swelling pressure of the fault equivalent horizon (proto-décollement) at the input site in the northern Sumatra Trench was investigated. This strata corresponds to a pelagic clay layer and is characterized by a high smectite content (>60 wt.%). This smectite content was found to be sufficient to generate a swelling pressure comparable to the effective vertical stress acting on the strata, suggesting that this may have caused a localized reduction in strength in the pelagic clay layer and triggered the onset of shear deformation (i.e., formation of proto-décollement).

In Chapter 6, the relationship between the pore structure of fault rocks and brittle deformation, especially around the principal slip zone of the fault (PSZ), was examined for the Nobeoka Fault, which belongs to the Shimanto Belt in Kyushu, Japan. The Nobeoka Fault is a fossil thrust that is considered to be a onshore analogue of a deeper part of the mega-branching fault from the plate-boundary décollement in the modern Nankai Trough, and is thought to record deformation associated with past trench-type earthquakes. In this study, borehole core samples penetrating the Nobeoka Fault were used to evaluate the pore structure by gas adsorption/desorption analysis and to quantify the mineral composition by XRD analysis. These analyses showed that the proportion of micropore volume (micropore / micropore + mesopore) increased in the PSZ due to a decrease in mesopore volume, while no clear difference in BET specific surface area was observed between the PSZ and the host rocks. Based also on the results of previous studies, this may be the result of comminution of illite particles and selective filling of mesopores. Such pore closure may have caused a reduction in permeability and contributed to the dynamic weakening process (thermal pressurization) associated with high-velocity coseismic slip during the earthquake. In the last part of this chapter, I examined how the pore structure changes with fault deformation depending on the depth of the subduction zone, based on the results of pore structure analysis carried out using shallower fault rocks in addition to the findings from the Nobeoka Fault. Here, the BET specific surface area, which has a high correlation with micropore volume and mesopore volume, was used as an example to compare the host rocks of each sample, and a sharp decrease in specific surface area was observed after a depth of about 3 km. This condition is thought to correspond to the onset of various fluid-mediated diagenetic processes (smectite illitization reaction, mineral cementation and pressure-solution deformation) around this depth. On the other hand, the specific surface area in

cataclastic deformation zones such as PSZ and damage zones tends to increase with respect to the host rock at depths shallower than 3 km, while it remains almost unchanged or even decreases at greater depths. As mentioned earlier, this is likely to be due to progression of fluid-mediated diagenesis at such depth. The present study indicates that diagenetic reaction plays a significant role in the establishment of seismogenic zones in subduction zones. It is also suggested that the pore structure assessment by gas adsorption/desorption method is a very effective method for further clarification of the diagenesis and seismogenesis in plate subduction zones.

要旨

岩石の間隙構造は流体やガスの輸送過程に影響を与える要因の 1 つである．頁岩のような細粒の鉱物を多く含む岩石では，ナノスケールの細孔構造が特に重要な役割をもつと考えられている．本研究が対象とする地殻の断層岩も，岩石-水相互作用によって形成される微細な粘土鉱物や破砕された細粒岩片で構成されるため，断層帯における流体やガスの輸送過程を理解する上でナノスケールの間隙構造評価が重要と考えられる．さらに，これらのプロセスを理解することは，断層の力学的挙動や地殻内の物質循環を解明するために不可欠である．本論文では，プレート沈み込み帯深部から浅部までの様々な環境において地震性の高速すべり変形の影響を受けた断層岩を対象として，主にナノスケールの間隙構造に基づいて，断層の形成・発達過程や力学的性質を検討し，沈み込み帯内の変形過程の変化を明らかにすることを目的とする．

第 1 章では，断層挙動を理解する上での間隙構造評価の重要性と，その評価手法としてのガス吸脱着測定法の有用性を述べる．
第 2 章では，ガス吸脱着測定の原理と解析手法について紹介する．
第 3 章では，房総付加体に発達する白子断層の断層ガウジを対象として，断層変形に伴う内部構造の変化を検討した．先行研究によりこの断層は，沈み込み帯浅部での地震性高速すべりを記録していると考えられている．ガス吸脱着測定および水銀圧入法による間隙構造解析の結果，断層ガウジにおいては細孔径が低下する一方で，10 nm 以下の細孔容積や BET 比表面積は増加することが分かった．一般に BET 比表面積の増加は粒子破砕による影響が考えられるため，X 線 CT による粒子径分析を行ったところ，石英や長石の粒子径は母岩と断層ガウジの間でほとんど変化が見られなかった．このことから，より細粒な粘土鉱物の破砕とそれに伴う細孔の形成が考えられる．そこで，先行研究で得られている白子断層の smectite-illite 混合層の XRD スペクトルに注目して，Newmod を用いたパターンシミュレーションを行った．その結果，断層ガウジのスペクトルが，混合層鉱物の積層数の減少によって説明できることを明らかにした．本断層においては，断層すべりに伴う長石や石英粒子の破砕が殆ど起こらず，粘土鉱物の剥離・変形が優先的に生じたと考えられる．このことは，地震発生時の粒子破砕に伴うエネルギー散逸が抑制され，その結果高速断層すべりがより促進された可能性を示唆している．
第 4 章では，2011 年東北地方太平洋沖地震 ($M_w = 9.0$)を引き起こした日本海溝プレート境界断層の断層ガウジ試料を用いて，粒子間の微視的な相互作用と断層すべり過程との関連性について検討した．粒子間相互作用力を評価するため，電気泳動法によりゼータ電位を測定し，さらに接触角測定を行うことで粒子の表面自由エネルギーを求めた．これらの測定結果と拡張 DLVO 理論に基づいて粘土粒子間の相互作用力を評価したところ，断層帯の間隙水に相当する高塩濃度条件では，粒子間に作用する力が極めて小さいことが分かり，

このことが断層帯の粘性抵抗力を弱め，地震発生時の大きな断層変位をもたらした可能性がある．また，得られた相互作用エネルギー曲線にはポテンシャル井戸が存在することが分かり，これはエネルギー的に安定な粒子配置が存在することを示している．ガス吸脱着法により推定される平均的な粒子間距離は，この安定構造から逸脱したものであり，地震発生に伴う粒子構造体の安定状態の破壊と地震発生後の構造緩和（強度回復過程）を見ている可能性がある．さらにこのような地震発生に伴う粒子構造体の破壊とその後の構造緩和は，断層のチキソトロピー性とそれに伴う自発的なスティックスリップ運動を発現させる可能性がある．

第 5 章では，スメクタイトに富む沈み込み帯浅部の断層帯を想定して，断層の膨潤挙動に関する評価を行った．モンモリロナイトと石英の混合サンプルを作成し，0.6 M NaCl 水溶液と純水を使用した膨潤圧測定実験を行った.実験の結果，同一の間隙率条件においては，スメクタイトの含有率が高いほど膨潤圧が増加することがわかった．また，溶液のイオン強度が大きくなると膨潤圧が小さくなることがわかった．この結果に基づいて，スマトラ沖海溝のインプットサイトにおける断層相当層準（プロトデコルマ）の原位置膨潤圧を検討した．この層準は遠洋粘土層に相当し，高いスメクタイト含有率（60 wt.%以上）で特徴づけられる．このスメクタイト含有量は，断層相当層準に作用する有効垂直応力に匹敵する膨潤圧を発生させるのに十分であることがわかり，このことが遠洋粘土層における局所的な強度低下を引き起こし，せん断変形（プロトデコルマの発達）の引き金となった可能性を示唆している．

第 6 章では，九州の四万十帯に属する延岡衝上断層を対象として，断層の間隙構造と特に断層中軸部（主せん断帯）付近に見られる脆性変形との関連性について検討した．延岡衝上断層は，現世南海トラフに見られるデコルマから派生した巨大分岐断層深部の陸上アナログと考えられている化石断層であり，過去の海溝型地震に伴う変形を記録していると考えられている．ここでは，延岡断層を貫通するボーリングコア試料を用いて，ガス吸脱着解析による間隙構造評価と XRD 分析による鉱物組成の定量を行った．分析の結果，主せん断帯においては mesopore 容積の減少に起因する micropore の比率が増加する一方で，BET 比表面積には明瞭な変化は見られなかった．先行研究の成果を踏まえると，これはイライト粒子の破壊に伴う細粒化と mesopore への選択的充填が起こった結果と考えられる．こうした細孔の閉鎖は，透水性の低下を引き起こし，地震発生時の高速変形に伴う動的断層弱化過程（熱圧化）に寄与した可能性がある．本章の最後では，延岡衝上断層の知見に加え，より浅部の断層岩を用いて実施した間隙構造解析の結果に基づいて，沈み込み帯の深度に応じて，断層変形に伴う間隙構造がどのように変化するかを検討した．ここでは，micropore 容積や mesopore 容積との相関の高かった BET 比表面積を例にとり，各試料の母岩の比較を行ったところ，深さ 3 km程度を境に，比表面積の急激な減少が確認された．これは，この深度付近から流体を介した多様な続成作用（スメクタイトのイライト化反応や鉱物のセメンテーション，圧力溶解変形）が始まることに対応していると考えられる．

一方，断層中軸や破砕帯といった脆性変形帯における比表面積の変化に注目すると，深さ３km程度を境に，それ以浅では母岩に対して増加する傾向にある一方，深部ではほぼ変化が見られないかむしろ低下する傾向にあることがわかった．先述の通り，これは深部における流体を介した続成作用の進行が大きく作用していると考えられる．本研究により，沈み込み帯における地震発生帯の成立過程において，続成作用が大きく関与していることが示された．またプレート沈み込み帯における続成作用と地震発生過程のさらなる実態解明に向けて，ガス吸脱着法による間隙構造評価が極めて有効な方法であることが示唆された．

Acknowledgements

First, I would like to express my deepest gratitude to my supervisor Dr. Jun Kameda, for his many advices and enthusiastic guidance. I would also like to thank my co-supervisor Dr. Marie Python, for her many comments at the laboratory seminar.

I would also like to thank my examiners, Dr. Takaya Nagai and Dr. Takeshi Kuritani, for their useful suggestions.

I would like to thank Dr. Yohei Hamada for his help with the mercury injection method, XRD analysis, and core sampling at the Kochi Core Center. I would like to thank Dr. Masaoki Uno for allowing me to use his equipment for swelling pressure measurement.

I would like to thank Dr. Toru Takeshita, Dr. Ippei Kitano, Dr. Hirokazu Masumoto, and other laboratory members for their active discussions on my research.

Finally, I would like to thank my family for always supporting me.

Index

Chapter 1 Introduction

Pores in rocks consist of intergranular voids between the constituent minerals, fractures, or their complexes (McCreesh et al., 2010; Passey et al., 2010). The structure of these pores (size, shape, connectivity, surface complexity, etc.) is one of the factors that influence fluid and gas transport processes. Among the various scales of pores in rocks, nanoscale pore structure is thought to play a particularly important role, especially in rocks composed of fine-grained minerals such as shale (Slatt and O'Brien, 2011). Since crustal fault rocks, the subject of this study, are also rich in fine-grained comminuted rock fragments and clay minerals formed by the water-rock interactions, evaluating the nanoscale pore structure will be important for understanding fluid and gas transport processes in fault zones. Furthermore, understanding these processes is essential to elucidate the mechanical behavior of faults as well as the material cycle within the crust. For example, in the short term, the pressure of fluids in a fault zone directly affects its strength (Sibson, 1973), and in the long term, fault properties develop through rock-water interactions that cause material changes in the fault zone (Evans and Chester, 1995). In addition, it has been noted that specific gas production/circulation occur on the fault (Kameda et al., 2003, Kameda and Okamoto, 2021), and these effects may alter the chemical environment of the fault zones such as redox states.

In recent years, with the increasing demand for shale gas, pore structure analysis, especially in shale, has been actively pursued because it is essential for elucidating gas storage mechanisms and establishing effective recovery technologies. Observation of pores using electron microscopy is one of the basic methods for pore structure analysis (e.g., Desbois et al., 2009; Schieber et al., 2010). However, such observations are generally two-dimensional, making it difficult to fully assess the three-dimensional shape and connectivity of pores. It is also difficult to fully evaluate the effects of nanoscale pores. Transmission electron microscopy is considered effective for observing nanoscale rock textures with sufficient resolution, but this method has the problem of limited observation area. In this regard, the gas adsorption/desorption method is considered to be an effective alternative tool that can be utilized to quantitatively evaluate complex, fine pore structures (Kuila and Prasad, 2013; Li et al, 2019; Qin et al, 2021; Kong et al, 2021; The details of gas adsorption/desorption method are outlined in Chapter 2). In particular, since clayey rocks such as shale form complex nanopore structures composed of hard, rigid grains (quartz, felspar, pyrite) and soft, ductile clay mineral grains, gas adsorption/desorption method is becoming the

primary analytical techniques for pore structure evaluation (Desbois et al., 2009; Schieber, 2010; Loucks et al., 2009; 2012). This method is also expected to be useful for the assessment of pore structure in fault rocks, but has so far only been applied in a few cases (Sawai et al., 2012; Daigle, 2014; Dutilleul et al., 2020). Proper assessment of the pore structure of fault rocks will be also important for understanding the formation and development process of faults.

On the other hand, to understand the formation process and retention mechanism of pore structure in clayey rocks, microscopic water-mediated interactions between particles should also be considered. This is because the pores in subsurface rocks are generally filled with fluid, and these particle-particle interactions are thought to govern particle packing and aggregation patterns. For example, in smectite-rich rocks, the swelling effect due to interparticle interactions is thought to be responsible for the formation of nanopores (e.g., Kuila and Prasad, 2013). In this study, I will evaluate the structure of nanopores in fault rocks and also examine their formation processes from the perspective of these microscopic particle-particle interactions.

This study will focus on faults that may or have actually experienced seismic activity in the plate subduction zones. As seen in the 2011 Mw 9.0 Tohoku-oki Earthquake, earthquakes that occur in plate subduction zones can sometimes be geohazards that cause great damage, and understanding their fault-slip processes is an urgent issue. Since these faults develop in clay-rich marine sediments and sedimentary rocks, nanopore analysis will become even more important for understanding the fluid and gas circulation processes and mechanical properties of faults. The samples analysed include fault rocks that are thought to have undergone coseismic high-velocity slip in a variety of depth conditions within the plate subduction zone. The objective of this study is to investigate the formation and development processes and mechanical properties of these faults, mainly by evaluating their nanoscale pore structures, and to clarify how the deformation process varies from shallow to deep in the subduction zones.

Chapter 2 Principles and applications of gas adsorption/desorption method

2.1 Overview of gas adsorption/desorption methods and adsorption/desorption isotherms

The gas adsorption/desorption method is an analytical technique that uses the phenomenon of physical adsorption, in which free gas molecules are adsorbed on a solid surface by intermolecular forces at low temperatures (Fig. 2.1). Since the amount of adsorbed gas molecules varies with pressure, the relative pressure P/P_0 of the gas is varied in the range $0 < P/P_0 < 1$ (P is the absolute equilibrium pressure and P_0 is the condensation pressure of the gas at laboratory conditions), and the amount of adsorbed gas molecules is measured in that interval. The plot of relative pressure versus the number of gas molecules adsorbed is called an adsorption/desorption isotherm. The curves when pressure is increased/decreased are called the adsorption/desorption branches, respectively, and the difference between the adsorption and desorption branches is called the hysteresis. The International Union of Pure and Applied Chemistry (IUPAC) classifies the shape of adsorption/desorption isotherms and hysteresis. This classification reflects the size and shape of the pores. Type I isotherm is considered to correspond to micropores, types IV and V to mesopores, types II and III to poreless or macropores, and type VI to poreless (Figure 2.2a), with micropores less than 2 nm in pore size, mesopores 2-50 nm, and macropores >50 nm, respectively. The classification regarding hysteresis is considered as follows: type H1 is an aggregate of spherical particles, type H2 is an ink bottle-type pore with a small pore diameter and a wide pore depth, and types H3 and H4 are slit-type pores created by plate-like particles (Fig. 2.2b). In addition to these qualitative classifications, isotherms can be used to estimate parameters related to pore structures, as shown below.

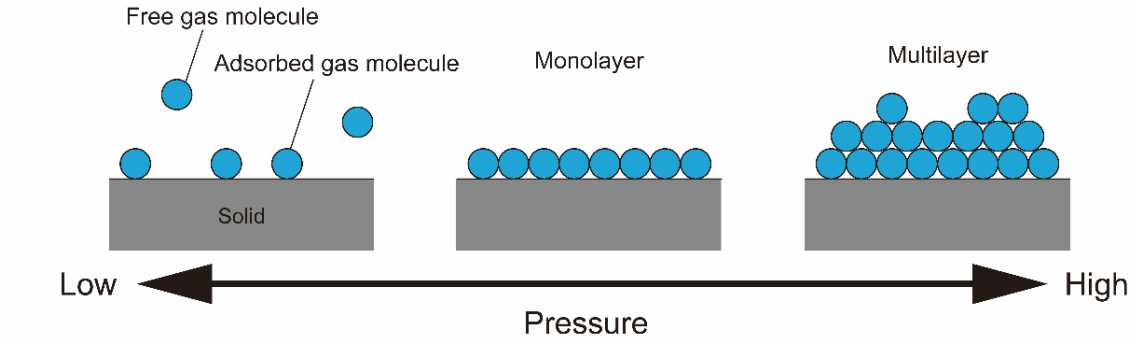

Figure 2.1. Adsorption of gas molecules on a solid surface by physical adsorption. The amount of gas molecules adsorbed increases as the pressure increases.

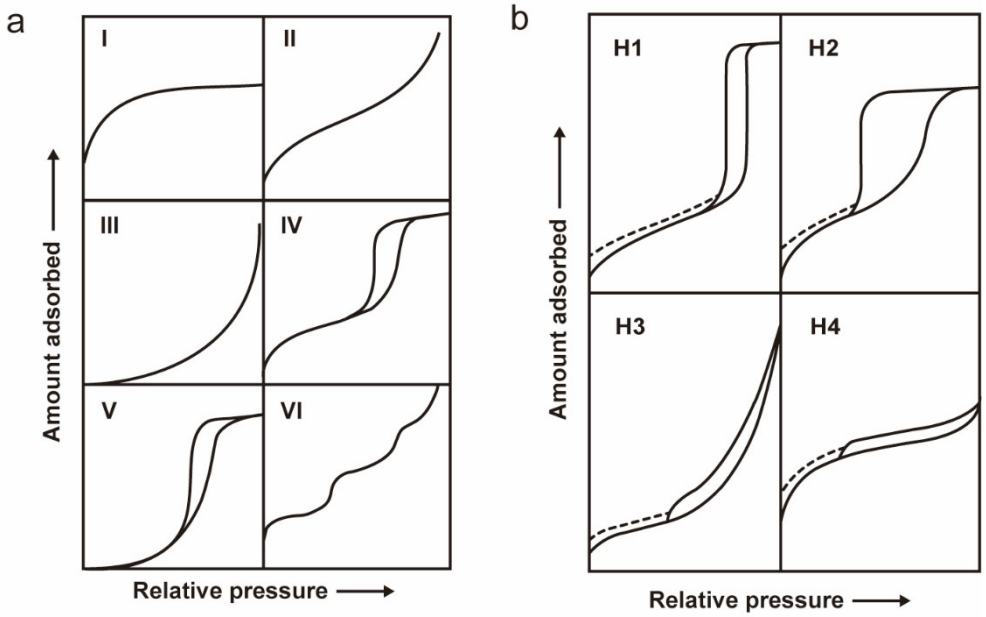

Figure 2. 2. Classification of isotherms and hysteresis loops (Sing, 1985). (a) Types of isotherms. (b) Types of hysteresis loops.

2.2 Brunauer-Emmett-Teller (BET) specific surface area

The specific surface area S (m^2/g) of a substance can be calculated by determining the amount of adsorption required to form a monolayer, or monolayer adsorption volume V_m (cm^3/g) (Fig. 2.3). The estimation based on the BET theory (Brunauer et al., 1938) is often used to calculate this monolayer adsorption volume from the adsorption/desorption isotherm, and Brunauer et al. (1938) proposed the following equation under the assumptions that the heat of adsorption and condensation after the second adsorption layer are equal, the evaporation/condensation constant ratio after the second adsorption layer is equal, and the number of adsorption layers is infinite when the relative pressure is 1:

$$\frac{x}{V_a(1-x)} = \frac{1}{V_m C} + \frac{(C-1)x}{V_m C} \quad (1),$$

$$C = \exp\left(\frac{E_1 - E_L}{RT}\right) \quad (2),$$

where x is the relative pressure, V_a is the amount adsorbed at relative pressure x, C is an adsorption parameter, E_1 is the heat of adsorption of the first layer of adsorption, E_L is the heat of condensation of adsorbed gas molecules (= heat of adsorption after the second layer), R is a gas constant, and T is the absolute temperature. Substituting x and V_a from the measured adsorption/desorption isotherm into equation (1) and plotting x and $x/V_a(1-x)$ on the horizontal and vertical axes, respectively, a straight line with slope $(C-1)/V_mC$ and intercept $1/V_mC$ is obtained to determine V_m and C. This can be applied in the range of relative pressure from 0.05 to 0.35. The cross-sectional area of adsorbed molecule is 0.162 nm for N_2, so the relationship between the specific surface area and the amount of monolayer adsorption is expressed as follows;

$$S = \frac{V_m}{0.162} \quad (3).$$

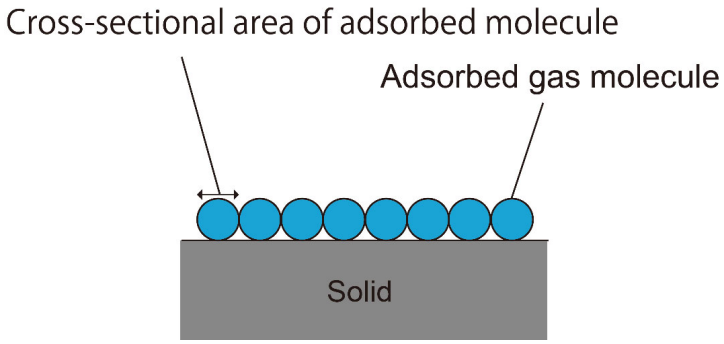

Figure 2.3. A solid surface on which adsorbed gas molecules form a monolayer. The BET specific surface area can be obtained from the cross-sectional area of the adsorbed molecule and the amount adsorbed.

2.3. Pore size distribution analysis by the Barret-Joyner-Halenda (BJH) method

The BJH method is a general method for estimating the pore size distribution in gas adsorption/desorption methods, in which the pore size distribution is calculated based on the following Kelvin equation assuming cylindrical pores (Barrett et al., 1951);

$$r = r_k + t = \frac{2\gamma V_L}{RT \ln \frac{P}{P_0}} \quad (4)\ ,$$

γ is the interfacial tension between the liquid and gas phases, V_L is the molar volume of the liquid phase, r is the actual pore radius, r_k is the Kelvin radius at which condensation occurs at a given relative pressure, and t is the thickness of the adsorption layer (Fig. 2.4). The value of t obtained experimentally or computationally is called the reference t-curve, which was calculated in this study using silica data.

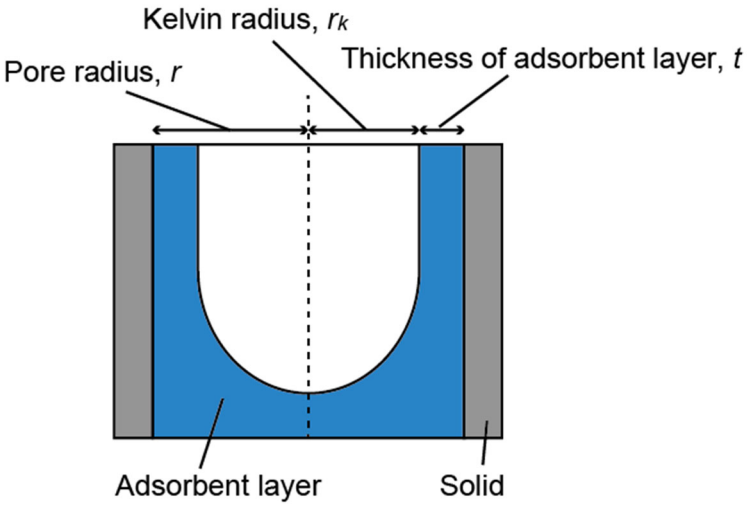

Figure 2.4. The adsorption layer assumed in the BJH method. This method assumes that the pore is cylindrical and analyzes the pore distribution based on the thickness and Kelvin radius of the adsorption layer.

2.4 Fractal dimension

Fractal dimension is a parameter that expresses the surface roughness and complexity of a material and has been proposed using the Frankel-Halsey-Hill model, which is described as follows (Avnir and Jaroniec, 1989);

$$\frac{V}{V_m} = K\left(RT\ln\left(\frac{P_0}{P}\right)\right)^{-(3-D)} \quad (5)\ ,$$

where V is the adsorption volume at a given pressure P, V_m is the unimolecular adsorption volume, K is the characteristic coefficient, and D is the fractal dimension. Equation (5) can be transformed to:

$$\ln V = \mathrm{Const} + S\ln\left(\ln\left(\frac{P_0}{P}\right)\right) \quad (6).$$

where S is the slope of the approximate line obtained by plotting the measured values on a coordinate with $\ln V$ and $\ln\left(\ln\left(\frac{P_0}{P}\right)\right)$ on the axes. The fractal dimension D is then expressed using S as follows:

$$D = S + 3 \quad (7).$$

The fractal dimension takes values between 2 and 3, with the closer to 2 indicating a smoother plane.

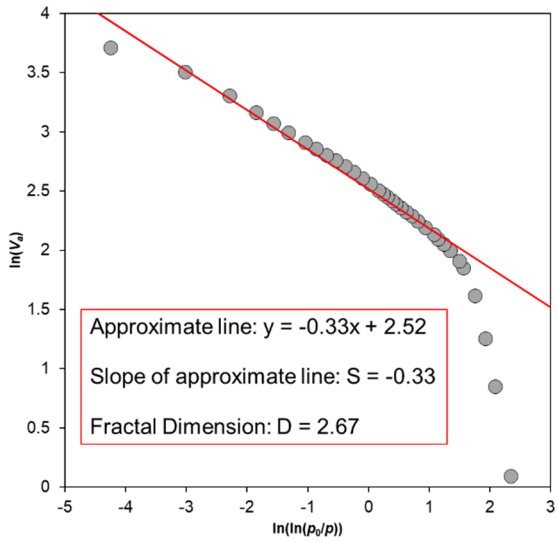

Figure 2.5. An example of the derivation of fractal dimension in the FHH model. The red line is the approximate straight line for the data, and the fractal dimension is calculated from its slope.

2.5 Experimental Conditions in this Study

In this study, sample preparation was performed according to the procedure described in Kuila and Prasad (2013). First, the sample was mildly ground in a mortar, and particles <425 μm were collected with a sieve. The increase in the specific surface area of the rock sample assumed by this treatment is negligible, as confirmed by Kuila and Prasad (2013). Before gas adsorption/desorption measurement, the ground samples were degassed at 200°C for 12 hours to remove water and gas molecules adsorbed on the surface. The measurements were performed under liquid nitrogen temperature (77 K) conditions by a gas adsorption analyzer (BELSORP MINI X, MicrotracBEL Corp.) using nitrogen as the adsorption gas.

Chapter 3 Deformation process of an imbricate frontal thrust at shallow depths in an accretionary prisms deduced from nanopore analyses

3.1. Introduction

Fault gouges are thought to be formed by fracturing of minerals and fluid-rock interactions associated with fault movement at shallow crustal depths (Sibson, 1977; Marone and Scholz, 1989; Vroljik and van der Pluijm, 1999). Since clay minerals formed by these processes control the frictional property and permeability of faults (e.g., Wibberley, 1999; Warr and Cox, 2001; Schleicher et al., 2009), clarifying the clay species and their fabric in fault gouge is important for understanding faulting mechanisms. In this study, I focus on a fault gouge of an ancient imbricate thrust fault in an on-land accretionary complex (the Shirako Fault in the Miura-Boso accretionary complex), and aim to clarify its developmental process especially by analyzing nano-scale pore structure using gas adsorption/desorption method. Here, I will generally refer to pores of 100 nm or less obtained by gas adsorption/desorption experiments as "nanopores", that is, including micropores (>2 nm pore size) and mesopores (2-50 nm pore size) according to the classification of the International Union of Pure and Applied Chemistry (IUPAC).

The Shirako Fault is thought to be a fossilized imbricate thrust that diverged from an ancient plate subduction boundary fault analogous to those observed at the Nankai margin (Kameda et al., 2013). Vitrinite reflectance measurements of the fault samples by Hamada (2011) revealed local reflectance anomalies around the gouge layer. Furthermore, clay mineral analysis by X-ray diffraction showed local illitization of the smectite-illite mixed layer (I-S) and partial decomposition of kaolinite (Kameda et al., 2013; Masumoto et al., 2018). Since these reactions are considered thermal activation processes, these observations suggest that some local exothermic events have occurred on the fault, presumably resulting from frictional heating associated with high-velocity coseismic slip of the fault. Therefore, further clarification of the developmental process of this fault is expected to be key to understanding the mechanism of earthquake generation and propagation of coseismic slip, especially in the shallow subduction zone where tsunamis can be triggered.

In recent years, the application of gas adsorption methods has greatly advanced our understanding of nanoscale pore structure in shale and sedimentary rocks (Kuila and Prasad, 2013; Dutilleul et al., 2020). It has been suggested that such nanopores develop to reflect the mineral species and fabric of fine particles such as clay minerals, and thus are expected to yield important information about the internal microstructure of fault gouge. However, there have been few examples of its application to natural fault rocks except for Sawai et al. (2012), who studied fault zones of granite origin. The analysis of Sawai et al (2012) focused on the change in solid surface area obtained by the gas adsorption method, and it was shown that the surface area of the fault gouge clearly increased compared to the parent granitic rock. Moreover, the author performed friction experiments using the gouge material and discussed the relationship between specific surface area and slip velocity, but little mention is made of changes in pore structures.

In this study, the analysis focused on the nanopore of the clay-rich Shirako Fault gouge derived from sedimentary rock and showed the distinct formation/increase of nanopores in the fault gouge. This may be related to modification, especially in clay minerals, associated with faulting. Based on these results, I discuss the development and deformation process of the Shirako Fault.

3.2. Geological Setting of the Shirako Fault

The Shirako Fault is thought to be formed as a member of imbricate thrust system of the Miura-Boso accretionary prism, on the Boso peninsula of central Japan (Kameda et al., 2013; Figures 3.1a and 3.1b). The host sedimentary sequence of the thrust system (Nishizaki formation) was deposited on the Izu-arc along the Sagami trough (Hanamura and Ogawa, 1993; Lee and Ogawa, 1998; Soh et al., 1989; Soh et al., 1991; Yamamoto and Kawakami, 2005) during 9.9–6.8 Ma (based on radiolarian biostratigraphy; Kawakami, 2001; Yamamoto and Kawakami, 2005). Porosity and vitrinite reflectance of the sediments indicate that this accretionary body has experienced a maximum burial depth of about 1000 m. In addition, detailed structural analyses showed that a suite of primary accretionary processes of incoming sediments from the initiation of décollement development, off-scraping, to imbrication of the off-scraped sediments is well preserved (Yamamoto et al., 2005; Yamamoto, 2006).

The Shirako fault strikes NE to SW, dips ~70° to northward, and is characterized by a black gouge from a few millimeters to centimeters thick (Figs. 3.1b–1d). Under the optical microscope, a preferred clay mineral alignment is observed in the gouge layer (Kameda et al., 2013), which is very similar to the comparative fault in the Miura

peninsula (the Sengen fault; Yamamoto et al., 2005). Mineral analysis shows no major differences in bulk mineral composition between the gouge and host rocks, but as mentioned earlier, local illitization reactions and kaolinite decomposition are specifically observed within the gouge layer (Kameda et al., 2013; Masumoto et al., 2018).

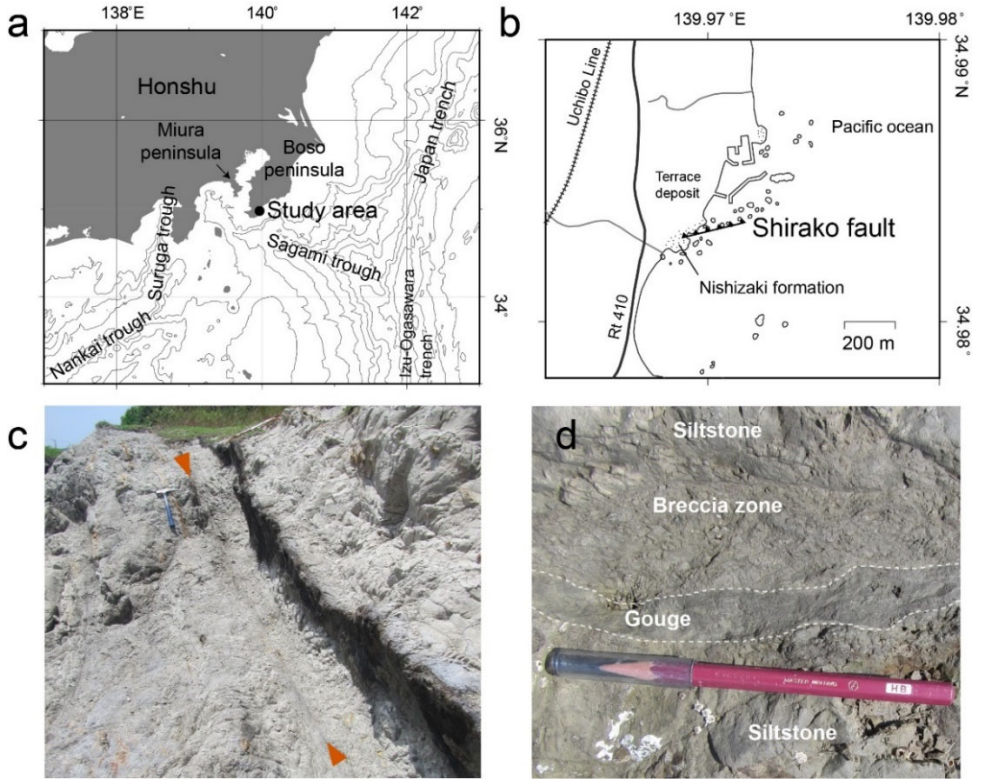

Figure 3.1. (a) (b) Location of the Shirako Fault. (c) Outcrop of the Shirako Fault. Red arrows show a trace of the slip zone of the fault. (d) Occurrence of the Shirako Fault.

3.3. Experiments

3.3.1. Gas adsorption/desorption measurements

I examined two gouge samples and 15 host rock samples collected from the Shirako Fault. Gas adsorption/desorption measurements were performed on the bulk samples which were gently ground and passed through a <425 μm sieve. Before the measurements, the samples were degassed at 200°C for 12 hours to remove water and gas molecules adsorbed on the surface. The measurements were performed by using a gas adsorption analyzer (BELSORP MINI X, MicrotracBEL Corp.) under liquid nitrogen temperature (77K) conditions. The obtained adsorption-desorption isotherms

were provided for pore size distribution (PSD) analysis based on the Barrett–Joyner–Halenda (BJH) method (Barrett et al. 1951). The specific surface area of the samples was also determined from the adsorption isotherms using BET (Brunauer, Emmett, and Teller) theory. Some samples were examined for the effect of salt removal, as described below, but no significant differences in the results were found between samples with and without salt removal treatment.

3.3.2. Macropore measurement by mercury intrusion method

Two samples (one from the gouge and another from the host rock) were subjected to macropore analysis by the mercury intrusion method. Both samples were treated for salt removal; the samples were immersed in pure water in a desiccator and degassed, and this operation was performed three times, replacing with fresh water.

3.3.3. X-ray computed tomography (CT) imaging

The internal microstructure of the fault gouge and host rock sample was observed by X-ray CT (XT H225 ST, Nikon). The acceleration voltage was 150kV. Particle size was analyzed from the obtained CT images using ImageJ.

3.3.4. XRD patterns simulation

NEWMOD (Reynolds, 1985) was used to calculate XRD patterns for mixed-layered clays. The calculated conditions were: illite:smectite = 40:60, Reichwite parameter (*R*) = 0, K per half unit lattice = 0.8, and Fe = 0. The number of clay unit layers stacked ranged from 2 to 11.

3.4. Results

To examine the internal structure of the samples, I performed a nondestructive X-ray CT observation for the gouge sample (FG01) and host rock (SRK03). Although the host rock appears dense and nearly homogeneous (Fig. 3.2a), the image shows relatively bright seams that appear to be randomly developed, which may be immature deformation bands or sedimentary structures. The bright particles distributed in the CT images are thought to be quartz and plagioclase crystals based on mineral compositions from XRD analysis (Kameda et al, 2013). In addition, dark regions of a few micrometers in size are scattered, which may correspond to macropores.

Figure 3.2b shows an example of a CT image of a fault gouge. In this image, as in the host rock, bright particles and dark regions are universally observed. The major difference from the host rock is the presence of several cracks, which may have developed during the drying process prior to observation. Figure 3.2c shows the results of measuring the grain size of bright particles (quartz and feldspar particles) in the fault gouge and host rock using a number of CT images. In this procedure, particles ranging from 30μm to 300μm were counted. The mean and median particle sizes of the fault gouge and host rock were 72, 78 μm and 61, 64 μm, respectively; therefore, these analyses did not identify significant variation in particle size between the gouge and host rock.

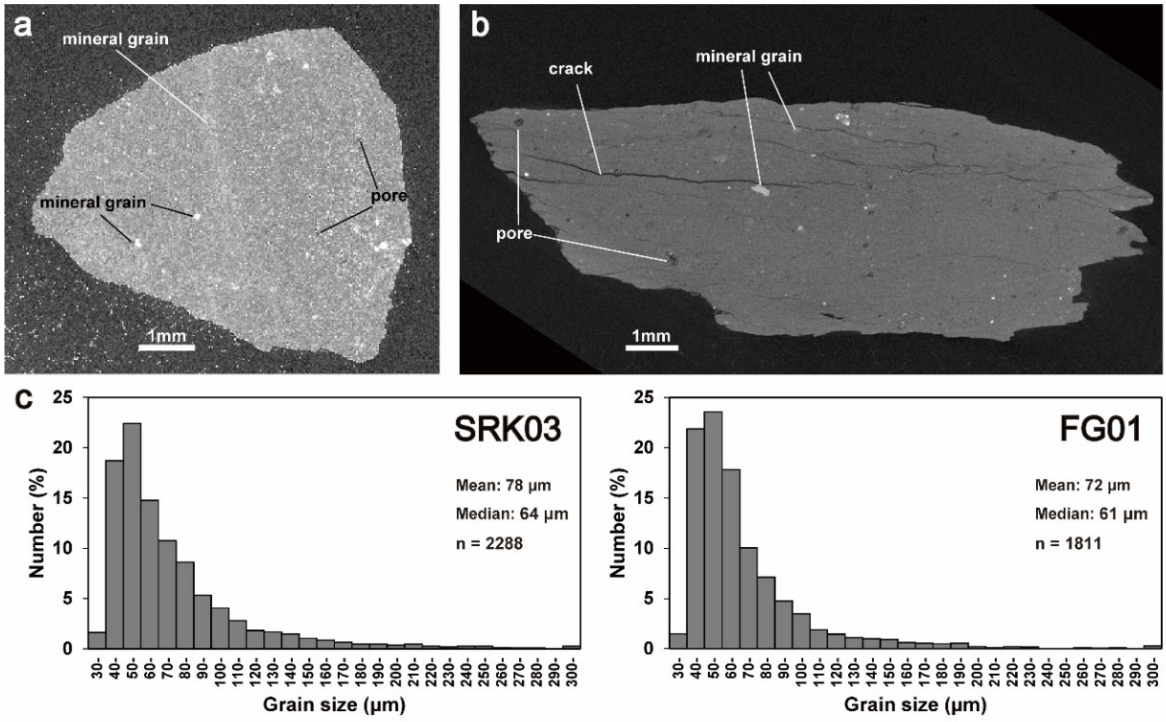

Figure 3.2. (a) XCT image of the host rock. (b) XCT image of the fault gouge. (c) Grain size distrubution of the samples.

Figure 3.3 shows typical nitrogen adsorption/desorption isotherms for the gouge (FG01) and the host rock sample (SRK03). Based on the ICPU classification (Sing, 1985), all samples show type IV isotherms, suggesting that the structure is rich in mesopores (2-50 nm). Comparing the isotherms of the fault gouge and host rock, hysteresis loops during adsorption and desorption paths are more pronounced in the former, and thus slit-like, somewhat bottlenecked pores are likely formed, classified as

intermediate between H2 and H3 types in further subdivision of the ICPU classification. The isotherm of the host rock, on the other hand, generally corresponds to the H3 type, and it is considered to be rich in slit-like pores. Table 3.1 shows the pore structure parameters calculated from the adsorption/desorption isotherms. The results of BET specific surface area from these isotherms are shown in Figure 3.4. In this figure, the horizontal axis indicates the distance from the gouge layer (positive numbers indicate the structurally upper direction). The specific surface areas of the host rock samples are somewhat variable, ranging from 30 to 60 m^2/g, while the fault gouge is distinctly higher than these values (80-90 m^2/g).

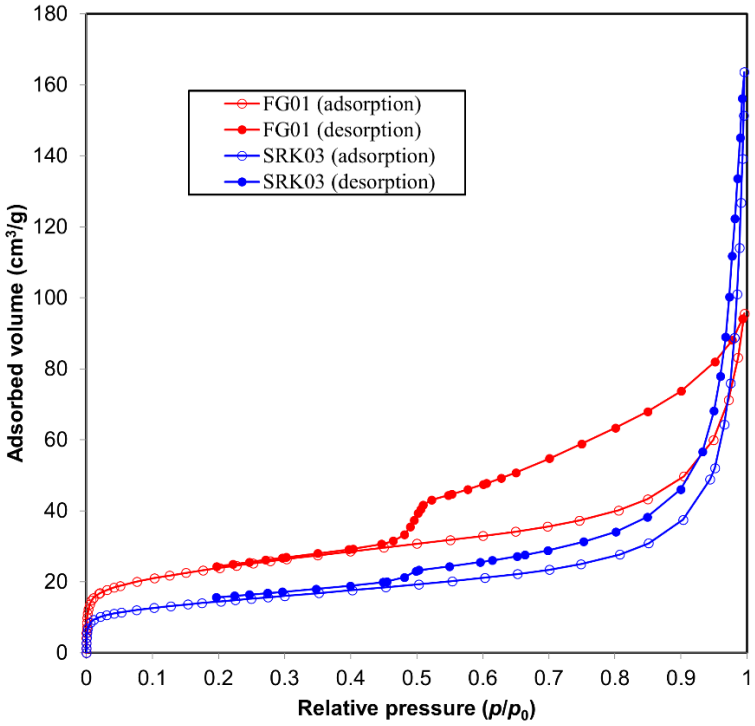

Figure 3.3. Typical isotherms of the host rock (SRK03) and the fault gouge (FG01).

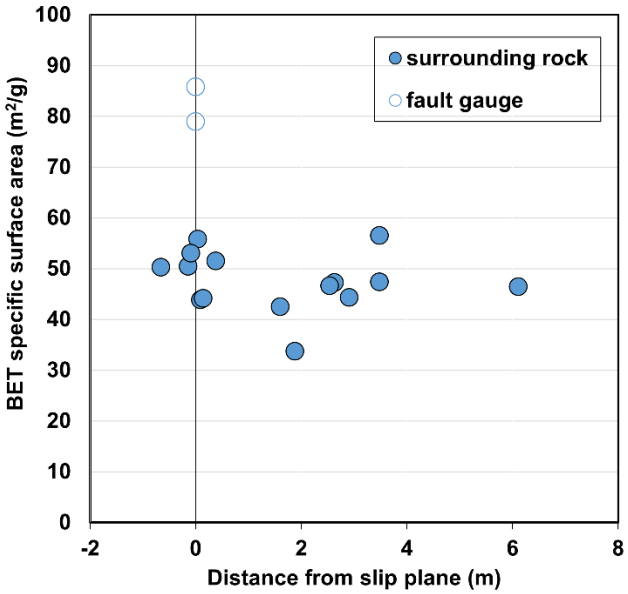

Figure 3.4. BET surface area variation as a function of distance from the slip plane. Solid blue circles show the host rocks. Open circles show the fault gouges.

Table 3.1. Results of pore structure parameters calculated from gas adsorption/desorption isotherms

Sample	Distance from fault (m)	BET specific surface area(m3/g)	Total pore volume (cm3/g)	Micropore volume (cm3/g)	Mesopore volume (cm3/g)	Saddle/peak (Kameda et al., 2013)
SRK01	2.91	44.31	0.135	0.007	0.060	0.664
SRK02	3.48	56.51	0.209	0.008	0.073	0.675
SRK03	0.38	51.54	0.239	0.008	0.070	0.708
SRK04	1.6	42.51	0.189	0.006	0.060	0.664
SRK05	2.63	47.25	0.213	0.007	0.065	0.644
SRK06	3.48	47.42	0.137	0.007	0.058	0.646
SRK07	1.88	33.71	0.143	0.005	0.046	0.666
SRK08	2.54	46.60	0.136	0.007	0.058	0.721
SRK09	-0.66	50.27	0.175	0.008	0.065	0.625
SRK10	6.11	46.45	0.216	0.007	0.063	0.573
SRK11	0.04	55.80	0.201	0.009	0.067	0.680-0.733
SRK12	-0.14	50.46	0.201	0.008	0.068	0.693
SRK13	0.09	43.85	0.169	0.007	0.053	0.607
SRK14	-0.09	53.05	0.245	0.008	0.069	0.691
SRK15	0.14	44.16	0.187	0.007	0.058	0.729
FG01	**0**	**85.77**	**0.144**	**0.016**	**0.076**	**0.876-0.908**
FG02	**0**	**78.99**	**0.154**	**0.015**	**0.081**	**0.855-0.894**

Figure 3.5 shows the respective PSDs (differential pore volume distribution; red line) obtained from isotherms of the gouge sample (FG01) and host rock (SRK03 and SRK12) calculated from the BJH method. The host rock samples show a nearly constant value (0.02-0.03 cm^3/g) up to about 10 nm, followed by a marked increasing trend toward a peak of about 100 nm (0.14-0.18 cm^3/g). On the other hand, the fault gouge sample shows a maximum of 0.08 cm^3/g at 50-60 nm, but its volume is about half that of the host rock. Furthermore, for relatively small pores (1-3 nm), the fault gouge is characterized by higher values (0.05-0.06 cm3/g) than the host rock (about twice as high). For pores larger than a few tens of nm, it is noted that the mercury injection method provides a more appropriate estimate than the gas adsorption method (e.g., Kuila and Prasad, 2013). Figure 3.5 also shows the PSDs obtained by the mercury injection method (blue line). In the mercury injection method, distinct peaks are also observed at approximately 100 nm in the host rock and 50-60 nm in the fault gouge. However, the height of the peak is two to three times greater than the value obtained by the gas adsorption method, suggesting that the gas adsorption method does not adequately measure some of these pores. The peak height of the fault gouge is approximately half that of the host rock in the mercury injection method, and this trend is consistent with that obtained by the gas adsorption method.

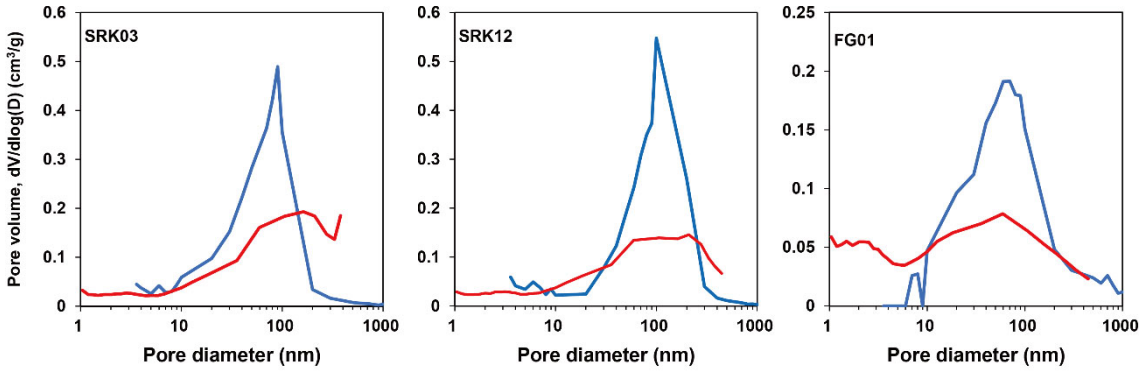

Figure 3.5. Pore size distributions of the host rocks (SRK03, SRK12) and the fault gouge (FG01) from the N_2 gas adsorption method (red line) and MICP (blue line).

3.5. Discussion

3.5.1. Selective clay particle fracturing and nanopore formation by shear deformation of the Shirako Fault

The present nanopore analysis of the Shirako Fault shows that in the fault gouge, pores of less than 10 nm are formed, while larger pores of about 100 nm are reduced. The mercury injection method also showed a decrease in pore volume with a size of about 100 nm. These changes in pore structure may be related to the development and subsequent activity of the Shirako Fault. Yamamoto (2006) analyzed the physical properties of sediments during the formation of thrust systems within the Miura-Boso accretionary complex and reported a progressive decrease in pore volume and size from coherent units to fault zones and then to fault gouge. These changes are thought to be the result of fault formation and the subsequent increase in shear strain. Therefore, as Yamamoto (2006) pointed out, the decrease in the volume of relatively large pores (about 100 nm) and the shift of their position toward smaller ones (~60 nm) may be shear-induced compaction. One interesting aspect of the Shirako Fault is the distinct increase in specific surface area when compared to the surrounding host rocks. As noted above, the Shirako Fault has experienced thermal events in the past, which are inferred to have been caused by high-velocity seismic slip on the fault. When such coseismic deformation occurs, it is assumed that particle size reduction occurs due to high-velocity particle movement, collisions, and fragmentation within the shear zone (Monzawa and Otsuki, 2003), and such particle size reduction may be responsible for the increase in specific surface area of the fault gouge. However, grain size analysis of quartz and feldspar from the CT images indicates that there is no apparent size variation in the clasts between the gouge and host rocks (Fig. 3.2). This suggests that the fracturing of fine-grained clay particles, rather than quartz or feldspar, is occurring.

According to XRD analysis, the fault gouge and its host rocks are composed of about 70% clay mineral fraction, which includes I-S, kaolinite, chlorite and discrete illite (kameda et al., 2013). Among these clay phases, XRD peaks from I-S and kaolinite show distinctive differences between the fault gouge and host rocks. For example, in kaolinite, there is a marked decrease in peak intensity ratio relative to chlorite in the fault gouge. While previous studies have attributed this to partial decomposition of kaolinite due to thermogenesis (Kameda et al. 2013; Masumoto et al., 2018), the decrease in peak intensity may also be due to a decrease in domain size that results in coherent scattering of X-rays, so it can be thought of as a reduction in the number of stacking layers of kaolinite crystallites due to e.g., exfoliation. On the other

hand, for the I-S peak, it is reported that the saddle-peak intensity ratio in the low-angle region is larger in the fault gouge sample. Such an increase in saddle-peak intensity ratio has been theoretically shown to be caused by an increase in the proportion of illite layers in randomly interstratified I-S crystallites (Reynolds, 1992), and such changes have actually been reported in I-S that has undergone burial diagenesis or hydrothermal alteration (Inoue et al., 1989). However, since the saddle-peak intensity ratio can also vary depending on other factors such as the number of stacking layers of I-S crystallites, this interpretation requires caution. Here, I performed XRD pattern simulations using Newmod to examine whether changes in the number of stacking layers of I-S can explain the reported changes in the XRD patterns. According to Kameda et al. (2013), the saddle-peak intensity ratio for the host rocks of the Shirako Fault ranges 60-70%, while in the fault gouge this index increases to over 85%. Figure 3.6 shows the results of the Newmod calculation and how the saddle-peak intensity ratio varies as a function of the number of stacking layers of I-S crystallites. This simulation suggests that the number of layers in the host rock is about 6 to 10, and if it were delaminated and reduced to about 3 layers, the observed change in XRD patterns could be reasonably reproduced. This means that the change in the XRD pattern in the fault gouge can be explained solely by mechanical exfoliation due to shear deformation. As mentioned above, the formation or increase of <10 nm nanopores is evident in the fault gouge (Fig. 3.3), and such small pores have been interpreted as corresponding to turbostratic stacking of clay elementary units (Kuila and Prasad, 2013). Therefore, if the exfoliation of kaolinite and I-S due to shear deformation and the subsequent formation of nanopores occurs, it would also explain the the increase in specific surface area. Furthermore, when partial exfoliation occurs inside the clay particles, the formation of bottlenecked pores is expected, which is consistent with the shape of the isotherm described above. A schematic summary of these processes is shown in Figure 3.7.

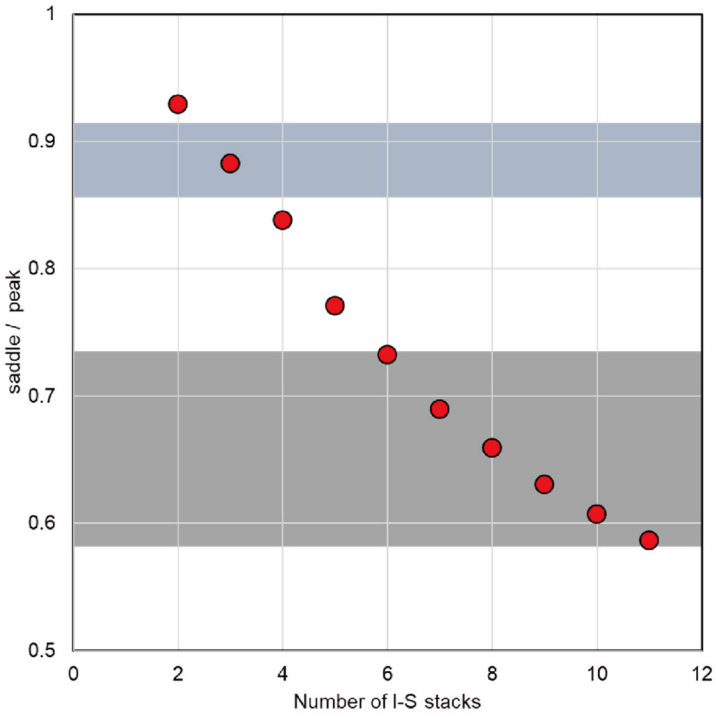

Figure 3.6. Variation of saddle/peak ratio with the number of unit layers in I-S crystallites calculated by Newmod. The gray and blue areas correspond to range of values for the host rock and fault gouge values, respectively (Kameda et al., 2013).

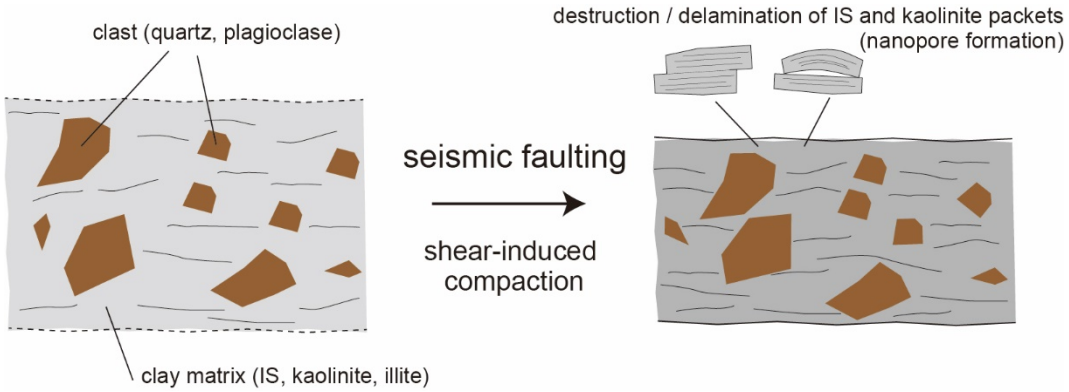

Figure 3.7. Conceptual model of pore structure changes due to fault slip on the Shirako Fault.

However, the above interpretation assumes an extreme case with no exothermic effects, and in fact it is highly likely that thermal events have occurred on the fault based on the increase in vitrinite reflectance values (Hamada, 2011). Therefore, I cannot

rule out the possibility that the thermally activated processes, kaolinite decomposition and I-S illitization, were driven by such exothermic events. In addition, mechanical action on clay particles has the effect of lowering the activation energy of the thermal activation process (Vroljik and van der Pluijm, 1999;), which may promote the reaction to a greater extent in faults than in static environments. In the fault gouge, these may have occurred in a complementary manner, and further quantitative evaluation of the contribution of each process is needed in the future.

3.5.2. Implications for coseismic deformation

When the 2011 Tohoku-Oki earthquake occurred at the Japan Trench, a large tsunami was generated due to coseismic high-velocity slip on a shallow subduction zone fault (Chester et al., 2012; Chester et al., 2013). In recent years, it has been pointed out that other subduction zones, such as the Nankai Trough and off Costa Rica, may have experienced seismic slip that reached the trench in the past (Sakaguchi et al., 2011; Vannucchi et al., 2017). Therefore, understanding deformation processes, especially coseismic slip process on shallow subduction zone faults is important from the perspective of such geohazard risk assessment. Rupture and slip propagation processes of a fault are controlled by the balance between elastic strain energy and dissipated frictional or rock fracture energy and elastic wave emission. The Shirako fault is expected to exhibit intrinsically low frictional strength because clay minerals are the major constituent material (Kameda et al., 2013). In addition, the CT images show no evidence of distinct particle (e.g., quartz or feldspar) fracturing, which may have suppressed the dissipation of fracture energy during fault activity, and further may have facilitated coseismic slip propagation. On the other hand, selective fracturing of clay particles occurred on the Shirako Fault. Interestingly, illite peaks from previous XRD studies has shown no apparent change in the width at half maximum between the host rock and the gouge (Kameda et al., 2013), suggesting that no exfoliation or other modification have occurred in the illite crystals. The interlayer bonding energy (ILBE) of various clay minerals have been calculated based on simple electrostatic forces by Giese et al. (1974; 1978). According to this calculation, ILBE of kaolinite is ~-1.1 J/m^2, which is about twice the value of the energy in muscovite (~-0.5 J/m^2), which has a similar crystal structure to illite, indicating that more energy is required for exfoliation. However, recent re-estimates based on quantum chemical calculations have shown that the ILBE of muscovite remains almost the same, while the energy of kaolinite decreases significantly (-0.1~0.15 J/m^2; Sakuma and Suehara, 2015). This result is in good

agreement with the fact that exfoliation was more pronounced in kaolinite and I-S crystals (and perhaps at the weaker-bound smectite layers within I-S packets) rather than illite in the Shirako Fault. In any case, these energies are smaller than the fracture energies of quartz and feldspar minerals (1-10 J/m^2; Sholz, 2002).

In the fault gouge, shear-induced compaction occurs, similar to that noted by Yamamoto (2016), and this may also contribute to changes in permeability structure around the Shirako Fault. Because such a reduction in permeability increases the likelihood of driving thermal pressurization during frictional heating (i.e., thermal expansion of pore fluid increases fluid pressure and correspondingly reduces shear strength; Sibson, 1973), triggering of these processes may have promoted high-velocity slip on this fault. On the other hand, in the fault gouge, nanopores of >10 nm are formed by clay exfoliation, but it is not clear how the formation of such pores contributes to changes in the retention/diffusion of fluids in fault zone, and it is necessary to evaluate the permeability of these samples experimentally in the future.

3.6. Conclusion

This study revealed the following:

(1) Gas adsorption/desorption measurements of the Shirako Fault gouge and host rock indicate that slit-like nanopores are generally developed in these samples. Combined with the mercury injection experiment, the results indicate that nanopores less than 10 nm are increased in the fault gouge, while pores of about 100 nm are decreased in volume and pore size. The specific surface area was clearly larger in the fault gouge than in the parent rock.

(2) CT imaging showed the internal structure of the gouge, such as the evenly distributed quartz and plagioclase particles and voids larger than a few microns. Measurements of particle size (e.g., quartz and feldspar) in the gouge and host rock showed no apparent difference between the two.

(3) XRD pattern simulations using Newmod of the mixed-layer smectite-illite show that decreasing the number of the stacking layers from ~6-10 to ~3 can reasonably explain the reported patterns of the fault gouge and host rock. Such a thinning of clay packets is probably caused by exfoliation due to fault activity, which is also consistent with the increase in specific surface area and formation of nanopores in the fault gouge. These findings suggest that the modification of clay phases in the

fault gouge may be influenced not only by thermal activation processes but also by mechanical fracturing.

(4) In the Shirako Fault, it appears that the particle fracturing of quartz and feldspar did not proceed, but rather selective fracturing of clays occurred, which may have suppressed energy dissipation due to fracturing and enhanced the propagation of high-velocity coseismic slip. The changes in the internal structure due to the formation of nanopores may also contribute to changes in the permeability structure around the fault and may also affect the faulting processes, which should be verified through future experiments.

Chapter 4 Surface physicochemical properties of smectite-rich fault gouge: A case study of the Japan Trench plate-boundary fault

4.1. Introduction

Smectite is one of the major clay minerals that constitute shallow crustal faults (Vrolijk and van der Pluijm, 1999). The frictional and other physicochemical properties of smectite, such as swelling and cation exchange capacity, have a strong influence on faulting behaviors, including seismogenesis (Logan and Rauenzahn, 1987; Moore and Lockner, 2007; Saffer et al., 2001; Kameda et al., 2016; Oohashi et al., 2017; Kameda and Hamada, 2020). The plate subduction boundary fault at the Japan Trench, which triggered the 2011 Tohoku-oki earthquake (Mw 9.0) and generated a huge tsunami, is characterized by smectite contents exceeding 60 wt.% (Chester et al., 2013; Kameda et al., 2015), suggesting that the physicochemical properties of smectite are important with respect to fault processes. For example, experiments have shown that such high smectite contents can locally generate high swelling forces within a fault that are nearly equivalent to the overburden load, which may result in very low fault strength conditions (Kameda et al., 2019). Previous rheological experiments using analog fault materials (a smectite–quartz mixture with brine) revealed that the slip behavior of faults can be approximated by flow deformation with a viscoplastic fluid (Kameda and Hamada, 2020). Moreover, Kameda and Hamada (2022) proposed that the time-evolving microstructure and organization of clay particles may cause a fault zone to become thixotropic, which in turn may be related to the periodic unstable slip motion of the involved fault. In general, such rheological properties of clay–water systems depend strongly on the interaction forces between clay particles. This kind of microscopic force is described within the framework of DLVO (Derjaguin and Landau, Verwey, and Overbeek) theory (Derjaguin and Landau, 1941; Verwey and Overbeek, 1948), which consists of repulsive electric double layer (EDL) forces and van der Waals attraction between clay particles. This framework, although classical, has been successfully applied to evaluate the stability of dispersion systems and their rheological parameters, such as yield stress (Otsuki, 2018) and viscosity (Duran et al., 2000; Montoro and Francisca, 2019). Therefore, the microscopic properties of clay particle surfaces, especially surface charge states, are also considered to be important for understanding

fault behaviors. In recent years, it has become increasingly acknowledged that the microscopic properties of the clay–water system govern the generation and dynamics of landslides (Plaza et al., 2018; Kameda, 2021; 2022), but this perspective has not yet been established with respect to understanding the dynamics of crustal faulting.

In this study, the surface free energy of solid particles was determined from contact angle measurements of probe solutions of core samples recovered from the Tohoku-oki fault zone. Using the obtained surface free energies and the zeta potential, which is the electric potential at the slip surface in the EDL of particles in aqueous solution measured by Nakamoto et al. (2023), the interaction forces between particles were then assessed by using an extended form of DLVO theory that includes the acid–base contribution (i.e., electron donor–acceptor interactions) in addition to the other forces described above (Van Oss, 1994). On the basis of the results, I argue that the surface properties of clay particles play an important role in the slip behavior of the studied fault.

4.2. Samples

The Mw9.0 Tohoku-oki earthquake occurred in the Japan Trench on 11 March, 2011. Slip of up to ~50 m along the plate-boundary fault propagated to the trench (Ide et al. 2011; Fujii et al. 2011; Fujiwara et al. 2011; Kodaira et al. 2012), generating a huge tsunami. One year after the earthquake, deep-sea drilling by the Integrated Ocean Drilling Program (IODP Expedition 343 JFAST program) was conducted to directly investigate the shallow source fault of the earthquake (Fig 4.1a; Chester et al. 2012, 2013). The drilling at site C0019E, 5 km landward from the trench axis, identified a <5-m-thick plate-boundary fault zone at ~820 m below the sea floor (mbsf; Fig. 4.1b) and recovered a 1.2-m-long core sample from the fault zone. Mineralogical analyses have revealed that the fault zone is marked by extremely high smectite contents (60–80 wt.%) compared with surrounding sequences (<20 wt.%; Fig. 4.1b; Kameda et al. 2015). Analysis by the Schollenberger method (extracting cations in ammonium acetate solution) has also shown that the exchangeable cations of smectite are enriched in Na (Kameda et al., 2016). In this study, a total of 10 fragments from various parts of the fault zone were used for laboratory measurements, as described below (Fig. 4.1b).

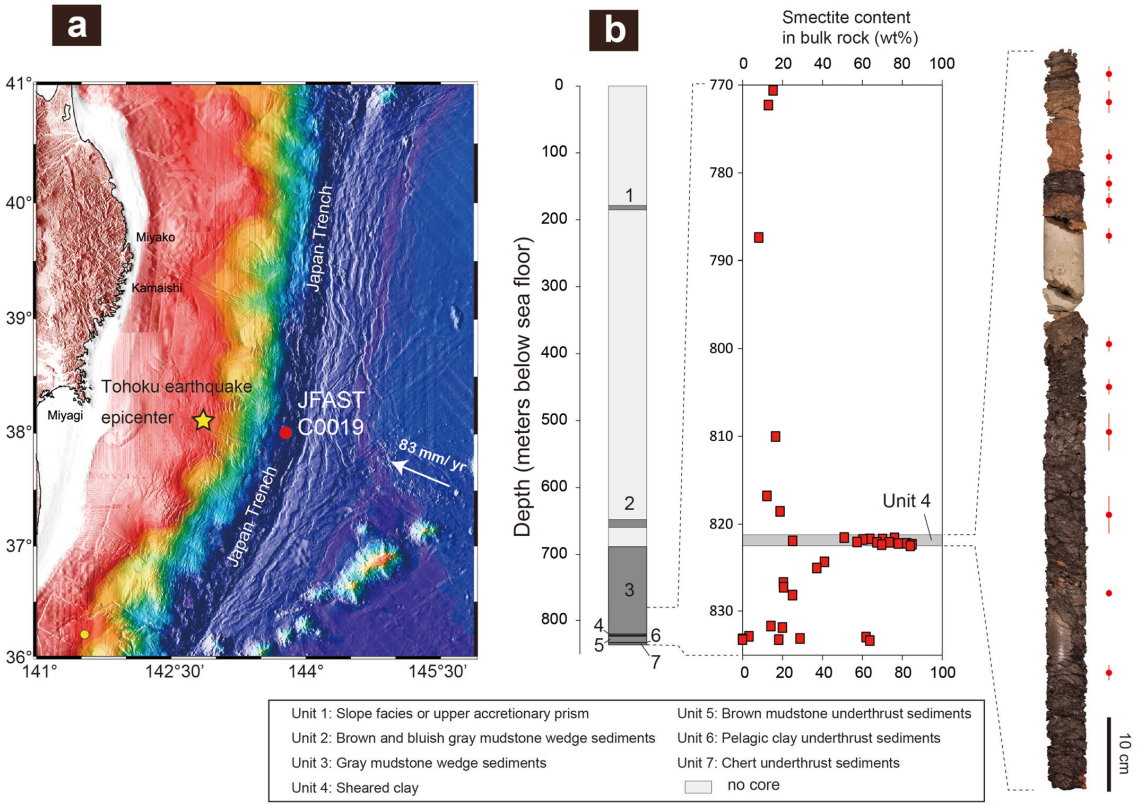

Figure 4.1. (a) Location of the JFAST drill site (Site C0019; modified from Kimura et al. 2012). (b) Lithological units at the JFAST drill site and variation in the bulk-rock smectite content. Red circles along the 17R core image depict the locations of samples analyzed in this study.

4.3. Methods

4.3.1 Measurement of zeta potential

The zeta potential ζ of the samples was estimated by electrophoretic light scattering using a Zetasizer Nano instrument (Malvern). For electrophoresis, the samples were dispersed in three types of solutions—distilled water, 0.5 M NaCl solution, and simulated solutions—for the extracted pore fluid of the fault gouge during the drilling survey (Na+ = 455.8 mM, Ca2+= 24.7 mM, K+= 7.7 mM, and Mg2+= 37.8 mM; Kameda et al. 2016) at a solid weight concentration of ~0.1%. The dispersions were then sonicated and disaggregated for 10–15 min before measurement (Kamei, 2023).

The zeta potential was obtained from the electrophoretic mobility μ of each sample based on the Smoluchowski relationship (Smoluchowski 1921), as follows:

$$\mu = \frac{\varepsilon_0 \varepsilon \zeta}{\eta}, \qquad (1)$$

where ε_0 is the vacuum permittivity (8.854×10^{-12} F/m), ε is the dielectric constant of water (78.4), and η is the viscosity of the solution (0.8872 mPa·s).

4.3.2. Determination of surface free energy

The surface free energy of a solid or liquid γ_k is described as the sum of the Lifshitz–van der Waals component, γ_k^{LW}, and the Lewis acid–base interaction, γ_k^{AB}, of phase k (e.g., Van Oss, 1994):

$$\gamma_k = \gamma_k^{LW} + \gamma_k^{AB}. \qquad (2)$$

In general, the polar acid–base interaction is caused by electron-donor (γ^-) and electron-acceptor ($\gamma+$) contributions:

$$\gamma_k^{AB} = 2\sqrt{\gamma_k^+ \gamma_k^-}. \qquad (3)$$

These correlations, combining Young's equation, lead to the following expression for a solid–liquid interface:

$$\gamma_{Li}(1+\cos\theta) = 2\sqrt{\gamma_S^{LW}\gamma_{Li}^{LW}} + 2\sqrt{\gamma_S^+\gamma_{Li}^-} + 2\sqrt{\gamma_S^-\gamma_{Li}^+}, \qquad (4)$$

where γ_{Li} is the surface tension of liquid i; θ is the contact angle on the solid; and γ_{Li}^{LW}, γ_{Li}^+, and γ_{Li}^- are the surface free energy components of the liquid. Thus, the three unknown variables for the solid surface, that is, γ_S^{LW}, γ_S^+, and γ_S^-, in Equation (4), can be calculated by contact angle measurements using at least three liquids of known surface free energy components.

In this study, the flat surface of one sample (17R-1_58–63cm) was prepared by dropping its suspension onto a glass slide and drying at 60 °C overnight. The contact angles, θ, of three probe liquids (diiodomethane, ethylene glycol, and water) on this surface (i.e., the angle between the tangent line of each droplet and the solid surface) were measured using a contact angle meter (B100W, ASUMI GIKEN). Five measurements were performed for each probe solution.

4.4. Results

Figure 4.2 shows the change in zeta potential of the analyzed 10 samples under three different dispersants (Kamei, 2023). In distilled water, the samples show potential values between −40 and −50 mV, whereas they range from −20 to −25 mV in 0.5 M NaCl (Table 4.1). These potential values and the decrease in potential in solutions with higher ionic strength are consistent with the reported behavior of Na-type smectite (Delgado et al. 1985). In the simulated porewater solution, the zeta potential of the samples is somewhat lower than that in 0.5 M NaCl, in the range of −10 to −20 mV. The pH values of the experimental samples were generally neutral (6-8), but when the values in pure water, salt water, and simulated pore water were compared, the latter tended to have a higher pH (Table 4.2). Therefore, in addition to ionic strength, the effect of these pH differences is also likely to be reflected in the measured zeta potentials.

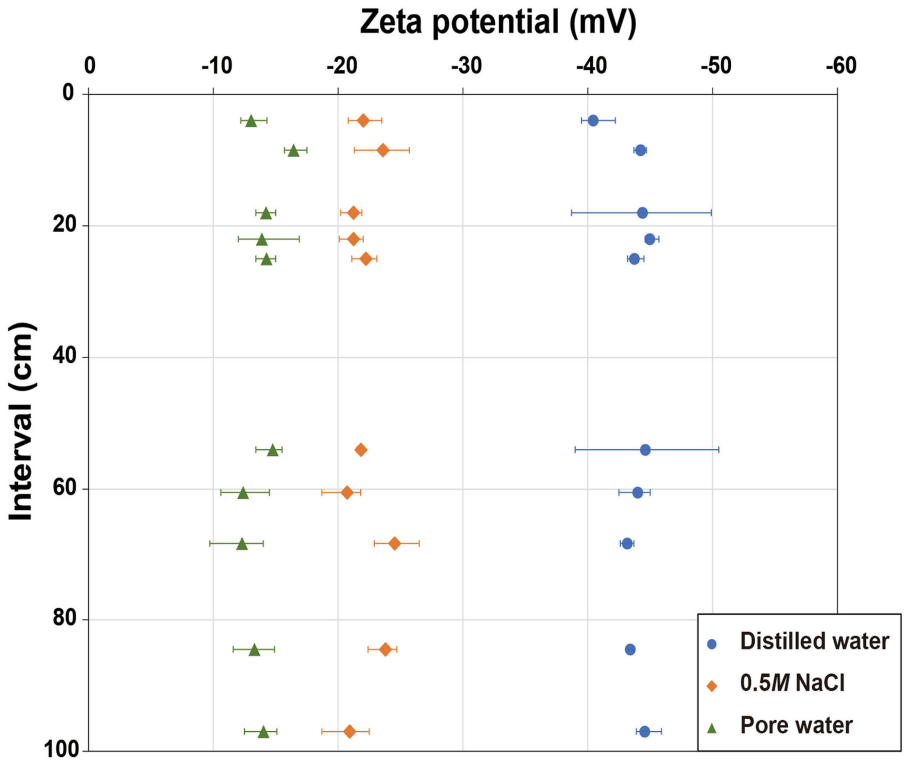

Figure 4.2. Zeta potential of the analyzed 10 samples in three different dispersants (distilled water, 0.5 *M* NaCl solution, and simulated pore water) (Nakamoto et al., 2023).

Table 4.1. Surface free energy components of the solid surface (mJ/m^2)

γ_S^{LW}	γ_S^+	γ_S^-
43.42	0.77	53.08

Table 4.2. Results of zeta potential measurements (Nakamoto et al., 2023)

Sample (cm)	H2O				0.5 M NaCl				Simulated pore water			
	Zeta Potential (mV)			pH	Zeta Potential (mV)			pH	Zeta Potential (mV)			pH
	1	2	3		1	2	3		1	2	3	
3_5	-39.6	-42.2	-39.5	7.64	-23.5	-21.8	-20.8	6.53	-12.6	-12.2	-14.3	6.28
7_10	-44.7	-44.3	-43.7	7.71	-23.8	-21.3	-25.7	6.34	-17.5	-15.7	-16.1	6.03
*17_19	-48.7	-49.9	-47.6	7.30	-21.6	-21.9	-20.2	6.11	-15.0	-14.3	-13.4	5.78
	-39.4	-38.7	-42.0									
21_23	-45.7	-44.6	-44.6	7.94	-22.0	-21.6	-20.1	6.40	-12.8	-12.0	-16.9	6.11
24_26	-44.5	-43.2	-43.5	7.36	-22.5	-23.1	-21.1	6.60	-13.4	-14.4	-15.0	6.13
*53_55	-49.9	-50.5	-48.3	7.75	-21.5	-22.1	-21.9	6.64	-15.5	-13.4	-15.4	6.23
	-41.0	-39.0	-39.0									
58_63	-45.0	-42.5	-44.5	7.81	-21.8	-18.7	-21.7	6.53	-10.6	-14.5	-12.1	6.21
67.5_69	-42.6	-43.7	-43.2	7.73	-24.2	-26.5	-22.9	6.53	-14.0	-9.7	-13.2	6.21
84_85	-43.6	-43.2	-43.4	7.90	-24.7	-22.4	-24.3	6.73	-14.9	-11.6	-13.4	6.43
96_98	-45.9	-43.9	-43.9	7.73	-21.6	-18.7	-22.5	6.62	-12.5	-15.1	-14.5	6.21

*Two different suspensions were measured

The average values of five contact angle measurements with diiodomethane, ethylene glycol, and water were 31.89°, 8.44°, and 12.02°, respectively (Table 4.3). From these values and Eq. (4), γ_S^{LW}, γ_S^+, and γ_S^- of the fault sample were calculated to be 43.42, 0.77, and 53.08 mJ/m^2, respectively (Table 4.1). These energy values are also reasonably consistent with those of Na-type montmorillonite (Duran et al., 2000).

Table 4.3. Results of contact angle measurements

Probe liquid	1	2	3	4	5	average	SD
water	10.31	10.42	12.44	13.07	13.87	12.02	1.43
diiodomethane	31.47	31.66	31.3	31.89	33.12	31.89	0.65
ethylene glycol	8.71	8.44	8.32	9.25	7.5	8.44	0.57

Figure 4.3 shows the results of PSD analyses obtained from the BJH method. The two samples show similar PSD profiles (partial volume of each pore diameter), with a subordinate peak in pore volume at around 2−3 nm diameter and a major peak at around 50–60 nm. These peaks are likely attributed to micropores formed by turbostratic

stacking of clay elementary units (e.g., voids at the edges of particles formed by stacking disorders of clay elementary layers) and mesopores owing to stacking of clay particles or aggregates, respectively (Kuila and Prasad, 2013).

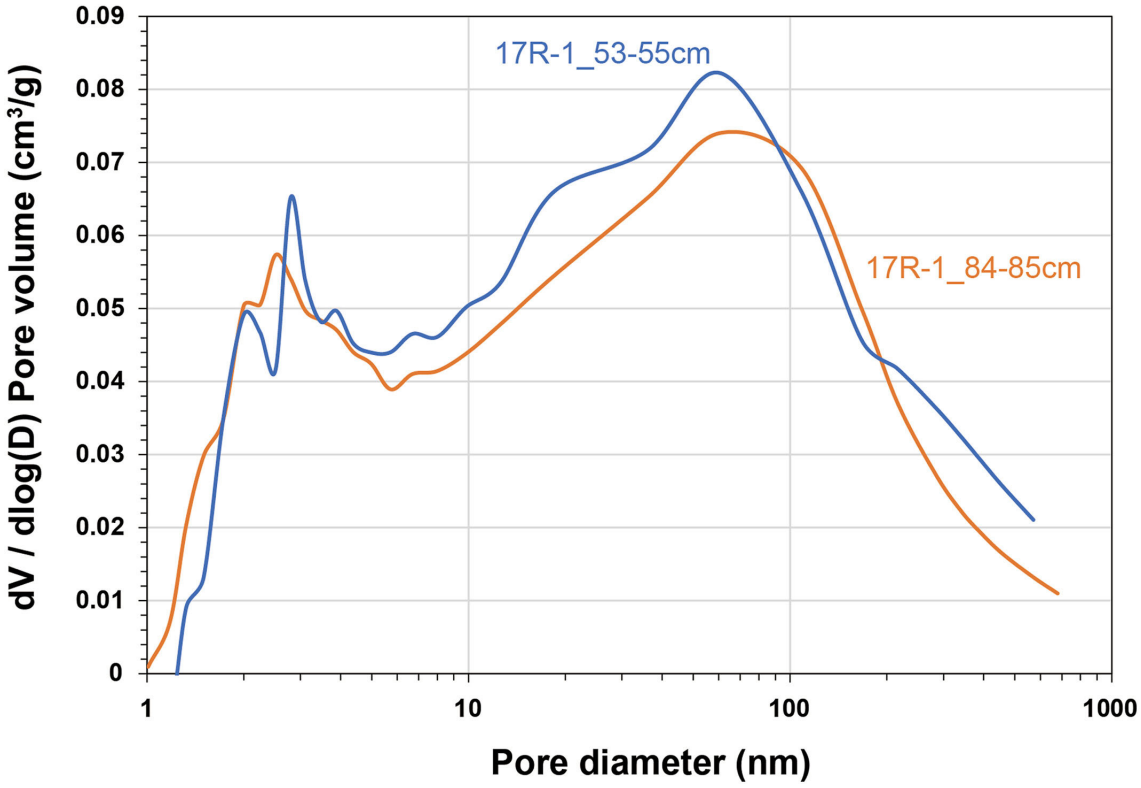

Figure 4.3. Pore size distribution curves of the two analyzed core samples obtained from BJH analysis.

4.5. Discussion

The analysis of the surface properties of the fault samples yielded values that correspond closely to Na-type smectite. This is explained by the very high contents of smectite in the fault (Kameda et al., 2015) and by the fact that the exchangeable cations of smectite are mainly Na (Kameda et al., 2016). In this section, I further examine the interparticle interactions in the in situ fault by adopting the parameters obtained from the analyses. For this purpose, as described above, extended DLVO theory is used to account for EDL and van der Waals forces, as well as structural or hydration forces, that cannot be ignored in interactions between particles with hydrophilic surfaces, such as clays (Van Oss, 1994). The repulsive energy due to EDL interaction between parallel

plates is calculated according to the following expression (Hogg et al., 1966; Israelachvili, 2011):

$$V_R^{EDL} = \frac{\varepsilon_0 \varepsilon \kappa}{2}[(\Psi_1^2 + \Psi_2^2)(1 - \coth\kappa H) + 2\Psi_1\Psi_2 \mathrm{cosech}\kappa H], \quad (5)$$

where κ is the reciprocal Debye length ($(1/\kappa = 0.304/\sqrt{[\mathrm{NaCl}]}$ nm for 1:1 electrolyte; Israelachvili, 2011), and H is the separation distance between particles. Here, the measured zeta potential ζ is used for the surface potential Ψ (Duran et al., 2000). The plates in the system are identical; therefore, $\Psi_1 = \Psi_2$.

The Lewis acid–base component of the surface free energy causes another source of repulsive interaction between the particles; i.e., so-called hydration or structural forces. The interaction energy is described as a function of H as follows:

$$V_R^{AB} = V^{AB}(H_0) \exp\left[\frac{H_0 - H}{\lambda}\right], \quad (6)$$

where λ is the correlation length of water molecules and is generally assumed to be 1 nm for hydrophilic surfaces (Van Oss, 1994). The preexponential factor of Equation (6) is calculated from the surface free energy of the phases involved:

$$V^{AB}(H_0) = 2\left[\sqrt{\gamma_L^+}\left(2\sqrt{\gamma_S^-} - \sqrt{\gamma_L^-}\right) + \sqrt{\gamma_L^-}\left(2\sqrt{\gamma_S^+} - \sqrt{\gamma_L^+}\right) - 2\sqrt{\gamma_S^+\gamma_S^-}\right]. \quad (7)$$

The Lifshitz–van der Waals attractive energy for two parallel plates is calculated by:

$$V_A^{LW} = -\frac{A}{12\pi H^2}, \quad (8)$$

where A is the Hamaker constant. If $\gamma\gamma_k^{LW}$ is known for the relevant system, the Hamaker constant can be determined as follows:

$$A = -24\pi H_0 \left[2\sqrt{\gamma_S^{LW}\gamma_L^{LW}} - \gamma_S^{LW} - \gamma_L^{LW}\right], \quad (9)$$

where H of 0.158 nm is a reasonable value for a variety of systems (Van Oss, 1994).

Substituting the energy values into Equation (9) obtained (Table 4.2) yields 6.94×10^{-21} J for the Hamaker constant, which is consistent with that of Na-type smectite (~7.0×10^{-21} J; Duran et al., 2000).

The net particle interaction energy V is determined from Eq. (5), Eq. (6) and Eq. (8) as follows:

$$V = V_R^{EDL} + V_R^{AB} + V_A^{LW}. \quad (10)$$

This can be differentiated to obtain the net force between particles (positive sign is repulsion):

$$F = -\frac{dV}{dH}. \quad (11)$$

Figure 4.4a shows an example of energy calculation for particles in the moderate salinity case (10^{-2} M and $\zeta = -35$ mV). The total energy increases markedly as the interparticle distance approaches ~10-20 nm, which is caused mainly by the pronounced increase in EDL-related and AB-related interactions. On the other hand, above 20 nm, the total energy decreases significantly and becomes negative due to LW-related interactions in addition to the decrease in EDL-related interactions. Figure 4.4b shows how the total energy and force varies with respect to solution condition, as well as the zeta potential of the clay surfaces. In the calculation for the high-salinity condition (0.5 M), the zeta potential was conservatively set at −15 mV because we assumed the fault zone condition (Fig. 3.2). In this case, the energy decreases more sharply than in the low ionic strength case at around 10 nm distance, shows a potential well at ~12 nm, and increases and gradually shifts to a lower energy state as the separation distance increases. This local minimum is an energetically stable state in which the force between the particles is zero; if the distance between the particles increases, an attractive force acts, and conversely, if the distance decreases, a repulsive force acts (red dotted line in Fig. 4.4b). In the case of the low-ionic-strength solution (10^{-3} M and ζ = −45 mV), the total energy is very large and positive due to the EDL related repulsive force, and such repulsive forces act down to around 80nm.

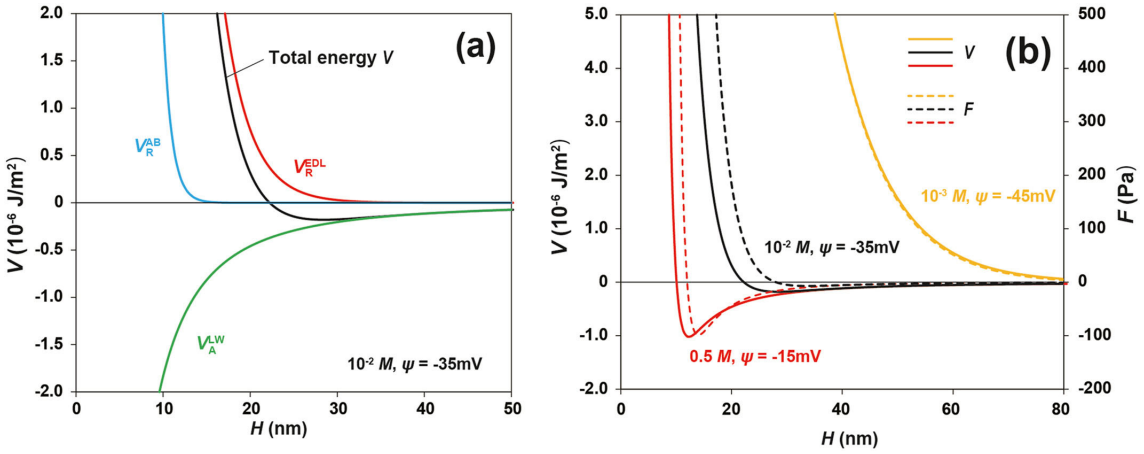

Figure 4.4. (a) Potential energy of interactions between smectite particles as a function of their separation distance, *H*. Contribution to potential energy of interaction from acid–base (AB) interaction V_R^{AB}, electric double layer interaction V_R^{EDL}, and Lifshitz–van der Waals (LW) interaction V_A^{LW}. (b) Potential energy (*V*) and force (*F*) of interactions between smectite particles as a function of their separation distance, *H*, at three different solutions.

As nano to mesopores observed in gas adsorption analyses likely correspond to the voids between clay aggregates, I consider the distribution of interparticle distances based on the PSD data (Fig. 4.3). The PSD curves show that the distances between particles within the fault zone vary from a few nm to several tens of nm but are characterized most distinctly by a pronounced peak at 50–60 nm. It should be noted, however, that in the gas adsorption measurements, the samples were heat-dried as a pretreatment, so individual smectite layers are considered to have dehydrated and shrunk to a d = 1.0 nm state; in the actual fault zone beneath the seafloor, smectite layers are expected to have absorbed water and swollen to ~1.2 or 1.5 nm (Brown and Ransom, 1996; Fitts and Brown, 1999; Fig. 4.5). This means that the distances shown in Figure 4.3 may be overestimated by ~20%–35%. However, even after subtracting such effects, the majority of the interparticle distances are expected to be a few tens of nanometers (the mode of distance is ~35 to ~50 nm after subtraction of the swelling effect). In this case, it is assumed that weak attractive forces are acting between most of the smectite particles (Fig. 4.4b). If the fault were filled with extremely low-ionic-strength fluid, such as ~10^{-3} M, then the strong EDL force would cause a large repulsive force to act between the particles (solid black line in Fig. 4.4b). This strong EDL force is due to the far extension of the EDL around the particle (i.e., long Debye

length), and when relative motion occurs between particles in such a state, the interaction between ionic clouds (e.g., overlapping and their distortions) occurs as a stronger viscous resistance force (i.e., the electroviscous effect; Rubio-Hernández et al., 2004; Montoro and Francisca, 2019) and thus contribute to the suppression of fault sliding. In contrast, where salinity is high, as in the case of the Tohoku-oki Fault, the interparticle energy is very low (solid red line in Fig. 4b), and this may have contributed to a reduction in viscous resistance and thus facilitated fault slip. A substantial decrease in the viscosity of the smectite suspension at high salt concentrations has been observed in several rheological experiments (e.g., Kameda and Morisaki, 2017). Another important point to note is that under the high-salinity condition, the energy curve shows the presence of a potential well (Fig. 4.5b). As described above, this indicates that energetically stable states can exist in the particle configuration, which may give rise to the thixotropic nature of a fault, as noted in previous studies (e.g., Ren et al., 2021). The energetically stable structures with well relaxed particle configurations would be destroyed by the force caused by fault slip, at which time the average intergranular distance would increase (i.e., shear-induced dilation). It is not yet clear whether dilation associated with coseismic slip occurred on this fault, but slip zones are often less dense than the surrounding rock after an earthquake (Wu et al. 2008; Li et al. 2014). In the interseismic period after the seismic event, the structure will transition back to an energetically stable structure over time, which may correspond to the strength recovery process of a fault. In the analyzed samples, the average interparticle distance seems to be slightly larger than the energetically stable distance, which may represent a transitory state of structural relaxation. The breakdown and rejuvenation of these structures (i.e., thixotropic nature) can also cause spontaneous stick-slip motion of the fault (Kameda and Hamada, 2022). Therefore, the key to further validating the above implication would be to analyze changes in the microscopic state of a fault over time.

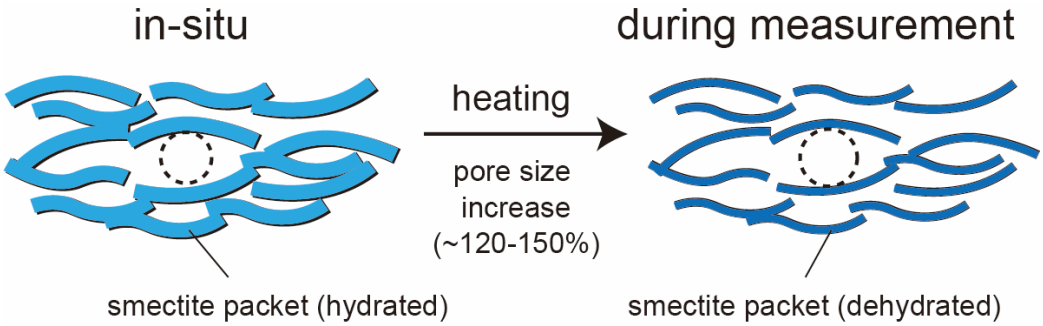

Figure 4.5. Illustration showing expected changes in fault rock and pore states under wet (in situ fault) and dry (during measurements) conditions.

Chapter 5 Swelling behavior of smectite–quartz mixed powder dispersed in salt water: an analog for smectite-bearing fault gouge in plate-subduction zones

5.1. Introduction

Smectite is a clay mineral that is widely distributed on or near Earth's surface as a weathering/alteration product in soils and shallow deposits. Smectite has a low intrinsic friction, and thus its influence on fault mechanics has been the focus of scientific attention (Logan and Rauenzahn, 1987; Saffer et al., 2001; Ikari et al., 2007; Moore and Lockner, 2007; Oohashi et al., 2015). In addition to characteristic frictional properties, smectite has several interesting physicochemical properties, such as cation exchange and swelling (Mitchell and Soga, 2005). In particular, the swelling capacity of smectite is thought to have a direct effect on the stress state of smectite-containing faults. On the basis of results of shear strength experiments on smectite soils, Chatterji and Morgenstern (1990) proposed the concept of "modified effective stress" (σ_n''), which can be represented as

$$\sigma_n'' = \sigma_n' - P_s, \qquad (1)$$

where P_s is the swelling pressure of smectite and σ_n' is the effective stress from Terzaghi's theory (Terzaghi, 1925), which is calculated as

$$\sigma_n' = \sigma_n - P_f, \qquad (2)$$

where σ_n is the normal stress and P_f is the fluid pressure. According to this relationship, the effect of the swelling pressure of smectite on the stress state of a fault is equivalent to that of the pore fluid pressure, suggesting that higher-swelling-pressure conditions result in a greater reduction in the strength of the fault. For example, Kameda et al. (2019) measured the swelling pressure of a smectite-rich plate-boundary fault at the tip of the Japan Trench and found that it was close to the in situ overburden stress applied on the fault. This finding indicates that the shear strength of this fault may be very low and that such a stress state may have contributed to the large fault slip during the 2011 Tohoku-oki earthquake. In fact, subsequent experiments have shown that the fault may have slipped with almost no effective stress acting on it (Kameda and Hamada, 2021). These observations suggest that the concept of effective stress can be applied to natural

faults. As smectite is ubiquitous in shallow-crustal faults (Vrolijk and van der Pluijm, 1999), it is important to characterize the swelling behavior of smectite to better understand the mechanical properties of faults.

Many studies have examined the effects of initial consolidation state, type and nature of smectite, and fluid composition on the swelling behavior of smectite and bentonite (e.g., Karnland et al., 2006; Komine et al., 2009; Zhu et al., 2013; Kaufhold et al., 2015). Swelling pressure can be explained by the Gouy–Chapman theory, which is based on diffuse double-layer repulsive interaction forces between plate-like smectite particles (Bolt, 1955; van Olphen, 1977; Tripathy et al., 2004). However, it is difficult to accurately estimate swelling pressure from such a theory under conditions of high salinity, such as in seawater (Komine et al., 2009). In addition, changes in swelling pressure in the presence of non-swelling minerals, such as in crustal faults, have not been systematically investigated.

In this study, swelling pressure experiments were conducted using samples simulating crustal fault zones, with a wide range of smectite contents from 20 to 80 wt.%. Experiments were performed under conditions of high salinity, as assumed for submarine faults at convergent plate margins, where the salinity of pore water is generally considered to be as high as that of seawater (e.g., the Japan Trench; Kameda et al., 2016). To evaluate the potential for swelling pressure generated by high smectite content layers to influence faulting behavior, experimental results in combination with constraints on material properties and conditions obtained from drilling are applied to plate-boundary sediments in Sumatra. Results of the study are expected to lead to a better understanding of the mechanical properties of smectite-bearing faults in plate-subduction zones.

5.2. Experimental methods

5.2.1. Sample preparation

Composite smectite–quartz powders were prepared by mixing commercially available Na-montmorillonite (Kunipia-F, Kunimine Industries, Japan) and crystalline quartz (silicon dioxide 199–00625; Fujifilm Wako Pure Chemicals, Japan) as a non-swelling mineral phase. The chemical composition of smectite using this study was reported as $Na_{0.42}Ca_{0.068}K_{0.008}(Al_{1.56}Mg_{0.31}Fe^{3+}_{0.09}Fe^{2+}_{0.01})(Si_{3.91}Al_{0.09})O_{10}(OH)_2$ (Ito et al., 1993). The smectite sample contains small amounts of quartz and calcite as impurities (1–2 wt.%; Ito et al., 1993). The sample was not heated to dehydrate, as such treatment may cause irreversible loss of swelling properties (Schleicher et al., 2015).

The quartz powder is composed of angular sand-sized grains (mean grain size of ~100 μm; Oohashi et al., 2015). The mixing ratio of these powders was varied, using smectite weight fractions of 80, 60, 40, and 20 wt.% (hereafter termed 80%Sm, 60%Sm, 40%Sm, and 20%Sm, respectively) to simulate fault gouge containing various fractions of smectite. The composite powder was homogenized by using a laboratory mixer.

5.2.2. Swelling experiments

Swelling experiments were conducted using the apparatus shown in Figure 5.1a. An amount of 0.3 g of composite powder, weighed under ambient temperature and humidity, was loaded into a cylindrical sample cell (Φ = 8 mm), following which the sample was pre-compacted to the desired porosity (the method for estimating porosity is described in Section 5.2.3). A solution of 0.6 M NaCl, comparable with seawater salinity, was introduced into the sample cell as a reacting fluid at a fluid pressure of 0.2 MPa. For 60%Sm, experiments with pure water were also conducted for comparison with experiments using brine water. The piston position was fixed to avoid any change in sample volume caused by swelling during the experiments.

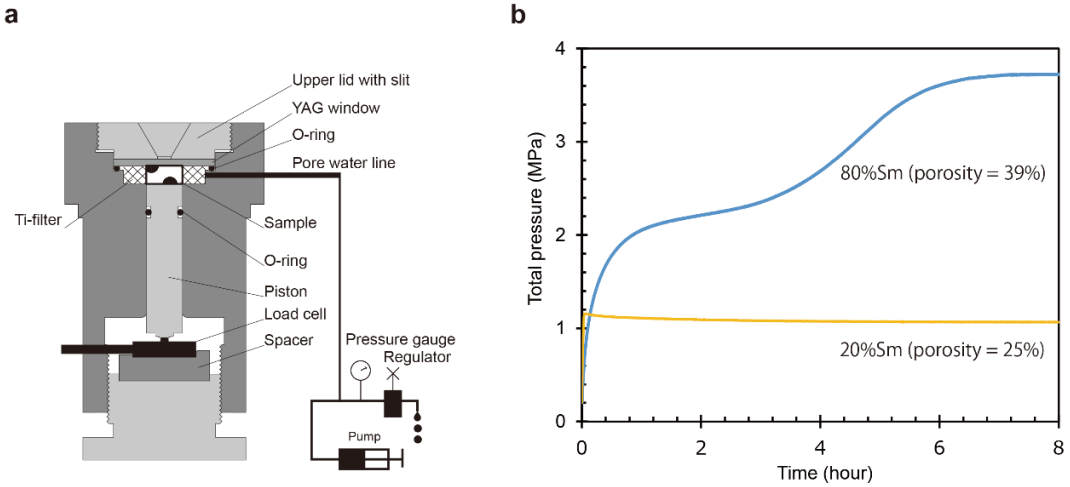

Figure 5.1. Apparatus and typical results of swelling-pressure experiments. (a) Schematic diagram of the test apparatus used in this study. (b) Typical swelling-pressure measurements for the samples with a high smectite content (80%Sm; blue line) and a low smectite content (20%Sm; yellow line). The fluid pressure used during the experiments was 0.2 MPa.

5.2.3. Porosity estimation

The porosity adopted for this study is the so-called “total porosity” (Conin et al., 2011), which is defined by the total volume of water in intergranular pore spaces and the mineral assemblage, as well as water adsorbed at mineral surfaces. Estimation of the total-porosity condition of each experiment required quantification of the initial water content in the smectite powder. For this purpose, the spacing of smectite layers at ambient conditions was measured by X-ray diffraction (XRD). A smectite 001 peak in the XRD pattern was observed at $2\theta = 7.2°$ ($d = 12.3$ Å), which suggests a one-layer hydration state (Keren and Shainberg, 1975). Smectite in this state contains 10 wt.% interlayer water (Miyawaki et al., 2010). Porosity was then estimated from the reading of the piston position and by adopting the density of quartz as 2.65 g/cm^3 (Deer et al., 1992) and that of dry smectite as 2.88 g/cm^3 (Tachi and Yotsuji, 2014).

5.3. Results

Figure 5.1b shows an example of the evolution of pressure from the time of immersion. For the sample with low smectite content (20%Sm), the pressure increases rapidly to the maximum value (1.1 MPa) within 4 min after the start of the experiment. Thereafter, pressure decreases slightly (~ 0.1 MPa) but remains constant from 6 h to the end of the experiment (14 h). However, the high-smectite-content (80%Sm) sample exhibits a more gradual increase in pressure to the maximum value (3.7 MPa) after ~8 h, and this pressure is maintained until the end of the experiment (20 h). The difference between the total pressure and the fluid pressure (0.2 MPa) is regarded as the swelling pressure.

Table5.1. Result of swelling experiments

Test	Sample	Solution	Porosity (%)	Total pressure (MPa)	Fluid pressure (MPa)	Swelling pressure (MPa)
00	80%Sm	Brine water	55.1	0.628	0.01256	0.428
01	80%Sm	Brine water	47.6	1.272	0.02544	1.072
02	80%Sm	Brine water	43.4	2.784	0.05568	2.584
03	80%Sm	Brine water	41.1	3.726	0.07452	3.526
04	80%Sm	Brine water	39.4	3.852	0.07704	3.652
05	80%Sm	Brine water	39.2	4.646	0.09292	4.446
06	80%Sm	Brine water	36.9	6.5	0.13	6.3
07	60%Sm	Brine water	42.5	1.32	0.0264	1.12
08	60%Sm	Brine water	44.8	0.516	0.01032	0.316
09	60%Sm	Brine water	41.1	0.812	0.01624	0.612
10	60%Sm	Brine water	50.1	0.362	0.00724	0.162
11	60%Sm	Brine water	31	6.72	0.1344	6.52
12	60%Sm	Brine water	38.3	1.642	0.03284	1.442
13	60%Sm	Brine water	36.9	2.402	0.04804	2.202
14	60%Sm	Brine water	55.1	0.26	0.0052	0.06
15	40%Sm	Brine water	41	0.336	0.00672	0.136
16	40%Sm	Brine water	36.7	0.822	0.01644	0.622
17	40%Sm	Brine water	34.4	0.824	0.01648	0.624
18	40%Sm	Brine water	50.5	0.28	0.0056	0.08
19	40%Sm	Brine water	27.5	4.4	0.088	4.2
20	40%Sm	Brine water	29.9	1.84	0.0368	1.64
21	20%Sm	Brine water	58.5	0.224	0.00448	0.024
22	20%Sm	Brine water	41.1	0.406	0.00812	0.206
23	20%Sm	Brine water	32.8	0.454	0.00908	0.254
24	20%Sm	Brine water	27.5	1.158	0.02316	0.958
25	20%Sm	Brine water	25.1	2.16	0.0432	1.96
26	60%Sm	Pure water	37.7	3.216	0.06432	3.016
27	60%Sm	Pure water	42	2.212	0.04424	2.012
28	60%Sm	Pure water	44.4	1.42	0.0284	1.22
29	60%Sm	Pure water	48.1	0.818	0.01636	0.618
30	60%Sm	Pure water	55.8	0.538	0.01076	0.338
31	60%Sm	Pure water	32.2	8.996	0.17992	8.796

Figure 5.2 presents a summary plot of the maximum swelling pressures of the studied sample as a function of sample porosity. In a series of experiments with the same smectite content, the swelling pressure increases steadily with decreasing porosity. For example, the 80%Sm sample shows a swelling pressure of 0.5 MPa at a porosity of

55%, whereas it reaches as high as ~6 MPa at a porosity of 37%. For a given porosity, the swelling pressure increases with increasing smectite content. The sample with the lowest smectite content (i.e., 20 wt.%) shows a swelling pressure of only ~2 MPa, even at a porosity of 25%.

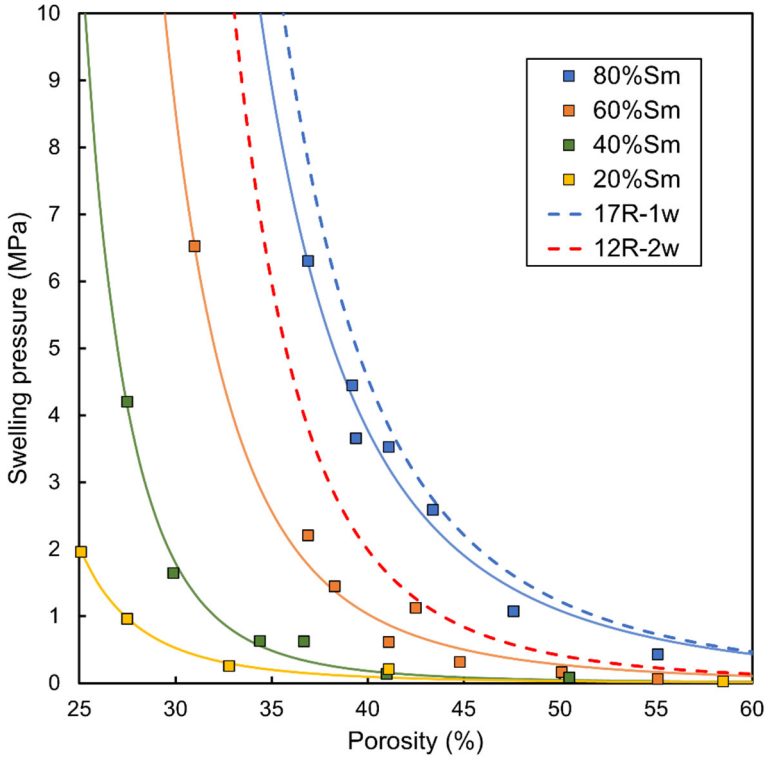

Figure 5.2. Results of swelling-pressure experiments on smectite–quartz composite samples in saline water. Results are shown for swelling-pressure experiments using 80%Sm, 60%Sm, 40%Sm, and 20%Sm as a function of sample porosity. The data were fitted using the empirical equation of Hedin (2004) (solid lines). Also shown are regression curves for Japan Trench core samples (17R-1w).

According to Hedin (2004), the relationship between the swelling pressure P_s (MPa) and water-saturated clay density ρ_c can be expressed empirically as

$$P_s = A \times T \left\{ \exp\left\{ B \frac{\rho_s(\rho_c - \rho_f)}{\rho_f(\rho_s - \rho_c)} \right\} - 1 \right\} \times \frac{1}{1000}, \quad (3)$$

where A and B are fitting parameters; T is temperature (K); and ρ_f and ρ_s are the densities of water (1.0 g/cm^3) and solid particles, respectively. ρ_c is related to ρ_s through the sample porosity ϕ as

$$\rho_c = \rho_s + \phi(\rho_f - \rho_s)\,. \quad (4)$$

Figure 5.2 also shows the results of least-squares fitting of the experimental data using Eqs. (3) and (4). The fitting parameters for the saline water experiment for samples 80%Sm, 60%Sm, 40%Sm, and 20%Sm were $A = 3.80 \times 10^{-1}$, 8.17×10^{-2}, 9.84×10^{-3}, and 7.34×10^{-5} and B = 0.85, 0.93, 1.03, and 1.47, respectively. The fitting parameters for 60%Sm in the pure water experiment were A = 0.27 and B = 0.81. Each series of data can be satisfactorily fitted by this model ($R^2 > 0.90$). Regression curves for the core samples from the Japan Trench (17R-1w and 12R-2w) from Kameda et al. (2019) are also plotted in Figure 5. 2. The smectite contents are 73% for sample 17R-1w and 10% for sample 12R-2w. Compared with the results of the present study, data for sample 17R-1w (corresponding to the plate-boundary fault) generally show the same or slightly higher swelling pressure, whereas data for sample 12R-2w, which has a low smectite content, show high swelling pressure.

Figure 5.3 shows the results of swelling experiments for 60%Sm in both pure water and saline water. Overall, a higher swelling pressure is observed for the pure water than the saline water. Komine et al. (2009) studied the swelling behavior of several smectite and bentonite samples, and observed higher swelling pressures in distilled rather than saline water for Na-type smectite but lower swelling pressures in saline rather than distilled water for Ca-type bentonite. The experimental results in this study are consistent with these previous results, as Na-type smectite was used in the present study.

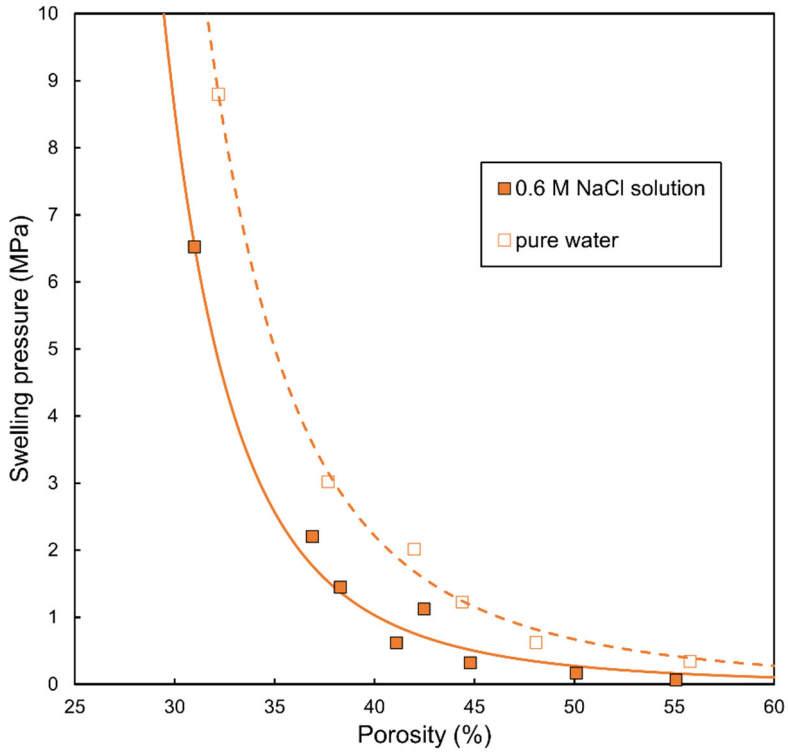

Figure 5.3. Comparison of swelling pressures in pure water and saline water with respect to porosity. Overall, a higher swelling pressure is observed for pure water than saline water. All data were obtained from experiments using 60%Sm.

5.4. Discussion

In general, from a microphysical viewpoint, the generation of swelling pressure in smectite under restricted volumetric expansion can be explained by diffuse double-layer repulsive forces acting between two charged plates. Using this framework, the swelling pressure can be estimated by applying the Gouy–Chapman theory. However, when non-swelling materials such as sand grains are present, such as in the present study (quartz), the swelling deformation of each smectite grain is also limited by the presence of the sand grains. To incorporate this effect into the estimation of the swelling pressure of a smectite–sand mixture, Komine and Ogata (2004) proposed a parameter referred to as the "swelling volumetric strain of the expandable phase" or ε_{sv}^{*}. Here, we combine the approach of Komine and Ogata (2004) and Gouy–Chapman diffuse double-layer theory to further investigate the experimental results. The detailed procedure for this investigation of swelling pressure is described in the Appendix.

Figure 5.4a shows the calculated swelling-pressure curves for saline water and experimental results obtained for pure water. Curves were calculated for NaCl concentrations of 30, 50, and 100 mM, which represent pressures close to those obtained experimentally. The results presented in Figure 5.4a show that even in the experiment using pure water, some ions were released into the pore water of the sample, possibly by the dissolution of soluble impurities in the powdered sample and ion exchange effects. Komine and Ogata (2004) also observed that similar concentrations of ions (20–50 mM) were released during swelling experiments of bentonite using pure water. Swelling pressures measured for saline conditions are markedly higher than theoretically predicted (Fig. 5.4b). Previous studies have not explained experimental data for high-salinity solutions such as seawater using diffuse double-layer theory. The present results also indicate that simple application of the theory to swelling pressure for saline conditions is challenging and that further study is needed.

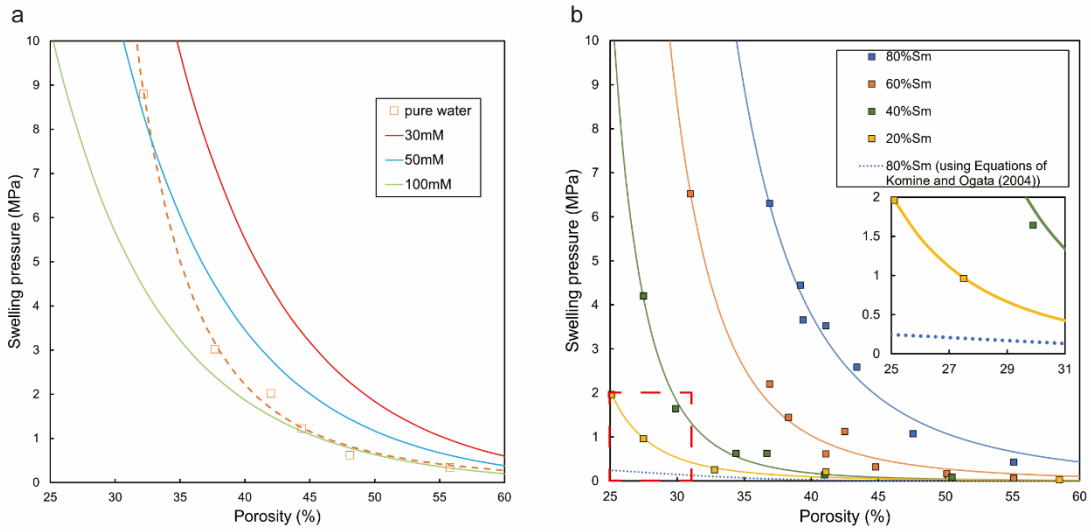

Figure 5.4. Comparison of experimental data with theoretical estimations based on the Gouy–Chapman theory (Komine and Ogata, 2004). (a) Results of an experiment using pure water (orange squares), with the fitting curve calculated using the empirical equation of Hedin (2004) (dashed line). Red, blue, and green lines are the results of calculations using the equation of Komine and Ogata (2004) and assuming NaCl concentrations of 30, 50, and 100 mM, respectively. (b) Application of the equations of Komine and Ogata (2004) to 80%Sm under a high NaCl concentration (0.6 M) (dotted blue line). The other data are the same as in

Figure 5.2. The inset shows an enlargement of the area enclosed by the dashed red line.

The experiments reported here were conducted with simplified solution and mineral compositions, meaning that caution should be taken when applying the obtained results to natural fault zones. For example, the swelling pressure of the low-smectite-content sample from the Japan Trench (12R-2w; Fig. 5.2) may be greatly underestimated if only the smectite content is considered, as interactions other than diffuse double-layer repulsion acting on the smectite particles may contribute to the generation of swelling pressure. In contrast, the estimated swelling pressure for the high-smectite-content sample (17R-1w) is similar to that of the natural sample. Therefore, the swelling pressure corresponding to smectite content seems to represent a lower limit.

Recent drilling surveys have revealed that a plate-boundary fault in the Sumatra subduction zone may be developed in clay-rich pelagic strata (McNeill et al., 2017), similar to the case of the Japan Trench. At the Sumatra drilling site, pelagic strata enriched in clay occur at depths of 1300–1400 m below the seafloor with an average total porosity of ~30% (Unit III; Dutilleul et al., 2020). The Na concentration of pore water in this unit is 500 mM (McNeill et al., 2017). Results of quantitative XRD suggest that the total smectite content is as high as 60–70 wt.% in the lower section of this unit (McNeill et al., 2017; Rosenberger et al., 2020). On the basis of the average grain density and the porosity profile of the sediments above this depth (McNeill et al., 2017), the overburden pressure at the stratigraphic level of Unit III is estimated to be ~17–18 MPa. For example, if the 60%Sm curve is extrapolated to the 30% porosity condition (Fig. 5.2), a swelling pressure of ~10 MPa can be expected to be generated. As mentioned earlier, given that this value is the lower limit, a swelling pressure comparable to the overburden pressure (i.e., ~17–18 MPa) is expected if the smectite content is ≥60 wt.% under the relevant porosity conditions. This result suggests that the shear strength of this horizon is very low and is also consistent with the inference that a plate-boundary fault (i.e., a décollement) can develop at this stratigraphic level. As this sedimentary section approaches the trench axis with continuing plate movement, the effective overburden stress will increase because of the supply of terrigenous sediments (Hüpers et al., 2017), and the degree of compaction will also increase. In this case, the swelling pressure may exceed the overburden pressure, and volumetric expansion (i.e., increase in porosity) is expected to occur to balance the overburden pressure. In any case, the plate-boundary fault at Sumatra may be in a state of low effective stress similar to that of the Japan Trench. This inference could be verified using drillhole data.

5.5. Conclusion

To clarify the effect of swelling pressure on the behavior of smectite-rich fault zones, I conducted swelling-pressure experiments using composite smectite–quartz powder in pure water and saline water. For the experiments, smectite content was varied over a wide range to allow application to natural fault zones. The main conclusions of the study are as follows.

(1) Swelling pressure increases with decreasing porosity. For a given porosity, swelling pressure increases with increasing smectite content. Under the same porosity and smectite content conditions, swelling pressure is greater in pure water than in saline water. It is also confirmed that predictions based on the Gouy–Chapman theory provide a marked underestimation of the swelling pressure generated under conditions of high salinity.

(2) The swelling pressure generated in a natural sample (from the Japan Trench) with a high smectite content was closely reproduced by the experiment with an equivalent smectite content and under corresponding porosity conditions. In contrast, the swelling pressure of a natural sample with low smectite content was greatly underestimated, suggesting the possibility that the swelling of natural samples is controlled by other materials in addition to smectite.

(3) The swelling behavior of a pelagic clay layer (smectite content of >60%) in sediments off Sumatra was examined by applying the experimental results in combination with constraints on material properties and conditions obtained from drilling. The results indicate that swelling pressure comparable to the overburden pressure may be generated in these sediments. The swelling behavior may affect the initial development of a fault and subsequent fault-slip behavior at this plate convergent margin.

Chapter 6 Nanopore structures of a fossil out-off sequence thrust and its implications for faulting processes

6.1. Introduction

The pore structure of a rock is an important factor controlling its mechanical properties and fluid or gas transport properties. In recent years, the growing demand for shale gas and the focus on tight oil, a new type of resource, have led to the analysis of the pore structure of various sedimentary rocks, including sandstone, carbonate rock, and shale (Kuila and Prasad, 2013; Li et al., 2019; Qin et al., 2021; Kong et al., 2021). Among these sedimentary rocks, shale is characterized by a particularly complex pore structure because it contains many fine crystals, such as clay minerals. Gas adsorption/desorption measurements are an effective means of analyzing such a complex structure of small-scale pores (generally >100nm) and have been applied to shales from a variety of sources (Wang et al., 2015; Chen et al., 2017; Li et al., 2017). These studies have shown that pore structure of shale depends on several factors, e.g., organic matter content and mineral composition.

In this study, I focus on the nanopore structure of shale that constitutes fault zone in plate subduction zone. Here, I will generally refer to pores of 100 nm or less obtained by gas adsorption/desorption experiments as “nanopores”, that is, including micropores (>2 nm pore size) and mesopores (2-50 nm pore size) according to the classification of the International Union of Pure and Applied Chemistry (IUPAC). These pores are thought to play an important role in the faulting process because they regulate the circulation of fluids and gases in the vicinity of the fault. Fluid in a fault acts on its mechanical aspects as fluid pressure (Sibson, 1973). In addition, fluid has the ability to modify the constituent materials by causing fluid-rock interactions in fault zones (references). It has also been pointed out that the chemical condition of fault zone may change over time due to the generation of hydrogen gas associated with mechanochemical reaction during earthquakes (Kameda et al., 2003; Saruwatari et al., 2004; Yamaguchi et al., 2011). On the other hand, the nanoscale pore structure depends on the type and fabric of fine phyllosilicate minerals, one of the major components of faults, and is expected to provide important information for understanding the formation and development process of faults.In chapter 3, I applied the gas adsorption/desorption method to a fault zone formed in a shallow part of subduction zone (~1000 m depth; the Shirako Fault, central Japan) and found that nanopores were formed in the fault gouge,

which were most likely caused by selective fracturing of clay minerals. However, chapter 3 focused on a fault zone in sediments with high porosity (~30%) with little burial diagenesis, and this chapter is the first attempt to apply this approach to deeper shale-dominated fault zones.

I here analyzed rocks comprising the Nobeoka Fault, which is exposed within an ancient accretionary complex (Shimanto Belt) in Kyushu, Japan. This fault is a large thrust fault with a total displacement of several kilometers and is considered to be equivalent to the megasplay fault that branches off the plate boundary in the modern Nankai Trough (Kondo et al., 2005). The sedimentary rocks in the hanging wall and footwall of the fault have suffered burial diagenesis of ~250 to 350 °C, and the muddy layer have become typical shale (Kondo et al., 2005). However, due to shear deformation near the plate boundary, it exhibits a mélange texture consisting of a so-called block-in-matrix structure (Kimura et al., 2013), and shale is observed in the matrix surrounding the deformed sandstone fragments (Kondo et al., 2005; Kimura et al., 2013). Furthermore, these mélange-forming deformations were overprinted by cataclastic deformation associated with subsequent faulting of the Nobeoka Fault. In 2011, a drilling survey was conducted on the Nobeoka Fault and core samples with a total length of 255 m were recovered (Hamahashi et al., 2013; 2015). These samples show little weathering at the surface, and are therefore suitable for a range of material analyses. In this study, a total of 30 samples were collected from various depths including principal slip zone (PSZ) of the Nobeoka Fault and the pore structure was evaluated by the gas adsorption/desorption method. At the same time, mineral analysis and measurement of organic matter content were also conducted to examine the factors that may affect the pore structure. Based on these results, the deformation process of the Nobeoka Fault is discussed.

6.2. Geological Setting of the Nobeoka Thrust

The Shimanto Belt is an ancient accretionary complex that is widely exposed along the Pacific side of southwest Japan (Fig. 6.1a). The belt is divided into northern and southern sub-belts, separated by the Aki Tectonic Line in the Shikoku and Kii regions, and by the Nobeoka Thrust in Kyushu (Taira, 1988). In eastern Kyushu, the Kitagawa Group was exhumed north of the Nobeoka Thrust, emplaced over the southern Hyuga Group (Fig. 6.1b). The Kitagawa Group is composed of phyllitic shales and sandstones, with pronounced formation of the slaty cleavages closer to the Nobeoka Thrust. Vitrinite reflectance values of the unit range from 5.33 to 5.63 (Kondo et al., 2005),

corresponding to maximum paleotemperatures of 320-330 °C. These temperatures are similar to the formation temperature of metamorphic chlorite (Raimbourg et al., 2009) and those estimated from illite crystallinity (Kameda et al., 2011; Fukuchi et al., 2014).

The Hyuga Group, footwall of the Nobeoka Thrust, is composed of mélange of shale matrix with sandstone and basaltic blocks deformed in a brittle manner. Vitrinite reflectance data indicate temperatures of 250-270 °C, which are 50-80 °C lower than those obtained for the hanging wall rock. From this temperature difference, cumulative displacement along the Nobeoka Thrust is estimated to be up to 7–10 km (Kondo et al., 2005), responsible for exhuming the sedimentary rocks from deep within the accretionary complex (Raimbourg et al., 2009). It has also been suggested that the Nobeoka Thrust is a fossilized splay fault branching off an ancient decollement analogous to those observed in the modern Nankai Trough (Kondo et al., 2005).

In 2011, a drilling survey was conducted through the fault, and core samples were collected for a total length of 255 m, including PSZ at a depth from 41.3-41.8 m (Hamahashi et al., 2013). The PSZ is a random to weakly foliated cataclasite with a marked size reduction of sandstone fragments relative to the surrounding rocks. Pseudotachylyte of 1 to 2 mm thick has been also observed to form on the top of the PSZ (at ~41.35 m depth; Hasegawa et al., 2019). In addition to the PSZ, multiple consolidated or unconsolidated shear zones were observed throughout the core (Hamahashi et al., 2013; 2015).

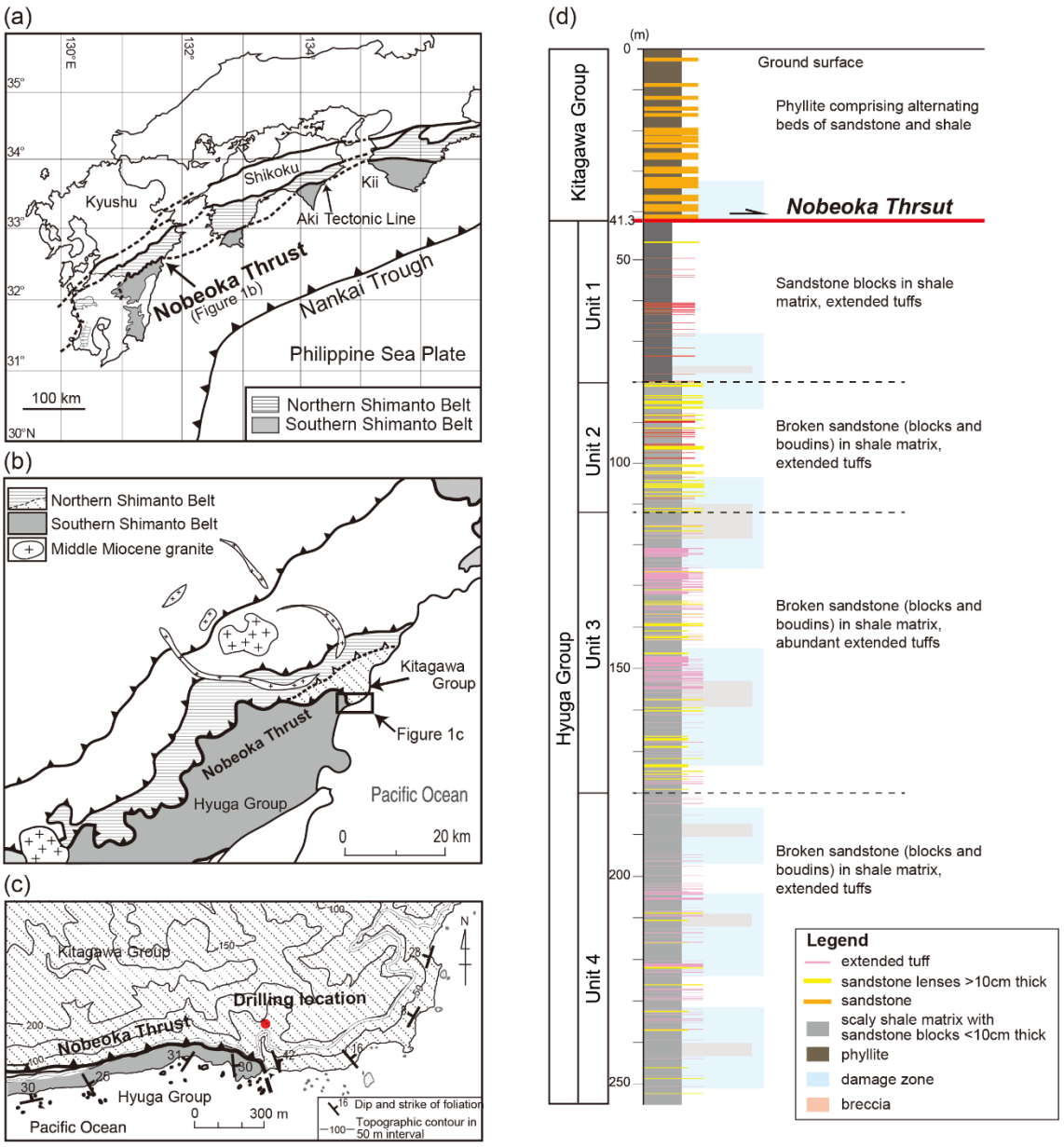

Figure 6.1. (a) Geologic setting of the Nobeoka Thrust and distribution of the Shimanto Belt in southwest Japan. (b) A simplified geologic map of the Shimanto Belt in northeast Kyushu, modified from Murata (1998). (c) Geologic map showing the studied area and the locality of the drilling location (dot) of the Nobeoka Thrust (modified from Kondo et al., 2005 and Kimura et al., 2013). (d) Lithology of the borehole core (modified from Fukuchi et al., 2014).

6.3. Samples and experiments.

In this study, a total of 30 samples were analyzed: 8 samples from the Kitagawa Group (hanging wall), 20 samples from the Hyuga Group (Footwall), and 2 samples from the PSZ. Two of the hanging wall samples were taken from just above the PSZ, which correspond to an interval within the damage zone (Hamahashi et al., 2013), and are therefore presented below separately from the other hanging wall samples. On the other hand, since the majority of the samples in the footwall side belong to one of several damage zones, they are shown without distinction.

Gas adsorption/desorption measurements were performed on the bulk samples which were gently ground and passed through a <425 μm sieve. Before the measurements, the samples were degassed at 200°C for 12 hours to remove water and gas molecules adsorbed on the surface. The measurements were performed by using a gas adsorption analyzer (BELSORP MINI X, MicrotracBEL Corp.) under liquid nitrogen temperature (77K) conditions. The obtained adsorption-desorption isotherms were provided for pore size distribution (PSD) analysis based on the Barrett–Joyner–Halenda (BJH) method (Barrett et al. 1951). The specific surface area of the samples was also determined from the adsorption isotherms using BET (Brunauer, Emmett, and Teller) theory.

For each sample, total organic carbon (TOC) content was also measured using a CHN coder (MT-5, Yanako) in the laboratory of A Rabbit Science Corp. As a pretreatment, samples were soaked in 1*N* hydrochloric acid to decompose inorganic carbon (carbonate minerals).

In addition, X-ray diffraction measurement and pattern analysis using RockJock software (Eberl, 2003) were performed to quantitatively evaluate their mineral composition. The measurement and analysis procedures followed Tanikawa and Tadai (2018).

6.4. Results

Figure 6.2 and Table 6.1 shows the pore structure parameters obtained from gas adsorption measurements. Figure 6.3 plots each parameter against the depth of the drilling hole.

The specific surface area ranges from ~1 to 4 m^2/g for the hanging wall and from ~2 to 7 m^2/g for the footwall, with the later generally showing larger values. In the footwall, the values are variable and no clear correlation is observed with the damage zone. The

PSZ values do not differ significantly from those of the footwall, but two samples in the damage zone of the hanging wall show distinctly smaller values than the other samples. The total pore volume ranges from ~0.01 to 0.02 cm^3/g for the hanging wall and from ~0.01 to 0.03 m^2/g for the footwall, and no clear difference is seen between the two. PSZ and the hanging wall samples in the damage zone show slightly smaller values. The micropore volume fraction is defined here as micropore volume / (micropore volume + mesopore volume). This value is generally in the range of 0.1 to 0.2 for both the hanging wall and footwall. Samples in the hanging wall damage zone show slightly lower values than the other samples. PSZ, on the other hand, shows distinctly higher values (>0.2). The fractal dimension ranges from ~2.5 to 2.65 for the hanging wall and from ~2.65 to 2.7 for the footwall, with the later generally showing larger values. The PSZ values are within the range of those of the footwall, but show slightly higher values. The damage zone samples in the hanging wall, on the other hand, show smaller values than the other hanging wall samples.

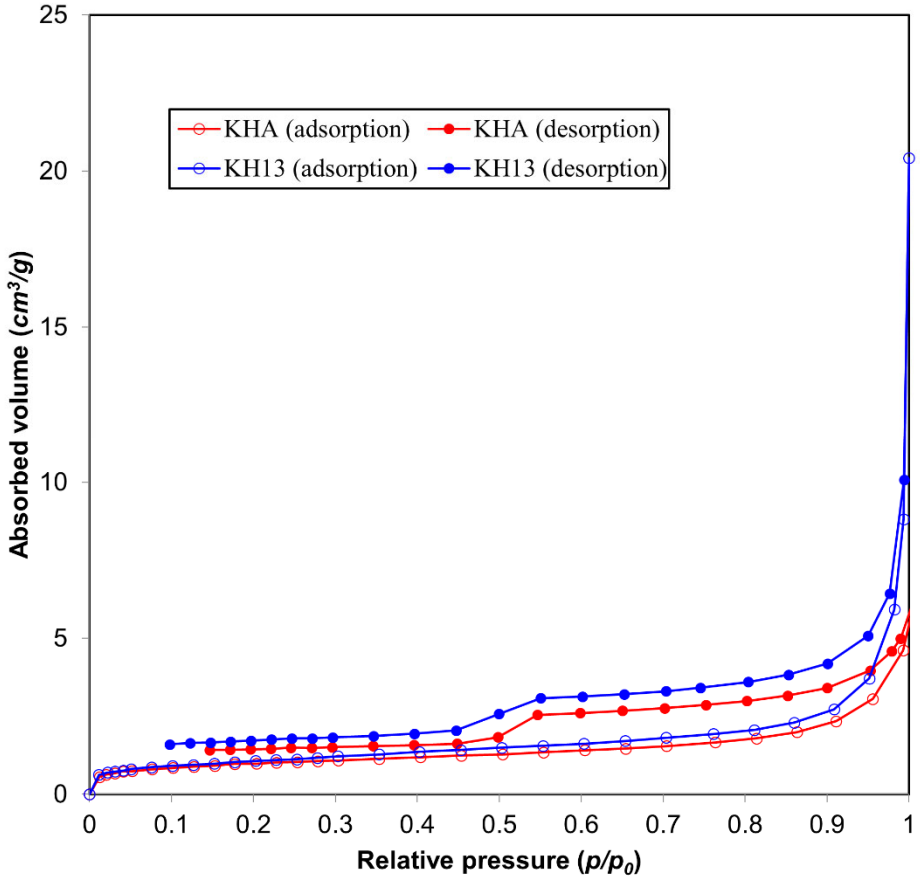

Figure 6.2. Typical isotherms of the footwall (KH13) and the PSZ (KHA).

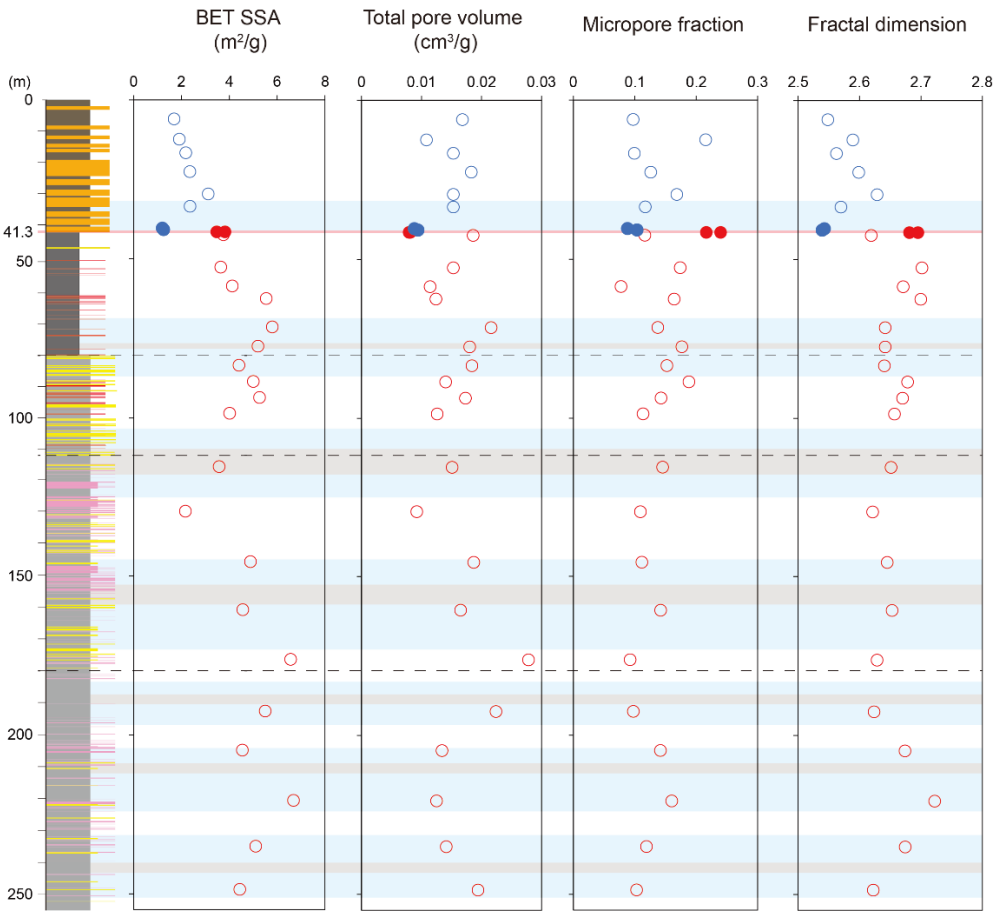

Figure 6.3. BET specific surface area (SSA), total pore volume, micropore fraction, and fractal dimension against depth (mbgs).

Table 6.1. Pore structure parameters obtained from gas adsorption/desorption measurements

Sample		Depth (mbgs)	BET specific surface area(m^2/g)	Total pore volume (cm^3/g)	Micropore volume (cm^3/g)	Mesopore volume (cm^3/g)	Micropore fraction	Fractal dimension
KH01	Hanging wall	2.74	5.05	0.0182	0.00159	0.00686	0.19	2.67
KH02	Hanging wall	6.04	1.69	0.0168	0.00030	0.00274	0.10	2.55
KH03	Hanging wall	12.4	1.91	0.0108	0.00082	0.00297	0.22	2.59
KH04	Hanging wall	16.65	2.18	0.0153	0.00037	0.00340	0.10	2.56
KH05	Hanging wall	22.57	2.35	0.0183	0.00044	0.00306	0.13	2.60
KH06	Hanging wall	29.58	3.12	0.0153	0.00072	0.00354	0.17	2.63
KH07	Hanging wall	33.49	2.36	0.0153	0.00046	0.00350	0.12	2.57
KH08	Hanging wall (damege zone)	40.34	1.2	0.0088	0.00023	0.00237	0.09	2.54
KH09	Hanging wall (damege zone)	40.79	1.25	0.0094	0.00038	0.00326	0.10	2.54
KHA	Fault core	41.5	3.47	0.0081	0.00122	0.00385	0.24	2.68
KHB	Fault core	41.5	3.82	0.0079	0.00111	0.00401	0.22	2.70
KH13	Footwall	42.43	3.75	0.0186	0.00069	0.00522	0.12	2.62
KH14	Footwall	52.63	3.64	0.0153	0.00117	0.00554	0.17	2.70
KH15	Footwall	58.56	4.12	0.0114	0.00039	0.00470	0.08	2.67
KH16	Footwall	62.47	5.54	0.0124	0.00107	0.00546	0.16	2.70
KH17	Footwall	71.43	5.79	0.0216	0.00109	0.00683	0.14	2.64
KH18	Footwall	77.47	5.19	0.018	0.00112	0.00523	0.18	2.64
KH19	Footwall	83.43	4.4	0.0184	0.00097	0.00542	0.15	2.64
KH20	Footwall	88.53	5	0.014	0.00119	0.00513	0.19	2.68
KH21	Footwall	93.59	5.26	0.0173	0.00092	0.00553	0.14	2.67
KH22	Footwall	98.59	4.01	0.0126	0.00061	0.00475	0.11	2.66
KH23	Footwall	115.65	3.57	0.0151	0.00071	0.00419	0.15	2.65
KH24	Footwall	129.65	2.16	0.0092	0.00037	0.00299	0.11	2.62
KH25	Footwall	145.54	4.88	0.0187	0.00077	0.00613	0.11	2.65
KH26	Footwall	160.63	4.56	0.0165	0.00090	0.00544	0.14	2.65
KH27	Footwall	176.24	6.56	0.0278	0.00088	0.00866	0.09	2.63
KH28	Footwall	192.49	5.5	0.0224	0.00080	0.00741	0.10	2.62
KH29	Footwall	204.79	4.54	0.0134	0.00088	0.00535	0.14	2.67
KH30	Footwall	220.61	6.68	0.0125	0.00109	0.00574	0.16	2.72
KH31	Footwall	235	5.1	0.0141	0.00082	0.00611	0.12	2.67
KH32	Footwall	248.61	4.43	0.0194	0.00069	0.00600	0.10	2.62

Figure 6.4 shows the correlation between the nanopore structural parameters (fractal dimension, total pore volume, micropore volume and mesopore volume) and specific surface area. There is a generally positive correlation between them, which is consistent with the results of previous studies (Liu et al., 2015; Li et al., 2019). In particular, the good correlation between the specific surface area and mesopore volume is a major feature of these samples.

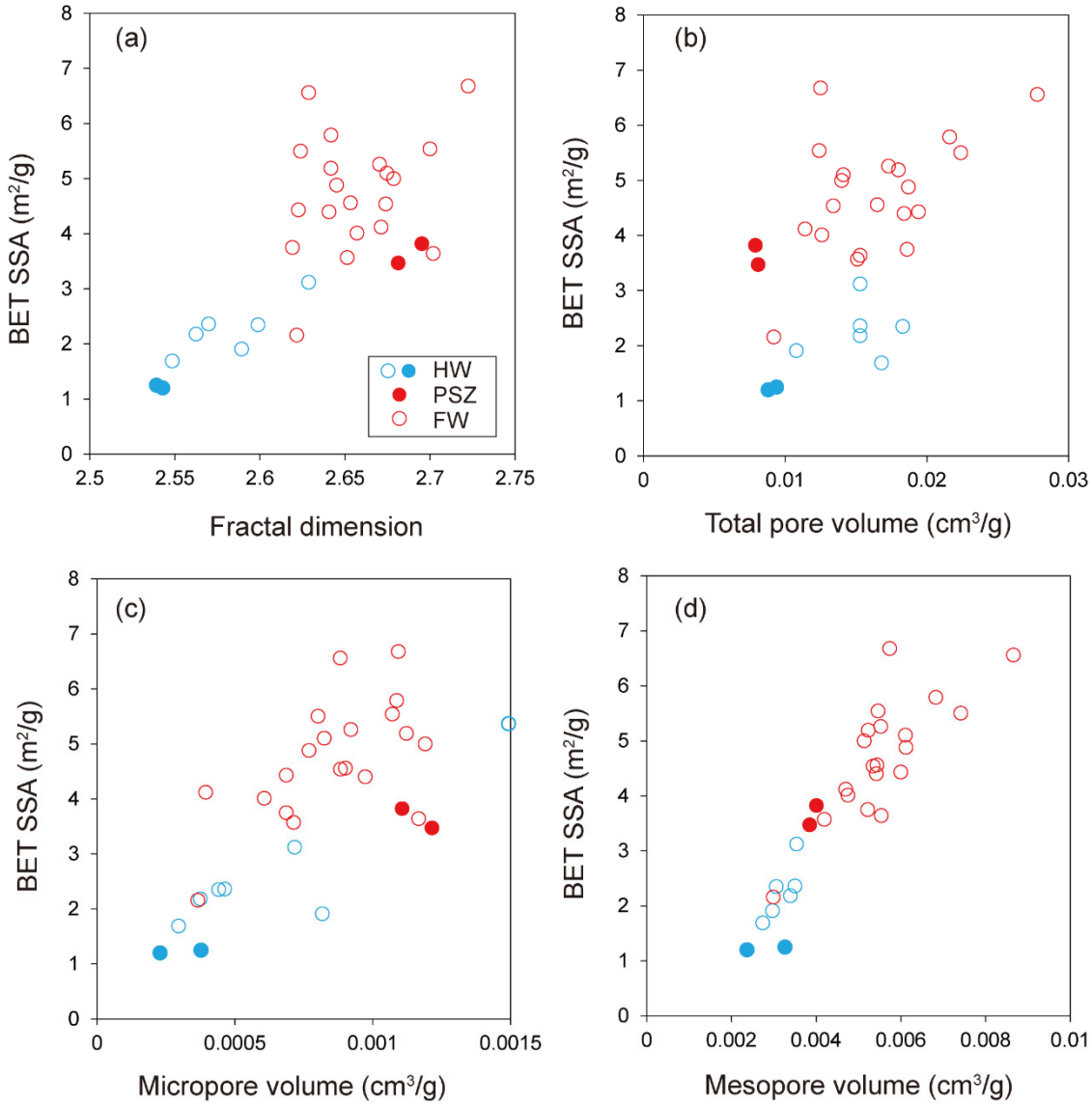

Figure 6.4. Relation between BET specific surface area and each pore structure parameter. (a) Fractal dimension. (b) Total pore volume. (c) Micropore volume. (d) Mesopore volume.

Semi-quantitative mineral analysis of the core samples has been carried out by

Fukuchi et al. (2014) using XRD. In the present study, quantitative analysis using Rockjock was performed on these samples (Fig 6.5, Table 6.2). The results are plotted against the core depth in Fig. 6.6. The analyzed samples consist of quartz, feldspar, carbonates (calcite + dolomite + siderite) and clay minerals (kaolin, illite, chlorite and muscovite). Quartz content ranges from ~5 to ~30% throughout the cores and vary widely with depth. Carbonate minerals appear to be inversely correlated with quartz content and generally range from 5-10%, although a value exceeding 20% was also observed. Feldspar fluctuates between approximately 10-20%. The muscovite content shows a marked difference between the hanging wall and footwall, with the former generally showing higher values (25%-40%) than the footwall (15-20%). Illite shows the opposite trend to muscovite, with values as low as ~10-15% in the hanging wall, whereas in the footwall they are in the range of ~15-20%. The values for chlorite and kaolin appear to be stable at around 10% and 5%, respectively. The reversal of muscovite and illite content between the hanging wall and footwall may reflect differences in the grade of the respective diagenetic to weak metamorphic processes. On the hanging wall side, a distinct growth of muscovite crystals has been reported with the development of slaty cleavages (Kameda et al., 2011). The illite crystallinity (the width at half maximum (FWHM) of the illite peak; the smaller the FWHM, the closer the structure is to muscovite) shows different values for hanging wall and footwall (Fukuchi et al, 2014), which is also consistent with the results obtained in this study.

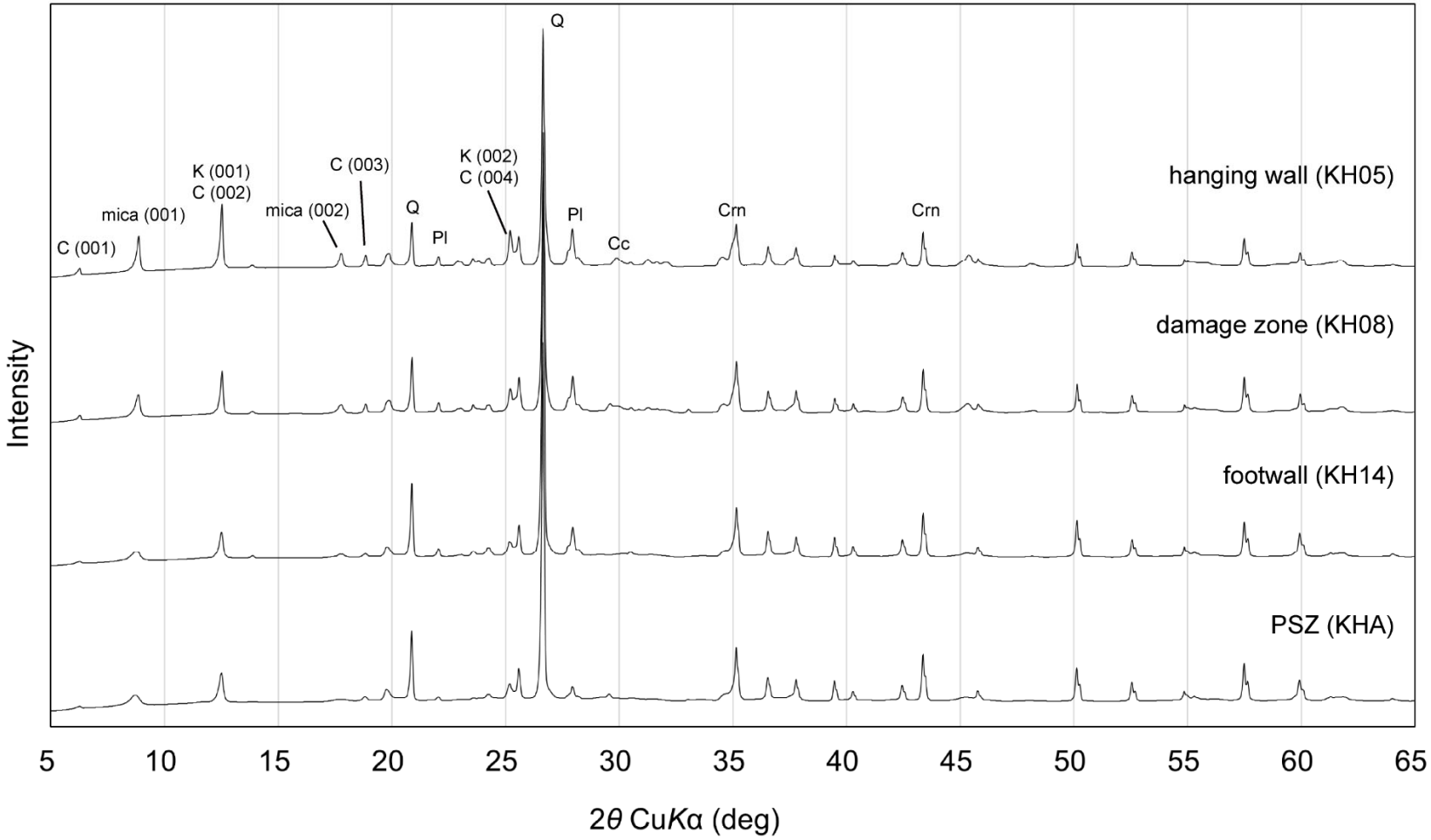

Figure 6.5 Typical XRD patterns of the hanging wall, the damage zone, the footwall, and the PSZ samples. C, chlorite; mica, illite and muscovite; K, kaolinite; Q, quartz; Pl, Plagioclase; Cc, calcite; Crn, corundom.

Table 6.2. Results of mineral composition analysis by XRD.

Sample		Quartz	Kspar	Plagioclase	Calcite	Calcite (Mg-rich)	Dolomite	Halite	Total clays	Kaolinite	Illite	Chlorite	Muscovite
KH01	Hanging wall	17.3	1.5	20.8	2.6	1.8	2.6	0.2	41.4	3.9	6.5	6.8	24.3
KH02	Hanging wall	14.8	2.6	15.0	2.8	0.9	2.4	0.5	50.8	3.0	7.0	8.9	31.9
KH03	Hanging wall	15.1	2.4	13.9	2.3	1.1	2.4	0.3	52.7	3.8	6.7	10.2	32.0
KH04	Hanging wall	15.8	3.9	12.9	2.7	0.4	5.4	0.7	48.3	2.8	3.4	5.7	36.3
KH05	Hanging wall	12.7	1.3	8.2	2.3	0.8	3.2	0.6	62.9	4.1	8.5	11.0	39.3
KH06	Hanging wall	12.8	1.8	12.8	2.3	1.1	2.7	0.3	56.8	3.5	7.4	9.6	36.5
KH07	Hanging wall	21.6	1.3	15.0	3.3	0.9	2.5	0.4	45.4	3.0	3.2	8.8	30.4
KH08	Hanging wall (damege zone)	15.3	3.1	9.0	3.8	1.1	3.1	0.4	53.7	2.7	9.2	8.7	33.2
KH09	Hanging wall (damege zone)	5.6	3.0	7.9	3.7	1.7	3.8	0.3	66.2	3.7	14.6	10.7	37.2
KHA	Fault core	14.0	2.8	11.5	4.2	2.5	3.9	0.1	50.6	3.6	20.1	7.1	19.8
KHB	Fault core	22.2	2.9	9.1	1.3	1.8	3.3	0.2	47.2	2.1	21.3	7.4	16.4
KH13	Footwall	12.5	3.4	11.1	3.6	2.9	3.5	0.1	52.7	3.8	19.1	8.7	21.1
KH14	Footwall	11.9	4.7	9.7	2.8	2.4	3.3	0.1	55.1	2.8	20.7	9.8	21.8
KH15	Footwall	5.7	4.4	11.4	2.9	3.0	4.5	0.1	58.8	3.8	21.6	10.1	23.3
KH16	Footwall	10.2	3.8	11.2	2.7	2.6	3.7	0.1	55.8	3.2	20.7	8.5	23.3
KH17	Footwall	24.6	2.0	8.1	2.3	2.6	4.0	0.1	45.4	3.2	16.8	7.3	18.1
KH18	Footwall	9.2	3.2	10.8	2.8	2.8	3.5	0.2	57.9	2.9	23.7	9.0	22.4
KH19	Footwall	17.9	3.5	9.0	2.3	2.4	3.3	0.1	52.7	2.7	18.5	9.4	22.0
KH20	Footwall	24.3	3.3	11.3	1.2	2.2	2.8	0.1	42.7	2.6	15.0	7.0	18.0
KH21	Footwall	29.9	3.2	10.8	0.9	1.4	2.9	0.2	36.8	2.2	19.2	2.7	12.7
KH22	Footwall	4.9	1.2	10.6	11.7	3.7	5.5	0.0	55.6	6.4	21.1	9.9	18.1
KH23	Footwall	17.3	3.4	10.0	2.9	2.5	4.4	0.2	50.8	3.6	17.5	9.5	20.2
KH24	Footwall	14.7	5.4	8.0	2.1	3.0	6.9	0.1	49.0	2.7	19.5	5.9	20.8
KH25	Footwall	16.7	3.7	13.4	2.1	2.2	3.3	0.1	47.8	3.2	16.0	7.4	21.3
KH26	Footwall	12.2	3.0	15.3	3.0	3.0	3.3	0.1	52.3	4.3	15.0	10.5	22.6
KH27	Footwall	13.9	3.4	12.2	2.8	2.7	3.6	0.1	50.7	3.3	16.8	9.5	21.1
KH28	Footwall	10.4	4.8	8.4	3.1	2.5	3.6	0.2	56.7	3.2	20.8	8.3	24.3
KH29	Footwall	12.2	4.8	9.9	3.2	2.6	3.5	0.1	55.0	2.9	17.4	11.1	23.6
KH30	Footwall	14.3	3.4	15.8	2.5	3.1	3.4	0.1	46.3	3.6	13.1	9.4	20.1
KH31	Footwall	20.0	4.0	4.7	2.7	2.2	3.5	0.2	50.7	2.9	25.8	7.6	14.3
KH32	Footwall	21.2	3.8	5.6	2.1	2.1	3.4	0.1	49.6	2.6	25.7	7.3	14.0

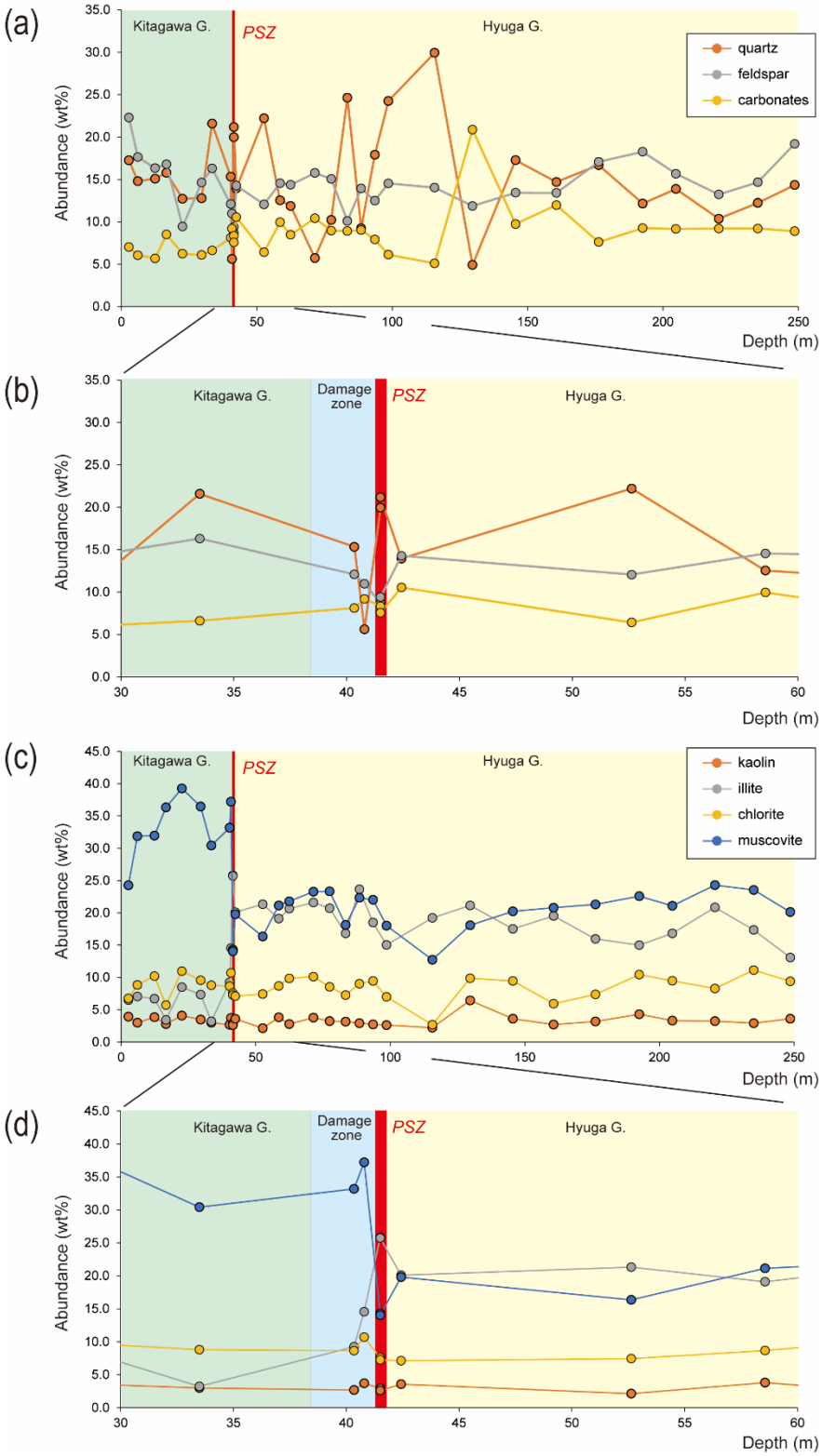

Figure 6.6 Variation in modal composition of quartz, feldspar, and carbonate (a and b) and clay minerals (c and d) with respect to the drilling depth.

6.5. Discussion

6.5.1. Factors affecting variations in pore structures of the Nobeoka Fault (1): Mineral composition and TOC

Because the Nobeoka Fault is a large-scale thrust fault that cuts the thermal structure within the accretionary complex, hanging wall and footwall shales that have undergone different grades of diagenesis to weak metamorphism are exposed in contact. Therefore, such differences were primary observed in the nanopore structures of the analyzed core samples (Fig. 6.7). On the other hand, the nanopore structures are also known to be strongly dependent on mineral composition (especially clay mineral content) and TOC (Li et al., 2019). Figure 6.7 shows the correlations between several parameters and the clay mineral content of the samples. As described above, XRD analysis shows that the samples contain kaolin, illite, chlorite and muscovite as layered silicate minerals, with total amounts of ~50-65% and ~35-60% in the hanging wall and footwall shales, respectively. It should be noted that the analyzed samples are likely to contain deformed sandstone fragments of various sizes, and the differences in clay content may reflect the mixing ratio of shale and sandstone. Correlations are presented here for the hanging wall and footwall, respectively, for the data sets excluding the PSZ and damage zone samples. Most parameters do not show a strong correlation with clay mineral content, but a slight positive correlation with fractal dimension was observed in the hanging wall samples (R^2=0.45). Higher clay content may contribute to more diverse and complex pores, which may lead to an increase in fractal dimension, as suggested by Li et al. (2019).

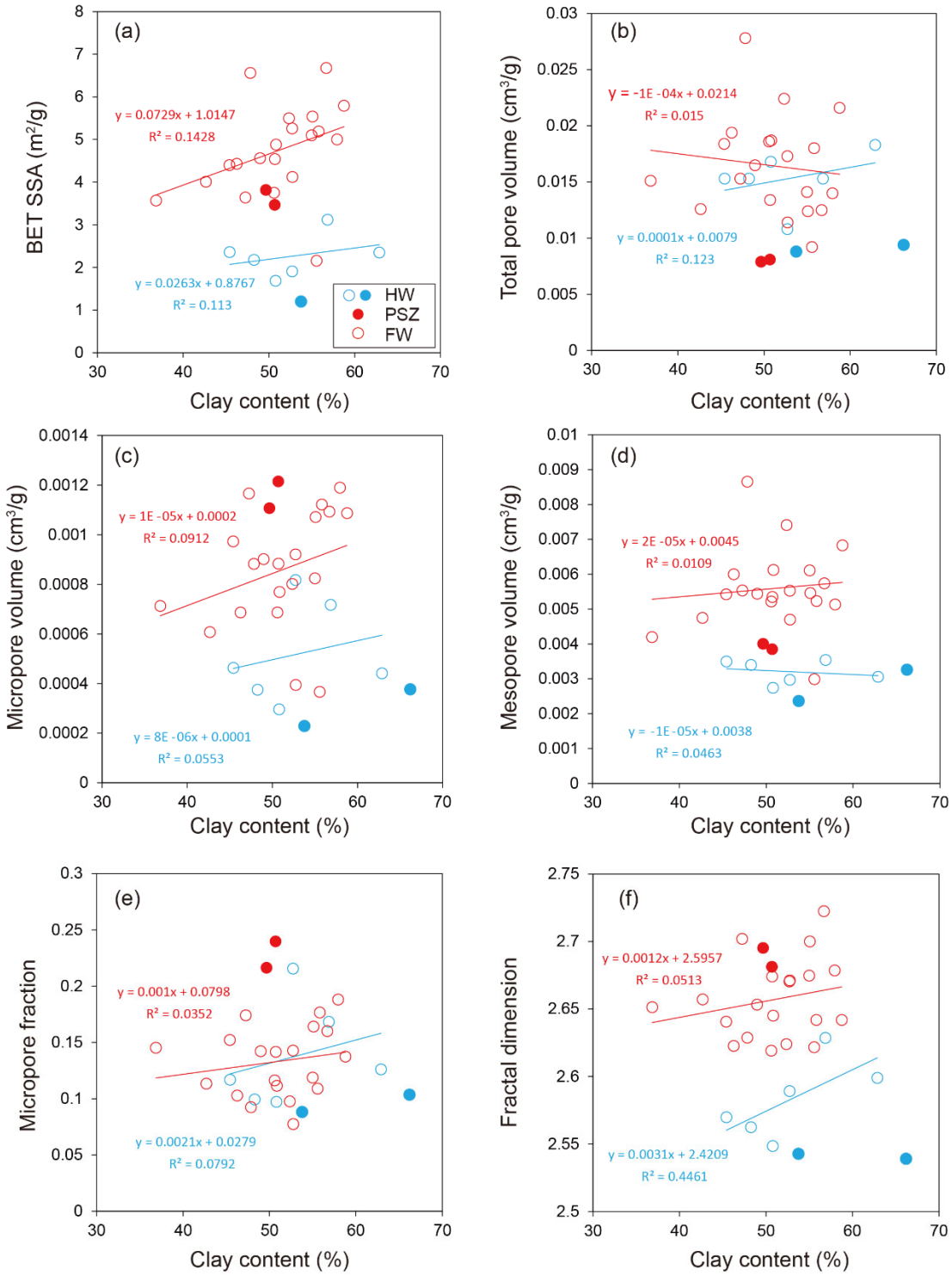

Figure 6.7 Correlation between clay content and pore structure parameters. (a) BET specific surface area. (b) Total pore volume. (c) Micropore volume. (d) Mesopore volume. (e) Micropore fraction. (f) Fractional dimension.

Figure 6.8 shows the correlation between the pore structural parameters and TOC. Both hanging wall and footwall samples contain small amounts of TOC, less than 0.6%. It is generally considered that an increase in TOC contributes to an increase in specific surface area and total pore volume (Li et al., 2019). In the present sample, a weak positive correlation between TOC and specific surface area and fractal dimension was observed in the hanging wall samples, while no clear correlation was observed in the footwall samples. One reason why some correlations were observed in the hanging wall samples is that, in general, intervals outside the damage zone are less intensely deformed than those of the footwall. In other words, cataclastic deformation of the Nobeoka Fault may also affect the nanopore structure. In the next section, the relevance of such fault activity to the pore structures is discussed, with particular focus on the PSZ and hanging wall damage zone.

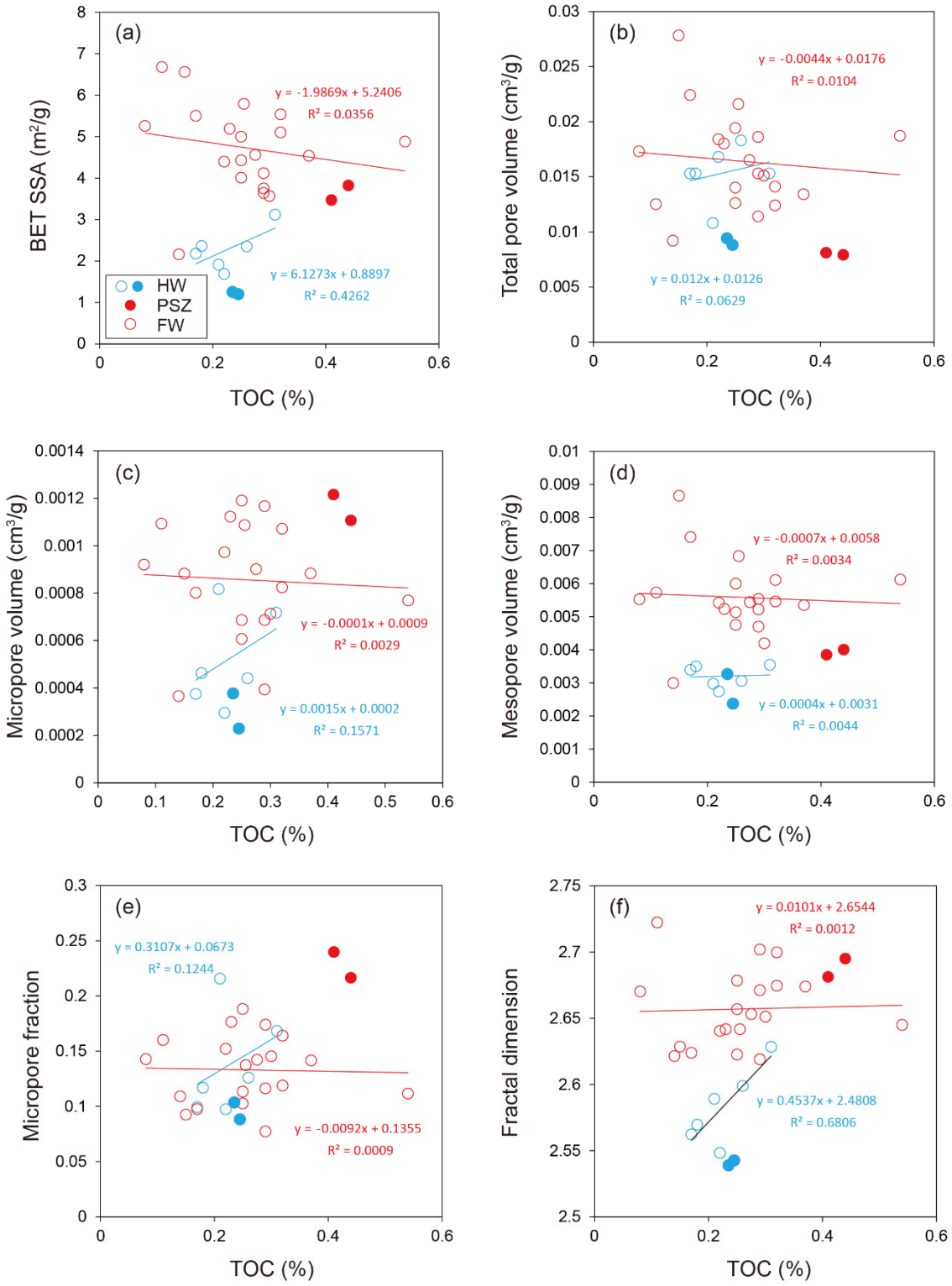

Figure 6.8. Correlation between TOC and pore structure parameters. (a) BET specific surface area. (b) Total pore volume. (c) Micropore volume. (d) Mesopore volume. (e) Micropore fraction. (f) Fractional dimension.

6.5.2. Factors affecting variations in pore structures of the Nobeoka Fault (2):

Influence of deformation processes

On the hanging wall side of the Nobeoka Fault, a 3 m thick damage zone was visually identified just above the PSZ (38.1-41.3 m) and is characterised by cataclastically fractured phyllite with many sandstone fragments (Hamahashi et al., 2013). Logging studies have also shown that this interval exhibits characteristic physical properties, such as low neutron porosity and resistivity and high elastic wave velocity (Hamahashi et al, 2013). The pore structure analysis of the samples in this interval also revealed low specific surface area, total volume, micropore volume fraction and fractal dimension (Figs. 6.3 and 4). A possible reason for the low neutron porosity and nanopore volume could be the high content of sandstone fragments in these samples, but this seems unlikely given that the clay content is similar or rather slightly higher than in the other samples. The decrease in the proportion of micropores in addition to the total nanopore volume indicates a selective reduction of micropore volumes. Icarried out pore structural analysis of the Shirako Fault in chapter 3, which was deformed in a shallow subduction zone, and found that micropores were formed during coseismic deformation of the fault by clay exfoliation and that such pores have been preserved up to the present day, when they have exhumed to the surface. In the Nobeoka Fault, cataclastic deformation has resulted in significant fragmentation of sandstone blocks, but in addition to this, it is also expected to cause deformation of clay minerals, which have a lower fracture strength in the shale matrix. In fact, Fukuchi et al. ((Moore & Saffer, 2001; Mukoyoshi et al., 2006; Satake, 1993; Trütner et al., 2015)14) observed a decrease in the illite crystallinity (i.e., increase in the FWHM of the illite peak) at this interval, which, together with the results of the ball-milling experiment, suggest that exfoliation and size reduction of illite crystals due to shear action. In the present XRD experiment, this can be observed as an increase in illite content at this interval (Fig. 6.6). However, unlike the Shirako Fault studied, the Nobeoka Fault was activated in much higher pressure and temperature conditions, resulting in pressure solution deformation driven by these thermal conditions (Kimura et al., 2013). Such solution-mediated deformation may have promoted mineral precipitation and caused the loss of micropores. In the Shirako fault, there is little evidence of deformation of illite crystals, and selective exfoliation of smectite layers with weaker interlayer bonding strength appears to have occurred. The reason for the deformation of the muscovite or illite crystals in the Nobeoka Fault may be due to the absence of a smectite phase as well as to even stronger shear stresses at depth.

A decrease in specific surface area and total nanopore volume is also observed in the PSZ compared to the footwall shales (Figs. 6.3 and 6.4). However, in contrast to the hanging wall, there is a marked increase in the volume fraction of micropores (Fig. 6.3),

which, when looking at the volume of mesopores and micropores, is likely due to the selective loss of mesopores and the simultaneous formation of micropores. XRD analysis indicated that the muscovite content is reduced and the illite content is increased in a complementary manner at the PSZ when compared to the values immediately below the PSZ (Fig. 6.4). Fukuchi et al. (2014) showed a decrease in illite crystallinity in the PSZ. These observations indicate that deformation or exfoliation of illite and probably detrital muscovite crystals has likely occurred. The retention of micropores in the PSZ may be due to the lower temperature environment than in the hanging wall, which resulted in a more subdued activity of fluid-mediated pressure solution. The illite crystallinity of the PSZ is even lower than in the damaged zone of the hanging wall (Fukuchi et al, 2014), suggesting that finer clay particles have been formed and these particles have filled the mesopores more efficiently, resulting in a reduced mesopore volume. Such clogging may have inhibited fluid circulation within the PSZ by causing a reduction in permeability, and may also have had a significant effect on the dynamic behaviour of the fault, such as causing thermal pressurization associated with coseismic high-velocity movements (Sibson, 1973).

6.5.3. Pore structure changes from shallow to deep subduction zones and their implications for seismogenic processes

In this section, the findings from the Nobeoka Fault are combined with data on the pore structure of intermediate-depth fault rocks such as the Kure mélange and on the shallow faults described earlier to examine how the pore structure changes from shallow to deep in the subduction zone and how it relates to the slip behaviour of the fault (Fig. 6.9). Figure 6.10 shows the relationships between the various parameters related to pore structures for all the analysed samples. Since BET specific surface area are generally highly correlated with micropore and mesopore volume, I will focus on this parameter in particular and discuss depth variation and its factor in the following. Figure 6.11 plots the specific surface area of the host rocks (undeformed sediments and tectonic mélange), excluding the data for the PSZ or damage zone, against the depth of each assumed sample. Samples from the Shirako Fault and the Nankai Trough (recovered at Site C0004 during the Integrated Ocean Drilling Program Exp. 316) have burial depths shallower than 1000 m, and generally have high values of more than 30 m^2/g. The Japan Trench sample is a pelagic clay in a fault-equivalent horizon (350 mbsf) recovered from the input site (Site 436, Deep Sear Drilling Program Leg 56/57), showing a specific surface area more than 60 m^2/g. This high value can be attributed to the high smectite content in the clay sample (>60 wt%; Kameda et al., 2015). On the other hand, samples that have experienced depths

greater than ~3 km show a sharp decrease in specific surface area, and this value appears to decrease further with depth. Figure 6.11 also shows how diagenetic or low-grade metamorphic reactions progress with depth, assuming Nankai Trough sediments (Moore and Saffer, 2001). In the depth range of ~1000 m to 3000 m, several diagenetic reactions, such as illitization of smectite and cementation of minerals, are thought to be active, and these effects suppress the swelling action of the sediments and fill nanopores, resulting in a significant decrease in specific surface area.

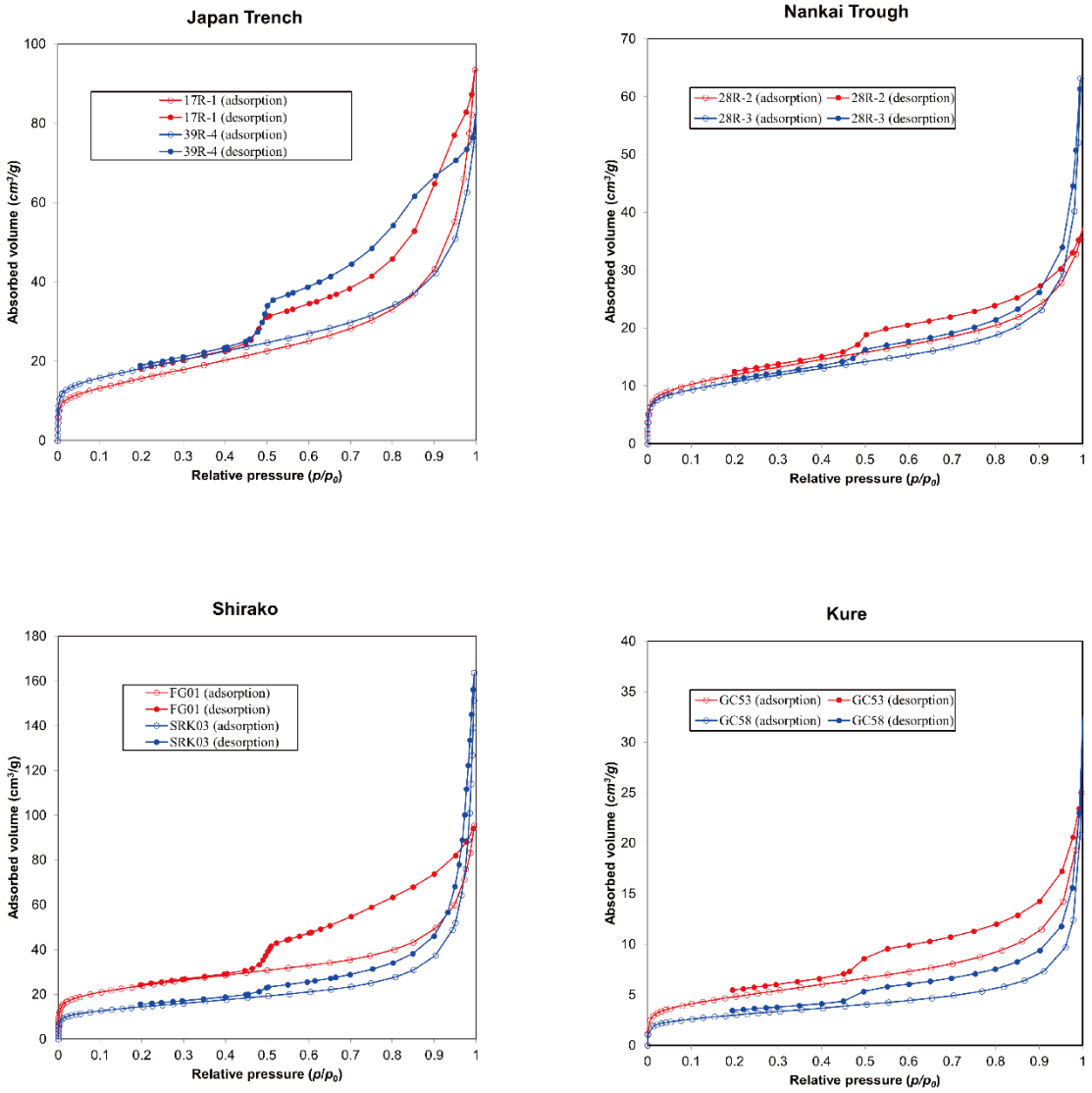

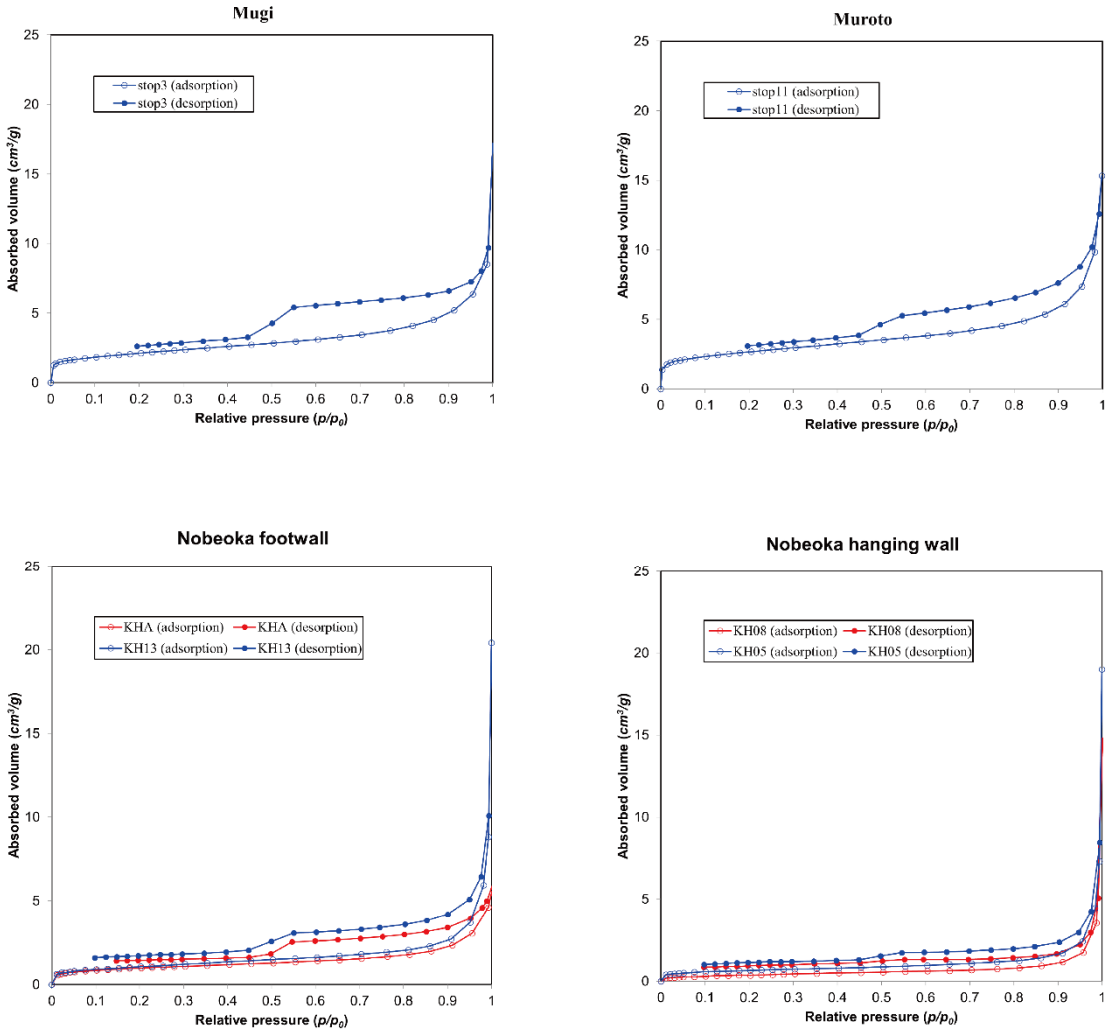

Figure 6.9. Typical isotherms of each fault zone. Red lines indicate gouge, PSZ, and damage zones. Blue lines indicate host sediment and mélange.

Table 6.3. Results of Porestructure analysis for all samples. Data of the PSZ and the damage zone are marked in bold.

Sample		Depth (m)	BET specific surface area (m^2/g)	Total pore volume (cm^3/g)	Micropore volume (cm^3/g)	Mesopore volume (cm^3/g)
Nankai Trough	25R-2	257	39.412	0.18	0.0072316	0.042168
	27R-1	266	32.897	0.080102	0.0059523	0.030125
	27R-2	267	44.513	0.1767	0.0072717	0.041082
	28R-1	270	15.913	0.055263	0.0028341	0.014718
	28R-2	271	36.761	0.088215	0.0065	0.033841
	28R-2	**271**	**42.092**	**0.055843**	**0.0092052**	**0.034492**
	28R-2	**271**	**41.462**	**0.056587**	**0.0087973**	**0.034666**
	28R-3	273	38.294	0.093305	0.0067758	0.035899
	29R-1	274	38.691	0.1041	0.0067687	0.035058
	30R-2	281	32.999	0.080065	0.00562	0.029686
	30R-3	282	42.957	0.1104	0.0075669	0.036845
Japan Trench	39R-4	365	64.861	0.1168	0.0093156	0.067729
	17R-1	**822**	**66.224**	**0.1017**	**0.010848**	**0.065381**
	17R-1	**822**	**67.398**	**0.1368**	**0.011071**	**0.073815**
	17R-1	**822**	**68.935**	**0.1442**	**0.011446**	**0.080382**
Shirako	SRK01	-1000[*1]	44.308	0.1349	0.0066661	0.059587
	SRK02	-1000[*1]	56.508	0.2086	0.0084593	0.072748
	SRK03	-1000[*1]	51.542	0.2393	0.0076472	0.069679
	SRK04	-1000[*1]	42.505	0.1888	0.0061859	0.05989
	SRK05	-1000[*1]	47.246	0.2126	0.0069393	0.065325
	SRK06	-1000[*1]	47.416	0.1369	0.0074571	0.058217
	SRK07	-1000[*1]	33.713	0.1432	0.0050569	0.046296
	SRK08	-1000[*1]	46.602	0.1357	0.0071914	0.057817
	SRK09	-1000[*1]	50.267	0.1748	0.0077393	0.065412
	SRK10	-1000[*1]	46.45	0.2156	0.0070961	0.062858
	SRK11	-1000[*1]	55.803	0.2005	0.0090234	0.067299
	SRK12	-1000[*1]	50.463	0.2007	0.0075489	0.067852
	SRK13	-1000[*1]	43.851	0.1689	0.0070487	0.052849
	SRK14	-1000[*1]	53.048	0.2451	0.0080325	0.068678
	SRK15	-1000[*1]	44.16	0.187	0.0067261	0.058451
	FG01	**-1000[*1]**	**85.774**	**0.1438**	**0.016134**	**0.075719**
	FG02	**-1000[*1]**	**78.993**	**0.1544**	**0.015171**	**0.081051**
Mugi	stop3	-3400[*2]	7.5307	0.015123	0.0011306	0.008278
	stop5	-3400[*2]	6.5322	0.015806	0.0013308	0.0070275
Muroto	stop9	-4000[*3]	13.356	0.016365	0.0023099	0.009138
	stop11	-4000[*3]	9.5485	0.021958	0.0016812	0.0092819
	stop12	-4000[*3]	8.3611	0.016976	0.0013611	0.006349
Kure	**GC52**	**-4500[*4]**	**14.343**	**0.038702**	**0.0029985**	**0.016467**
	GC53	**-4500[*4]**	**17.046**	**0.039102**	**0.0035908**	**0.018625**
	GC58	-4500[*4]	10.666	0.04009	0.0019728	0.01169
Nobeoka	KH01	-11000[*5]	5.05	0.0182	0.0015914	0.006855
	KH02	-11000[*5]	1.69	0.0168	0.00029547	0.0027408
	KH03	-11000[*5]	1.91	0.0108	0.0008171	0.0029735
	KH04	-11000[*5]	2.18	0.0153	0.00037477	0.0033959
	KH05	-11000[*5]	2.35	0.0183	0.00044086	0.0030579
	KH06	-11000[*5]	3.12	0.0153	0.00071711	0.0035434
	KH07	-11000[*5]	2.36	0.0153	0.00046301	0.0034995
	KH08	**-11000[*5]**	**1.2**	**0.0088**	**0.00022872**	**0.0023664**
	KH09	**-11000[*5]**	**1.25**	**0.0094**	**0.00037689**	**0.0032625**
	KHA	**-8000[*5]**	**3.47**	**0.0081**	**0.0012151**	**0.0038501**
	KHB	**-8000[*5]**	**3.82**	**0.0079**	**0.0011066**	**0.0040079**
	KH13	-8000[*5]	3.75	0.0186	0.00068642	0.0052202
	KH14	-8000[*5]	3.64	0.0153	0.0011664	0.0055367
	KH15	-8000[*5]	4.12	0.0114	0.00039416	0.0046997
	KH16	-8000[*5]	5.54	0.0124	0.0010712	0.0054595
	KH17	-8000[*5]	5.79	0.0216	0.0010872	0.0068292
	KH18	-8000[*5]	5.19	0.018	0.001122	0.0052341
	KH19	-8000[*5]	4.4	0.0184	0.00097293	0.0054215
	KH20	-8000[*5]	5	0.014	0.00119	0.0051341
	KH21	-8000[*5]	5.26	0.0173	0.00092062	0.0055276
	KH22	-8000[*5]	4.01	0.0126	0.00060706	0.0047514
	KH23	-8000[*5]	3.57	0.0151	0.0007126	0.0041947
	KH24	-8000[*5]	2.16	0.0092	0.00036596	0.0029908
	KH25	-8000[*5]	4.88	0.0187	0.00076892	0.0061251
	KH26	-8000[*5]	4.56	0.0165	0.00090135	0.0054397
	KH27	-8000[*5]	6.56	0.0278	0.00088224	0.0086564
	KH28	-8000[*5]	5.5	0.0224	0.00080145	0.0074133
	KH29	-8000[*5]	4.54	0.0134	0.00088298	0.0053491
	KH30	-8000[*5]	6.68	0.0125	0.001093	0.0057367
	KH31	-8000[*5]	5.1	0.0141	0.00082397	0.0061102
	KH32	-8000[*5]	4.43	0.0194	0.00068679	0.0059998

*1 Yamamoto et al. (2006), *2 Ohmori (2001), *3 Mori and Taguchi (1988), *4 Mukoyoshi et al. (2006), *5 Kondo et al. (2005).

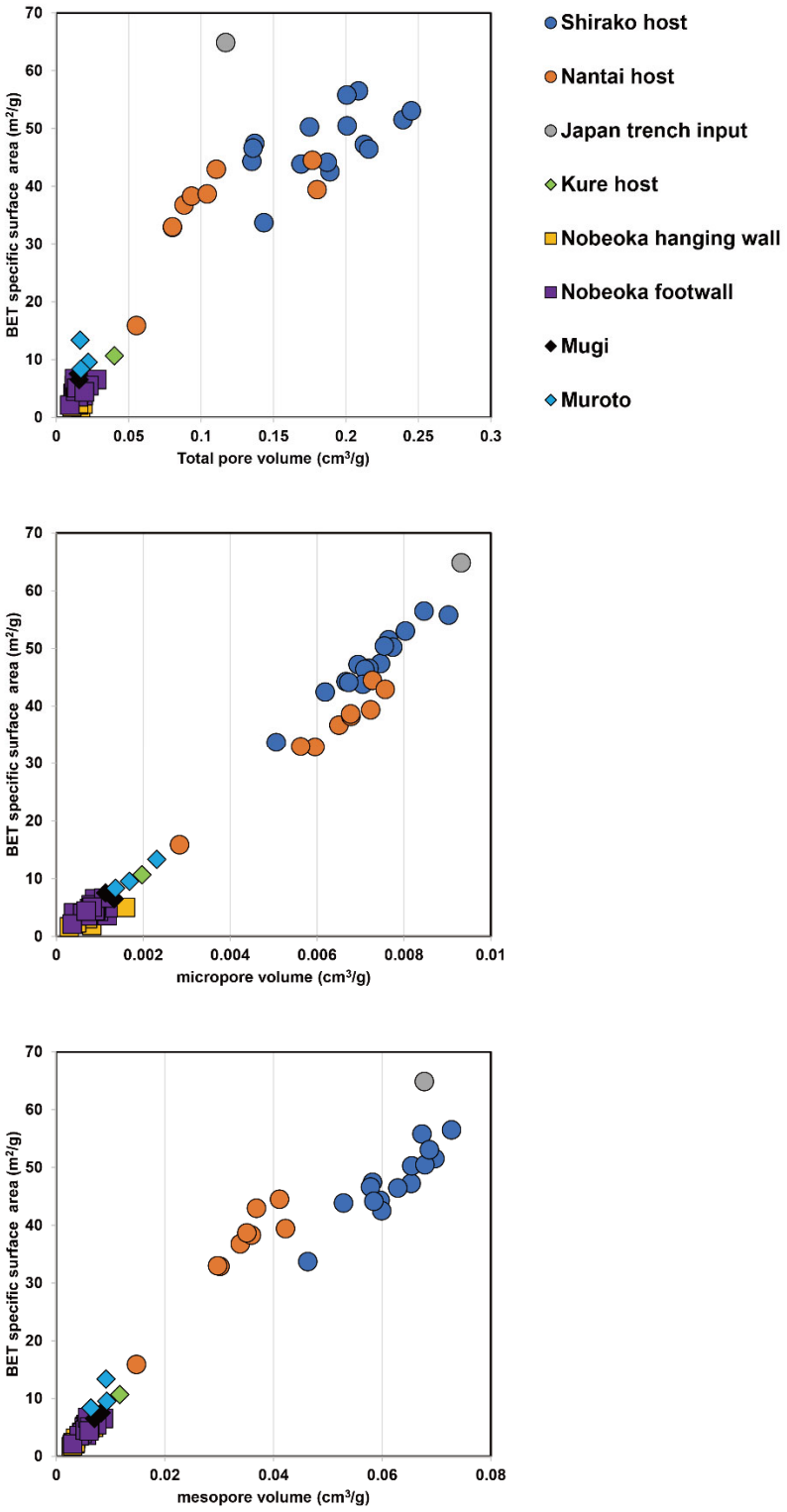

Figure 6.10. Correlation of pore structure parameters to BET specific surface area in host rock. (a) Total pore volume. (b) Micropore volume. (c) Mesopore volume.

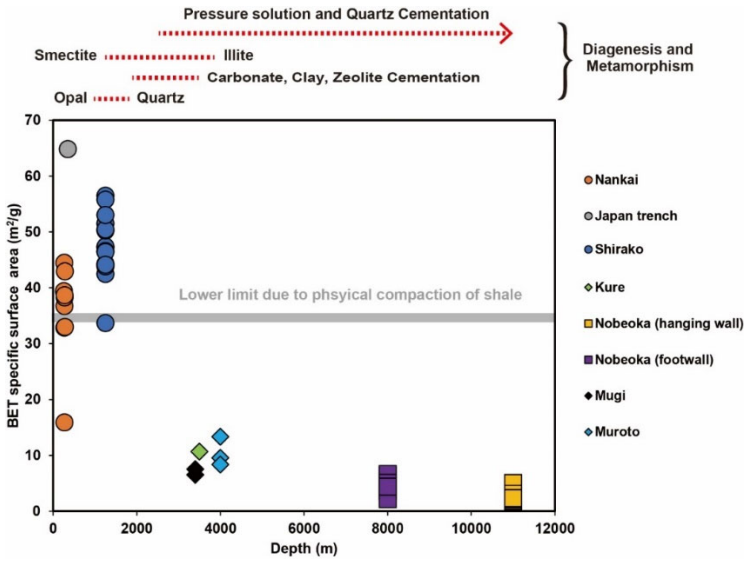

Figure 6.11. Relationship between BET specific surface area and depth in host rock. Red dotted lines indicate the depth range of diagenesis and metamorphism (Moore and Saffer, 2001). Gray area is the lower limit of specific surface area due to mechanical compaction (Seiphoori et al., 2017).

At greater depths, pressure-solution deformation associated with mélange formation is expected to contribute to the filling of nanopores as argued in the previous section, further reducing the specific surface area. These assumed processes are also in good agreement with observations in fault rocks (Kondo et al., 2005; Mukoyoshi et al., 2006). In addition, the lower limit of specific surface area achieved by physical loading alone in shale consolidation experiments conducted by Seiphoori et al. (2017) is around 33 m^2/g (grey line in Fig. 6.11), which is also consistent with the present observation.

Figure 6.12 shows how coseismic or cataclastic deformation can cause changes of the specific surface area (on a logarithmic scale) to these host rocks (blue area). In this figure, the area shown in red is for the combined samples from the PSZ and from the damage zone. The figure also shows the aseismic-seismic traction in the Nankai Trough where the seismogenic zone corresponds to the estimated rupture area of the 1946 Nankai earthquake (Satake, 1993). Even in the shallow aseismic zone, recent studies have shown that coseismic slip is likely to have occurred in the Nankai Trough and on the Shirako Fault (Sakaguchi et al., 2011; Kameda et al., 2013), but it should be noted that such slips were those propagated from depths, not that the rupture started in situ. In the 2011 Tohoku-oki earthquake, the rupture and slip actually propagated up to the frontal tip of

the Japan Trench (Ide et al., 2011). On the other hand, the so-called seismogenic zone is thought to be composed of materials that could nucleate rupture and slip. In the physics of earthquake generation, such materials are considered to exhibit velocity-weakening behaviour (a property that decreases frictional strength when an increase in displacement velocity occurs; Scholz, 1990). Interestingly, as shown in Figure 6.12, the direction of change in specific surface area with coseismic or cataclastic deformation changes almost in line with this transition (aseismic-seismic transition). In the shallow aseismic zone, the specific surface area tends to increase due to seismic slip, whereas in the deeper seismogenic zone it is almost unchanged or rather decreases. As described so far, the change in specific surface area and the associated changes in pore structures are considered to be strongly related to the presence or absence of fluid-mediated diagenetic reaction. In fact, Moore and Saffer (2001) point out that the combined effects of various diagenetic processes at a depth of around 4 km are crucial for the onset of the seismogenic zones. Friction experiments have also shown that lithification by diagenetic reactions is an essential process for sediments to exhibit rate-weakening behaviour (Trütner et al., 2015). One of the key findings of this study is that the effects of these diagenetic reactions have been recorded in PSZs and fracture zones of the Nobeoka Fault, which may be related to the post-seismic strength recovery process. Changes in frictional properties and strength recovery processes associated with the diagenetic reactions may therefore be related to the repeated nucleation of earthquakes in seismogenic zone. On the other hand, in the shallow fault zones, the specific surface area (including the volume of nanopores, etc.) of the fault that has undergone seismic slip is held at an increased level, which is expected to result in little progress in diagenetic reaction and no significant increase or decrease in fault strength. This means that there are also unlikely to be significant variations in the buffer capacity of seismogenic rupture and slips propagating from depth. The progression of diagenesis has been assessed mainly on the basis of microstructural observations by optical microscopy and SEM, or mineral composition by XRD, but this study suggests that gas adsorption analysis is a more quantitative method of assessment. More applications to experimentally deformed samples and natural fault samples would further improve our understanding of the mechanisms of earthquake generation in subduction zones.

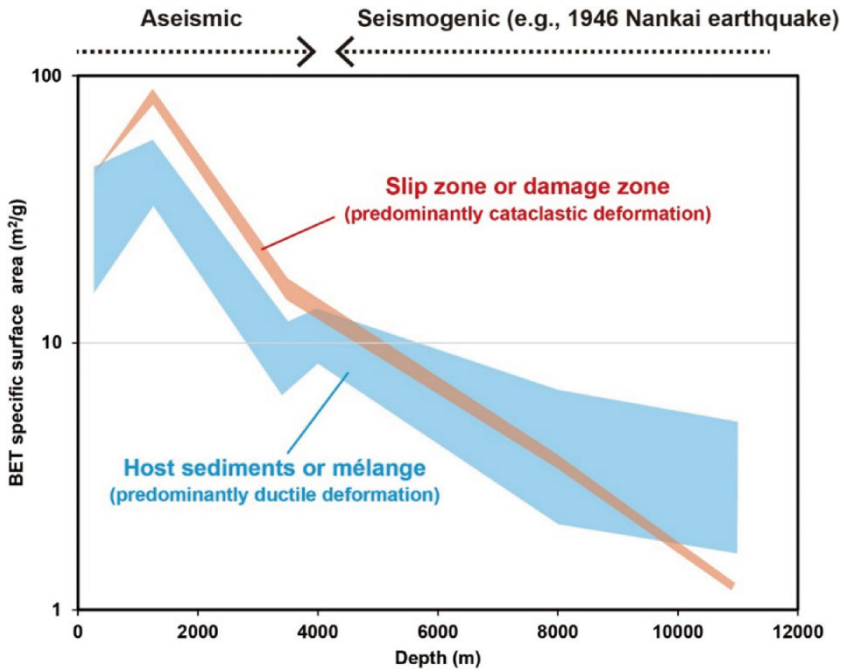

Figure 6.12. Relationship between BET specific surface area for the slip zone or damage zone samples (red) and the host sediment or mélange samples (blue). The black dotted line corresponds to the rupture area of the 1946 Nankai earthquake (Satake 1993).

References

Avnir, D., & Jaroniec, M. (1989). An isotherm equation for adsorption on fractal surfaces of heterogeneous porous materials. *Langmuir*, *5*(6), 1431–1433.

Barrett, E. P., Joyner, L. G., & Halenda, P. P. (1951). The Determination of Pore Volume and Area Distributions in Porous Substances. I. Computations from Nitrogen Isotherms. *Journal of the American Chemical Society*, *73*(1), 373–380.

Bolt, G. H. (1955). Analysis of the validity of the Gouy-Chapman theory of the electric double layer. *Journal of Colloid Science*, *10*(2), 206–218.

Brown, K. M., & Ransom, B. (1996). Porosity corrections for smectite-rich sediments: Impact on studies of compaction, fluid generation, and tectonic history. *Geology*, *24*(9), 843–846.

Brunauer, S., Emmett, P. H., & Teller, E. (1938). Adsorption of Gases in Multimolecular Layers. *Journal of the American Chemical Society*, *60*(2), 309–319.

Chatterji, P. K., Morgenstern, N., & others. (1990). *A modified shear strength formulation for swelling clay soils*. ASTM International.

Chen, L., Jiang, Z., Liu, K., Tan, J., Gao, F., & Wang, P. (2017). Pore structure characterization for organic-rich Lower Silurian shale in the Upper Yangtze Platform, South China: A possible mechanism for pore development. *Journal of Natural Gas Science and Engineering*, *46*, 1–15.

Chester, F. M., Mori, J. J., Toczko, S., Eguchi, N., & Expedition 343/343T Scientists. (2012). *Integrated Ocean Drilling Program Expedition 343/343T Preliminary Report*. Integrated Ocean Drilling Program.

Chester, F. M., Rowe, C., Ujiie, K., Kirkpatrick, J., Regalla, C., Remitti, F., Moore, J. C., Toy, V., Wolfson-Schwehr, M., Bose, S., Kameda, J., Mori, J. J., Brodsky, E. E., Eguchi, N., Toczko, S., & Expedition 343 and 343T Scientists. (2013). Structure and Composition of the Plate-Boundary Slip Zone for the 2011 Tohoku-Oki Earthquake. *Science*, *342*(6163), 1208–1211.

Conin, M., Henry, P., Bourlange, S., Raimbourg, H., & Reuschlé, T. (2011). Interpretation of porosity and LWD resistivity from the Nankai accretionary wedge in light of clay physicochemical properties: Evidence for erosion and local overpressuring. *Geochemistry, Geophysics, Geosystems*, *12*(3).

Daigle, H. (2014). Microporosity development in shallow marine sediments from the Nankai Trough. *Marine Geology*, *357*, 293–303.

Derjaguin, B., & Landau, L. (1941). Theory of the stability of strongly charged

lyophobic sols and of the adhesion of strongly charged particles in solutions of electrolytes. *Progress in Surface Science*, *43*(1–4), 30–59.

Desbois, G., Urai, J., & Kukla, P. (2009). Morphology of the pore space in claystones—Evidence from BIB/FIB ion beam sectioning and cryo-SEM observations. *EEarth*, *4*.

Durán, J. D. G., Ramos-Tejada, M. M., Arroyo, F. J., & González-Caballero, F. (2000). Rheological and Electrokinetic Properties of Sodium Montmorillonite Suspensions: I. Rheological Properties and Interparticle Energy of Interaction. *Journal of Colloid and Interface Science*, *229*(1), 107–117.

Dutilleul, J., Bourlange, S., Conin, M., & Géraud, Y. (2020). Quantification of bound water content, interstitial porosity and fracture porosity in the sediments entering the North Sumatra subduction zone from Cation Exchange Capacity and IODP Expedition 362 resistivity data. *Marine and Petroleum Geology*, *111*, 156–165.

Dutilleul, J., Bourlange, S., Géraud, Y., & Stemmelen, D. (2020). Porosity, Pore Structure, and Fluid Distribution in the Sediments Entering the Northern Hikurangi Margin, New Zealand. *Journal of Geophysical Research: Solid Earth*, *125*(11).

Eberl, D. D. (2003). User Guide to RockJock—A Program for Determining Quantitative Mineralogy from X-Ray Diffraction Data. In *User Guide to RockJock—A Program for Determining Quantitative Mineralogy from X-Ray Diffraction Data* (USGS Numbered Series No. 2003–78; Open-File Report, Vols. 2003–78). U.S. Geological Survey.

Evans, J. P., & Chester, F. M. (1995). Fluid-rock interaction in faults of the San Andreas system: Inferences from San Gabriel fault rock geochemistry and microstructures. *Journal of Geophysical Research: Solid Earth*, *100*(B7), 13007–13020.

Fitts, T. G., & Brown, K. M. (1999). Stress-induced smectite dehydration: Ramifications for patterns of freshening and fluid expulsion in the N. Barbados accretionary wedge. *Earth and Planetary Science Letters*, *172*(1–2), 179–197.

Fujii, Y., Satake, K., Sakai, S., Shinohara, M., & Kanazawa, T. (2011). Tsunami source of the 2011 off the Pacific coast of Tohoku Earthquake. *Earth, Planets and Space*, *63*(7), 815–820.

Fukuchi, R., Fujimoto, K., Kameda, J., Hamahashi, M., Yamaguchi, A., Kimura, G., Hamada, Y., Hashimoto, Y., Kitamura, Y., & Saito, S. (2014). Changes in illite crystallinity within an ancient tectonic boundary thrust caused by thermal, mechanical, and hydrothermal effects: An example from the Nobeoka Thrust, southwest Japan. *Earth, Planets and Space*, *66*(1), 116.

Giese, R. F. (1974). Surface energy calculations for muscovite. *Nature*, *248*(5449), Article 5449.

Giese, R. F. (1978). The Electrostatic Interlayer Forces of Layer Structure Minerals. *Clays and Clay Minerals*, *26*(1), 51–57.

Hamada, Y., Hirono, T., & Ishikawa, T. (2011). Coseismic frictional heating and fluid-rock interaction in a slip zone within a shallow accretionary prism and implications for earthquake slip behavior. *Journal of Geophysical Research: Solid Earth*, *116*(B1).

Hamahashi, M., Hamada, Y., Yamaguchi, A., Kimura, G., Fukuchi, R., Saito, S., Kameda, J., Kitamura, Y., Fujimoto, K., & Hashimoto, Y. (2015). Multiple damage zone structure of an exhumed seismogenic megasplay fault in a subduction zone—A study from the Nobeoka Thrust Drilling Project. *Earth, Planets and Space*, *67*(1), 30.

Hamahashi, M., Saito, S., Kimura, G., Yamaguchi, A., Fukuchi, R., Kameda, J., Hamada, Y., Kitamura, Y., Fujimoto, K., Hashimoto, Y., Hina, S., & Eida, M. (2013). Contrasts in physical properties between the hanging wall and footwall of an exhumed seismogenic megasplay fault in a subduction zone-An example from the Nobeoka Thrust Drilling Project: PHYSICAL PROPERTY OF EXHUMED SPLAY FAULT. *Geochemistry, Geophysics, Geosystems*, *14*(12), 5354–5370.

Hanamura, Y., & Ogawa, Y. (1993). Layer-parallel faults, duplexes, imbricate thrusts and vein structures of the Miura Group: Keys to understanding the Izu fore-arc sediment accretion to the Honshu fore arc. *The Island Arc*, *2*(3), 126–141.

Hasegawa, R., Yamaguchi, A., Fukuchi, R., Hamada, Y., Ogawa, N., Kitamura, Y., Kimura, G., Ashi, J., & Ishikawa, T. (2019). Postseismic fluid discharge chemically recorded in altered pseudotachylyte discovered from an ancient megasplay fault: An example from the Nobeoka Thrust in the Shimanto accretionary complex, SW Japan. *Progress in Earth and Planetary Science*, *6*(1),

Hedin, A. (2004). *Integrated near-field evolution model for a KBS-3 repository*.

Hogg, R., Cahn, D. S., Healy, T. W., & Fuerstenau, D. W. (1966). Diffusional mixing in an ideal system. *Chemical Engineering Science*, *21*(11), 1025–1038.

Hüpers, A., Torres, M. E., Owari, S., McNeill, L. C., Dugan, B., Henstock, T. J., Milliken, K. L., Petronotis, K. E., Backman, J., Bourlange, S., Chemale, F., Chen, W., Colson, T. A., Frederik, M. C. G., Guèrin, G., Hamahashi, M., House, B. M., Jeppson, T. N., Kachovich, S., … Zhao, X. (2017). Release of mineral-bound water prior to subduction tied to shallow seismogenic slip off Sumatra. *Science*, *356*(6340), 841–844.

Ide, S., Baltay, A., & Beroza, G. C. (2011). Shallow Dynamic Overshoot and Energetic Deep Rupture in the 2011 Mw 9.0 Tohoku-Oki Earthquake. *Science*, *332*(6036), 1426–1429.

Ikari, M. J., Saffer, D. M., & Marone, C. (2007). Effect of hydration state on the frictional properties of montmorillonite-based fault gouge. *Journal of Geophysical Research: Solid Earth*, *112*(B6).

Ikehara-Ohmori, K., (2001). The thermal structure of the Shimanto Belt and accretionary denudation. *Chikyu monthly/special*, (32), 174-180.

Inoue, A. (1989). Convenient Technique for Estimating Smectite Layer Percentage in Randomly Interstratified Illite/Smectite Minerals. *Clays and Clay Minerals*, *37*(3), 227–234.

Israelachvili, J. N. (2011). *Intermolecular and surface forces*. Academic press.

Ito M., Okamoto M., Suzuki K., Shibata M., & Sasaki Y. (1994). Mineral Composition Analysis of Bentonite. *Journal of the Atomic Energy Society of Japan / Atomic Energy Society of Japan*, *36*(11), 1055–1058.

Kameda, J., & Hamada, Y. (2020). Cohesional Slip on a Plate Subduction Boundary During a Large Earthquake. *Geophysical Research Letters*, *47*(18), e2020GL088395.

Kameda, J., & Hamada, Y. (2022). Stick-slip behavior of a clayey crustal fault. *Physical Review Research*, *4*(1), 013211.

Kameda, J., Inaoi, C., & Conin, M. (2016). Exchangeable cation composition of the smectite-rich plate boundary fault at the Japan Trench. *Geophysical Research Letters*, *43*(7), 3112–3119.

Kameda, J., & Morisaki, T. (2017). Sensitivity of Clay Suspension Rheological Properties to pH, Temperature, Salinity, and Smectite-Quartz Ratio. *Geophysical Research Letters*, *44*(19), 9615–9621.

Kameda, J., & Okamoto, A. (2021). 1-D inversion analysis of a shallow landslide triggered by the 2018 Eastern Iburi earthquake in Hokkaido, Japan. *Earth, Planets and Space*, *73*(1), 116.

Kameda, J., Raimbourg, H., Kogure, T., & Kimura, G. (2011). Low-grade metamorphism around the down-dip limit of seismogenic subduction zones: Example from an ancient accretionary complex in the Shimanto Belt, Japan. *Tectonophysics*, *502*(3), 383–392.

Kameda, J., Saruwatari, K., & Tanaka, H. (2003). H_2 generation in wet grinding of granite and single-crystal powders and implications for H_2 concentration on active faults. *Geophysical Research Letters*, *30*(20), 2003GL018252.

Kameda, J., Shimizu, M., Ujiie, K., Hirose, T., Ikari, M., Mori, J., Oohashi, K., & Kimura, G. (2015). Pelagic smectite as an important factor in tsunamigenic slip along the Japan Trench. *Geology*, *43*(2), 155–158.

Kameda, J., Uno, M., Conin, M., Ujiie, K., Hamada, Y., & Kimura, G. (2019). Fault weakening caused by smectite swelling. *Earth, Planets and Space*, *71*(1), 131.

Kameda, J., Yamamoto, Y., Hamada, Y., Fujimoto, K., & Kimura, G. (2013). Progress of illitization along an imbricate frontal thrust at shallow depths in an accretionary prism. *Tectonophysics*, *600*, 41–51.

Karnland, O., Olsson, S., & Nilsson, U. (2006). *Mineralogy and sealing properties of various bentonites and smectite-rich clay materials*. Swedish Nuclear Fuel and Waste Management Co.

Kaufhold, S., Färber, G., Dohrmann, R., Ufer, K., & Grathoff, G. (2015). Zn-rich smectite from the Silver Coin Mine, Nevada, USA. *Clay Minerals*, *50*(4), 417–430.

Kawakami, S. (2001). Upper Miocene radiolarians from the Nishizaki Formation and Ishido Group in the southern part of Boso Peninsula, Japan, and their geological significance. *News of Osaka Micropaleontologists (NOM)*, *12*, 343–358.

Keren, R., & Shainberg, I. (1975). Water Vapor Isotherms and Heat of Immersion of Na/Ca-Montmorillonite Systems—I: Homoionic Clay. *Clays and Clay Minerals*, *23*(3), 193–200.

Kodaira, S., No, T., Nakamura, Y., Fujiwara, T., Kaiho, Y., Miura, S., Takahashi, N., Kaneda, Y., & Taira, A. (2012). Coseismic fault rupture at the trench axis during the 2011 Tohoku-oki earthquake. *Nature Geoscience*, *5*(9), 646–650.

Komine, H., & Ogata, N. (2004). Predicting Swelling Characteristics of Bentonites. *Journal of Geotechnical and Geoenvironmental Engineering*, *130*(8), 818–829.

Komine, H., Yasuhara, K., & Murakami, S. (2009). Swelling characteristics of bentonites in artificial seawater. *Canadian Geotechnical Journal*, *46*(2), 177–189.

Kondo, H., Kimura, G., Masago, H., Ohmori-Ikehara, K., Kitamura, Y., Ikesawa, E., Sakaguchi, A., Yamaguchi, A., & Okamoto, S. (2005). Deformation and fluid flow of a major out-of-sequence thrust located at seismogenic depth in an accretionary complex: Nobeoka Thrust in the Shimanto Belt, Kyushu, Japan: NOBEOKA THRUST, A SEISMOGENIC OST. *Tectonics*, *24*(6),.

Kong, L., Hadavimoghaddam, F., Li, C., Liu, K., Liu, B., Semnani, A., & Ostadhassan, M. (2021). AFM vs. Nanoindentation: Nanomechanical properties of organic-rich Shale. *Marine and Petroleum Geology*, *132*, 105229.

Kuila, U., & Prasad, M. (2013). Specific surface area and pore-size distribution in clays and shales: *Specific surface area and pore-size distribution in clays and shales*.

Geophysical Prospecting, *61*(2), 341–362.

Lee, I., & Ogawa, Y. (1998). Bottom-current deposits in the Miocene–Pliocene Misaki Formation, Izu forearc area, Japan. *Island Arc*, *7*(3), 315–329.

Li, H., Xu, Z., Niu, Y., Kong, G., Huang, Y., Wang, H., Si, J., Sun, Z., Pei, J., Gong, Z., Chevalier, M.-L., & Liu, D. (2014). Structural and physical property characterization in the Wenchuan earthquake Fault Scientific Drilling project—Hole 1 (WFSD-1). *Tectonophysics*, *619–620*, 86–100.

Li, T., Jiang, Z., Xu, C., Liu, B., Liu, G., Wang, P., Li, X., Chen, W., Ning, C., & Wang, Z. (2017). Effect of pore structure on shale oil accumulation in the lower third member of the Shahejie formation, Zhanhua Sag, eastern China: Evidence from gas adsorption and nuclear magnetic resonance. *Marine and Petroleum Geology*, *88*, 932–949.

Li, Y., Wang, Z., Pan, Z., Niu, X., Yu, Y., & Meng, S. (2019). Pore structure and its fractal dimensions of transitional shale: A cross-section from east margin of the Ordos Basin, China. *Fuel*, *241*, 417–431.

Liu, X., Xiong, J., & Liang, L. (2015). Investigation of pore structure and fractal characteristics of organic-rich Yanchang formation shale in central China by nitrogen adsorption/desorption analysis. *Journal of Natural Gas Science and Engineering*, *22*, 62–72.

Logan, J. M., & Rauenzahn, K. A. (1987). Frictional dependence of gouge mixtures of quartz and montmorillonite on velocity, composition and fabric. *Tectonophysics*, *144*(1–3), 87–108.

Loucks, R. G., Reed, R. M., Ruppel, S. C., & Hammes, U. (2012). Spectrum of pore types and networks in mudrocks and a descriptive classification for matrix-related mudrock pores. *AAPG Bulletin*, *96*(6), 1071–1098.

Loucks, R. G., Reed, R. M., Ruppel, S. C., & Jarvie, D. M. (2009). Morphology, Genesis, and Distribution of Nanometer-Scale Pores in Siliceous Mudstones of the Mississippian Barnett Shale. *Journal of Sedimentary Research*, *79*(12), 848–861.

Marone, C., & Scholz, C. H. (1989). Particle-size distribution and microstructures within simulated fault gouge. *Journal of Structural Geology*, *11*(7), 799–814.

Masumoto, H., Kameda, J., Arima, H., Sugiyama, K., Nagai, T., & Yamamoto, Y. (2018). Dehydroxylation Kinetics of Clay Minerals and Its Application to Friction Heating Along an Imbricate Thrust in an Accretionary Prism. *Geochemistry, Geophysics, Geosystems*, *19*(9), 2991–3003.

McCreesh, C., & Robert E. (1991). Petrography and Reservoir Physics II: Relating Thin Section Porosity to Capillary Pressure, the Association Between Pore Types and

Throat Size (1). *AAPG Bulletin*, *75*.

McNeill, L. C., Dugan, B., & Petronotis, K. E. (2017). Sumatra Subduction Zone. *Proceedings of the International Ocean Discovery Program*, *362*.

Mitchell, J. K., & Soga, K. (2005). *Fundamentals of Soil Behavior*. 560.

Miyawaki R., Sano T., Oohashi F., Suzuki M., Kogure T., Okumura T., Kameda J., Umezome T., Sato T., Chino D., Hiroyama K., Yamada H., Tamura K., Morimoto K., Uehara S., & Hatta T. (2010). *Some Reference Data for the JCSS CIay Specimens* (No. 4). The Clay Science Society of Japan.

Montoro, M. A., & Francisca, F. M. (2019). Effect of ion type and concentration on rheological properties of natural sodium bentonite dispersions at low shear rates. *Applied Clay Science*, *178*, 105132.

Monzawa, N., & Otsuki, K. (2003). Comminution and fluidization of granular fault materials: Implications for fault slip behavior. *Tectonophysics*, *367*(1), 127–143.

Moore, D. E., & Lockner, D. A. (2007). 11. Friction of the Smectite Clay Montmorillonite: A Review and Interpretation of Data. In T. H. Dixon & C. Moore (Eds.), *The Seismogenic Zone of Subduction Thrust Faults* (pp. 317–345). Columbia University Press.

Moore, J. C., & Saffer, D. (2001). Updip limit of the seismogenic zone beneath the accretionary prism of southwest Japan: An effect of diagenetic to low-grade metamorphic processes and increasing effective stress. *Geology*, *29*(2), 183–186.

Mori, K., & Taguchi, K., (1988). Examination of the low-grade metamorphism in the Shimanto Belt by vitrinite reflectance. *Modern geology* 12, 325– 339.

Mukoyoshi, H., Sakaguchi, A., Otsuki, K., Hirono, T., & Soh, W. (2006). Co-seismic frictional melting along an out-of-sequence thrust in the Shimanto accretionary complex. Implications on the tsunamigenic potential of splay faults in modern subduction zones. *Earth and Planetary Science Letters*, *245*(1–2), 330–343.

Murata, A. (1998). Duplexes and low-angle nappe structures of the Shimanto terrane, southwest Japan. *Memoir of Geological Society of Japan*, *50*, 147.

Nakamoto, K., Kamei, M., & Kameda, J. (2023). Surface Physicochemical Properties of Smectite-Rich Fault Gouge: A Case Study of the Japan Trench Plate-Boundary Fault. Geophysical Research Letters, 50(11), e2023GL104271.

Oohashi, K., Hirose, T., Takahashi, M., & Tanikawa, W. (2015). Dynamic weakening of smectite-bearing faults at intermediate velocities: Implications for subduction zone earthquakes. *Journal of Geophysical Research: Solid Earth*, *120*(3), 1572–1586.

Oohashi, K., Lin, W., Wu, H.-Y., Yamaguchi, A., & Yamamoto, Y. (2017). Stress State

in the Kumano Basin and in Slope Sediment Determined From Anelastic Strain Recovery: Results From IODP Expedition 338 to the Nankai Trough. *Geochemistry, Geophysics, Geosystems*, *18*(10), 3608–3616.

Otsuki, A. (2018). Coupling colloidal forces with yield stress of charged inorganic particle suspension: A review. *ELECTROPHORESIS*, *39*(5–6), 690–701.

Passey, Q. R., Bohacs, K. M., Esch, W. L., Klimentidis, R. ., & Sinha, S. . (2010). From Oil-Prone Source Rock to Gas-Producing Shale Reservoir – Geologic and Petrophysical Characterization of Unconventional Shale-Gas Reservoirs. *All Days*, SPE-131350-MS.

Plaza, I., Ontiveros-Ortega, A., Calero, J., & Romero, C. (2018). A new approach to triggering mechanism of volcano landslides based on zeta potential and surface free energy balance. *Geomorphology*, *301*, 1–9.

Qin, L., Wang, P., Li, S., Lin, H., Wang, R., Wang, P., & Ma, C. (2021). Gas adsorption capacity changes in coals of different ranks after liquid nitrogen freezing. *Fuel*, *292*, 120404.

Raimbourg, H., Tadahiro, S., Asuka, Y., Haruka, Y., & Kimura, G. (2009). Horizontal shortening versus vertical loading in accretionary prisms. *Geochemistry, Geophysics, Geosystems*, *10*(4).

Ren, Y., Yang, S., Andersen, K. H., Yang, Q., & Wang, Y. (2021). Thixotropy of soft clay: A review. *Engineering Geology*, *287*, 106097.

Reynolds Jr, R. (1985). NEWMOD©. *A Computer Program for the Calculation of One-Dimensional Diffraction Patterns of Mixed-Layered Clay*.

Reynolds, R. C. (1992). X-ray Diffraction Studies of Illite/Smectite from Rocks, < 1 μm Randomly Oriented Powders, and < 1 μm Oriented Powder Aggregates: The Absence of Laboratory-Induced Artifacts. *Clays and Clay Minerals*, *40*(4), 387–396.

Rubio-Hernandez, F., Carrique, F., & Ruiz-Reina, E. (2004). The primary electroviscous effect in colloidal suspensions. *Advances in Colloid and Interface Science*, *107*(1), 51–60.

Saffer, D. M., Frye, K. M., Marone, C., & Mair, K. (2001). Laboratory results indicating complex and potentially unstable frictional behavior of smectite clay. *Geophysical Research Letters*, *28*(12), 2297–2300.

Saffer, D. M., Frye, K. M., Marone, C., & Mair, K. (2001). Laboratory results indicating complex and potentially unstable frictional behavior of smectite clay. *Geophysical Research Letters, 28(12),* 2297-2300.

Sakaguchi, A., Chester, F., Curewitz, D., Fabbri, O., Goldsby, D., Kimura, G., Li, C.-F.,

Masaki, Y., Screaton, E. J., Tsutsumi, A., Ujiie, K., & Yamaguchi, A. (2011). Seismic slip propagation to the updip end of plate boundary subduction interface faults: Vitrinite reflectance geothermometry on Integrated Ocean Drilling Program NanTro SEIZE cores. *Geology*, *39*(4), 395–398.

Sakuma, H., & Suehara, S. (2015). Interlayer bonding energy of layered minerals: Implication for the relationship with friction coefficient. *Journal of Geophysical Research: Solid Earth*, *120*(4), 2212–2219.

Saruwatari, K., Kameda, J., & Tanaka, H. (2004). Generation of hydrogen ions and hydrogen gas in quartz–water crushing experiments: An example of chemical processes in active faults. *Physics and Chemistry of Minerals*, *31*(3), 176–182.

Satake, K. (1993). Depth distribution of coseismic slip along the Nankai Trough, Japan, from joint inversion of geodetic and tsunami data. *Journal of Geophysical Research: Solid Earth*, *98*(B3), 4553–4565.

Sawai, M., Shimamoto, T., & Togo, T. (2012). Reduction in BET surface area of Nojima fault gouge with seismic slip and its implication for the fracture energy of earthquakes. *Journal of Structural Geology*, *38*, 117–138.

Schieber, J. (2010). *Common Themes in the Formation and Preservation of Intrinsic Porosity in Shales and Mudstones – Illustrated With Examples Across the Phanerozoic*. SPE Unconventional Gas Conference.

Schleicher, A. M., Boles, A., & van der Pluijm, B. A. (2015). Response of natural smectite to seismogenic heating and potential implications for the 2011 Tohoku earthquake in the Japan Trench. *Geology*, *43*(9), 755–758.

Schleicher, A. M., Warr, L. N., & Van Der Pluijm, B. A. (2009). On the origin of mixed-layered clay minerals from the San Andreas Fault at 2.5–3 km vertical depth (SAFOD drillhole at Parkfield, California). *Contributions to Mineralogy and Petrology*, *157*(2), 173–187.

Scholz, C. H. (2002). *Earthquakes and faulting*. Cambridge University Press Cambridge.

Sibson, R. (1977). Fault rocks and fault mechanics. *Journal of the Geological Society*, *133*, 191–213.

Sibson, R. H. (1973). Interactions between Temperature and Pore-Fluid Pressure during Earthquake Faulting and a Mechanism for Partial or Total Stress Relief. *Nature Physical Science*, *243*(126), Article 126.

Sing, K. S. (1985). Reporting physisorption data for gas/solid systems with special reference to the determination of surface area and porosity (Recommendations 1984). *Pure and applied chemistry*, *57*(4), 603-619

Slatt, R. M., & O'Brien, N. R. (2011). Pore types in the Barnett and Woodford gas shales: Contribution to understanding gas storage and migration pathways in fine-grained rocks. *AAPG Bulletin*, *95*(12), 2017–2030.

Smolchowski M. (1921). Elektrische endosmose und stromungsstrome. *Handbuch Del Elektrizitat Und Des Magnetismus*, *2*, 366.

Soh, W., Nakayama, K., & Kimura, T. (1998). Arc–arc collision in the Izu collision zone, central Japan, deduced from the Ashigara Basin and adjacent Tanzawa Mountains. *Island Arc*, *7*(3), 330–341.

Soh, W., Pickering, K. T., Taira, A., & Tokuyama, H. (1991). Basin evolution in the arc-arc Izu Collision Zone, Mio-Pliocene Miura Group, central Japan. *Journal of the Geological Society*, *148*(2), 317–330.

Tachi, Y., & Yotsuji, K. (2014). Diffusion and sorption of Cs+, Na+, I− and HTO in compacted sodium montmorillonite as a function of porewater salinity: Integrated sorption and diffusion model. *Geochimica et Cosmochimica Acta*, *132*, 75–93.

Taira, A. (1988). The Shimanto belt in Shikoku, Japan-evolution of Cretaceous to Miocene accretionary prism. *The Shimanto Belt, Southwest Japan-Studies on the Evolution of an Accretionary Prism*.

Tanikawa, W., & Tadai, O. (2018). Data Report for quantitative analysis of mineral composition using powdered X-ray diffraction method and RockJock program. *JAMSTEC Rep. Res. Dev.*, *27*, 57–67.

Terzaghi, K. (1925). Principles of soil mechanics. IV. Settlement and consolidation of clay. *Engineering News-Record*, *95*, 874.

Tripathy, S., Sridharan, A., & Schanz, T. (2004). Swelling pressures of compacted bentonites from diffuse double layer theory. *Canadian Geotechnical Journal*, *41*(3), 437–450.

Trütner, S., Hüpers, A., Ikari, M. J., Yamaguchi, A., & Kopf, A. J. (2015). Lithification facilitates frictional instability in argillaceous subduction zone sediments. *Tectonophysics*, *665*, 177–185.

Van Olphen, H. (1977). *An introduction to clay colloid chemistry: For clay technologists, geologists, and soil scientists*. Wiley.

Van Oss, C. J., Giese, R. F., Li, Z., Murphy, K., Norris, J., Chaudhury, M. K., & Good, R. J. (1992). Determination of contact angles and pore sizes of porous media by column and thin layer wicking. *Journal of Adhesion Science and Technology*, *6*(4), 413–428.

Vannucchi, P., Spagnuolo, E., Aretusini, S., Di Toro, G., Ujiie, K., Tsutsumi, A., & Nielsen, S. (2017). Past seismic slip-to-the-trench recorded in Central America

megathrust. *Nature Geoscience*, *10*(12), 935–940.

Verwey, E. J. W. (1947). Theory of the Stability of Lyophobic Colloids. *The Journal of Physical and Colloid Chemistry*, *51*(3), 631–636.

Vrolijk, P., & Van Der Pluijm, B. A. (1999). Clay gouge. *Journal of Structural Geology*, *21*(8–9), 1039–1048.

Wang, J., Liu, H., Wang, L., Zhang, H., Luo, H., & Gao, Y. (2015). Apparent permeability for gas transport in nanopores of organic shale reservoirs including multiple effects. *International Journal of Coal Geology*, *152*, 50–62.

Warr, L. N., & Cox, S. (2001). Clay mineral transformations and weakening mechanisms along the Alpine Fault, New Zealand. *Geological Society, London, Special Publications*, *186*(1), 85–101.

Wibberley, C. (1999). Are feldspar-to-mica reactions necessarily reaction-softening processes in fault zones? *Journal of Structural Geology*, *21*(8–9), 1219–1227.

Wu, Y.H., Yeh, E.C., Dong, J.J., Kuo, L.W., Hsu, J.Y., & Hung, J.H. (2008). Core-log integration studies in hole-A of Taiwan Chelungpu-fault Drilling Project. *Geophysical Journal International*, *174*(3), 949–965.

Yamaguchi, A., Cox, S. F., Kimura, G., & Okamoto, S. (2011). Dynamic changes in fluid redox state associated with episodic fault rupture along a megasplay fault in a subduction zone. *Earth and Planetary Science Letters*, *302*(3), 369–377.

Yamamoto, Y. (2006). Systematic variation of shear-induced physical properties and fabrics in the Miura–Boso accretionary prism: The earliest processes during off-scraping. *Earth and Planetary Science Letters*, *244*(1–2), 270–284.

Yamamoto, Y., & Kawakami, S. (2005). Rapid tectonics of the Late Miocene Boso accretionary prism related to the Izu–Bonin arc collision. *Island Arc*, *14*(2), 178–198.

Yamamoto, Y., Mukoyoshi, H., & Ogawa, Y. (2005). Structural characteristics of shallowly buried accretionary prism: Rapidly uplifted Neogene accreted sediments on the Miura-Boso Peninsula, central Japan. *Tectonics*, *24*(5).

Zhu, C.M., Ye, W.M., Chen, Y.G., Chen, B., & Cui, Y.J. (2013). Influence of salt solutions on the swelling pressure and hydraulic conductivity of compacted GMZ01 bentonite. *Engineering Geology*, *166*, 74–80.